UCLouvain

epl

École polytechnique de Louvain

Sparse-array metasurface: design of a feeding network and optimisation

Author: **Victor Schoofs**
Supervisor: **Christophe Craeye**
Readers: **Jonathan Dessy, David González Ovejero, Dimitri Lederer, Claude Oestges**
Academic year 2023–2024
Master [120] in Electro-mechanical Engineering

Acknowledgments

I would like to express my deepest gratitude to everyone who has supported me throughout the journey of completing this master thesis.

First and foremost, I would like to express my sincere thanks to Prof. Christophe Craeye for his support throughout the year. Thank you for the guidance, advice and availability you have shown me throughout this year, from the beginning to the writing of this document. The feedback and ideas you gave me were always helpful in exploring new areas to address the issues I faced.

Secondly, I would particularly like to thank Jonathan Dessy for his valuable support throughout the year. Your help and explanations on this subject, which was initially very obscure to me, were necessary for the completion of this thesis. Thank you for your time and investment, it was a pleasure to have your assistance.

Furthermore, I would like to thank Dr. Jean Cavillot, Dr. Modeste Bodehou and Dr. David González Ovejero for their valuable suggestions for improvements and their expertise in this field. Thanks also to Maxime Drouguet and Dr. Khaldoun Al Khalifeh for their precious advice and expertise on prototyping.

In addition, I would like to thank Prof. Dimitri Lederer and Prof. Claude Oestges for being part of my jury and for taking the time to read this document. I would also like to thank Brigitte Dupont and François Hubin for the time they spent helping me with the software issues I encountered throughout the year.

Finally, a big thank you to my family and all my friends who have supported me throughout the year. Your daily encouragement has really helped me to complete this work.

Abstract

Metasurface (MTS) antennas are 2D structures composed of a thin dielectric slab on which periodic arrays of metal patches are disposed. Feeding pins are located inside of the substrate and generate surface waves (SWs) when supplied. These propagating surface waves (SWs) in the dielectric slab are being perturbed by the slow spatial variation in the shapes of the patches. The resulting perturbation generates leaky-wave radiation, which can be controlled by altering the size, shape, and orientation of the patches. In particular, this master thesis focuses on the 3D design and full-wave analysis of sparse-array MTS antennas. Such arrays are based on a common metasurface but feature wider beam spacing, offering an efficient alternative for beam scanning applications compared to traditional phased array antennas. This larger spacing reduces the density of electronic components, at the expense of a reduced field of view. This technology has the potential to offer innovative solutions to a wide range of applications, including air traffic control, satellite communications, and other fields.

The primary objective of this master thesis is to design the feeding network of the sparse-array MTS antennas, which is responsible for supplying the feeding pins. The purpose of the feeding pins is to launch a planar surface wave that propagates along the MTS and excites the arrays of patches in a uniform manner. The feeding network aims therefore to achieve homogeneous currents in the aforementioned feeding pins, despite the very strong coupling between those pins. Firstly, a theoretical model of the feeding network is constructed, based on the principles of transmission line theory. The model is then subjected to a series of parametric tests and optimisations until the results are deemed satisfactory. Afterwards, a spectral analysis is conducted to ascertain the consistency of the propagating fields and the similarity between the radiation pattern generated by the MTS and the predicted one. We validated and improved the 2D simulations conducted in a previous study through 3D full-wave analysis, by comparing the radiation patterns obtained using a full-wave commercial solver and those simulated with a simpler in-house code. A satisfactory design has been found.

Contents

Mathematical notations and Acronyms

Mathematical notations

$j = \sqrt{-1}$	imaginary unit
X	a scalar
$\overrightarrow{X}$	a vector
$\mathbf{X}$	a matrix
$\hat{x}$	a unit vector
$f(x, y, z)$	a quantity in the spatial domain
$\widetilde{f}(k_x, k_y, k_z)$	a quantity in the spectral domain
$\|X\|$	the absolute value of X
$\delta(x)$	the Dirac delta function of x
$\mathbb{Z}$	the set of integers
$\times$	the cross product operator
$\circledast$	the convolution operator
$\cdot$	the dot product operator

Acronyms

1D	One Dimension
2D	Two Dimensions
3D	Three Dimensions
ADS	Advanced Design System
AF	Array Factor
BW	Bandwidth
CST	Computer Simulation Technology
EBG	Electromagnetic Band-Gap
EEP	Embedded Element Pattern
EFIE	Electric Field Integral Equation
EM	Electromagnetic
FEM	Finite Element Method
FIT	Finite Integration Technique
FT	Fourier Transform
IBC	Impedance Boundary Condition
IFT	Inverse Fourier Transform
MoM	Method of Moments
MTS	Metasurface
PEC	Perfect Electrical Conductor
PW	Planar Wavefront
SLL	Sidelobe Level
SW	Surface Wave
RF	Radio Frequency
TE	Transverse Electric
TEM	Transverse Electromagnetic
TLIN	Transmission Line
TM	Transverse Magnetic
VED	Vertical Elementary Dipole

Chapter 1

Introduction

1.1 Context and Problem statement

Nowadays, the demand for advanced communication and radar systems is constantly growing, driven by the need to increase performance, reliability, and versatility, while trying not to increase cost too much. To keep pace with these evolving demands, antennas constantly improve, leading to cutting-edge technologies that enhance communication systems and other applications. One of these technologies that is of main interest for this work is the beam scanning antenna, it consists of an antenna capable of controlling the direction of the radiated pencil-shaped field. Beam scanning is a very useful technology employed across a wide range of frequency bands for applications in many domains such as defense, air traffic control to monitor aircraft movements, satellite communications, 5G networks, remote sensing, astronomy, and many other areas as described in [1], [2], [3]. Among the different ways of realising beam scanning, the phased array antenna stands out and will be used as a basis for comparison in this work. This technology offers unparalleled beam steering and signal processing capabilities, making it an ideal reference point for developing and evaluating new beam scanning methods.

1.1.1 Phased array antennas

Unlike traditional antenna systems that rely on mechanical movement to direct their beams, phased array antennas use multiple radiating elements with electronically controlled phased shifters. This allows the accurate control of the beam steering angle as depicted in Figure 1.1 [4], [5]. It makes this technology highly efficient and easily adaptable. Phased array antennas can indeed be very useful since they provide high directivity, rapid beamforming, and flexibility to support multiple simultaneous beams. These features are essential for modern applications where speed, accuracy, and reliability are paramount.

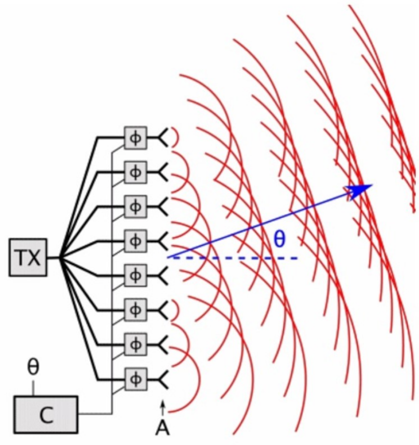

Figure 1.1: Phased array antennas with beam steering [4].

1.1.2 $\lambda/2$ spacing constraint

Phased array antennas are a set of spatially distributed antennas. In this work, only the case of equally spaced antennas along a line is considered, where adjacent antenna elements are separated by a distance d, called the element spacing. The element spacing is a critical factor for phased array antennas. The expression of this spacing d to ensure an ideal directivity is given by the following condition extracted from *Nguyen Thanh Huong's book* [5] and adapted to the θ angle from Figure 1.1 as:

$$\frac{d}{\lambda} \leq \frac{1}{1 + |cos(\frac{\pi}{2} - \theta)|} \tag{1.1}$$

where λ is the free-space wavelength and θ is the angle from broadside, also called the angle of arrival. It is represented in Figure 1.1 and has a range going from 0 to 2π radian. The worst case for this condition would be $\theta = \frac{\pi}{2}$ radian, which yields the condition for the element spacing of $d \leq \lambda/2$. Although, in reality, a scan angle of $\pi/2$ rad is usually not requested. Instead, a range of angles between $-\pi/3$ rad and $\pi/3$ rad is more realistic, allowing for a maximum spacing of 0.536λ, which is nearly equivalent to the common spacing of $\lambda/2$.

Maintaining a spacing of $d \leq \lambda/2$ helps to avoid so-called grating lobes (as explained in Section 2.1.2) by ensuring that the main lobe is prominent in the radiation pattern. However, a smaller spacing increases the mutual coupling between adjacent elements, which can affect the impedance and radiation pattern of each element. It also requires a greater number of elements for a given array aperture size, increasing complexity, cost and power consumption. An increase in spacing would result in the emergence of non-negligible grating lobes, which correspond to repetitions of the main lobe in other directions. This would give rise to directivity issues, resulting in power losses in these unintended directions. The spacing is directly proportional to the wavelength at the operating frequency. Consequently, as the frequency increases, the spacing decreases, due to the inverse relationship between wavelength and frequency. This results in a very high electronic density at high frequencies, which leads to higher manufacturing complexity and cost, making this technology difficult to use for this type of applications. A larger spacing is therefore required, but the challenge of dealing with the grating lobes remains [5].

1.2 Solutions provided by metasurfaces

A solution to the problem encountered with phased array antennas is the more recent technology named *metasurfaces* (MTS) [6]. The objective of this technology is firstly to allow the manipulation of near-fields, and additionally to achieve a significant reduction in electronic density through an increase in element spacing and a modification of the feeding method. An example of a MTS antenna at multiple scales is shown in Figure 1.2.

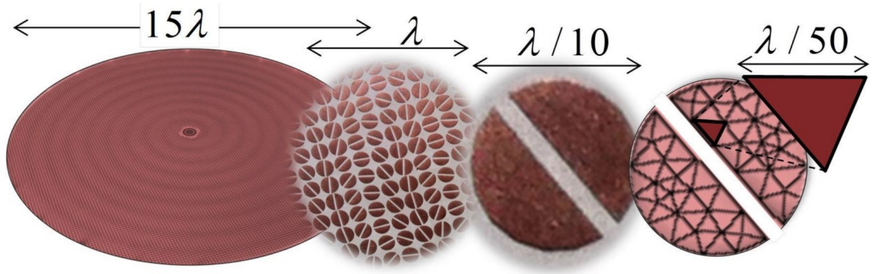

Figure 1.2: Example of a circular MTS antenna at multiple scales [7].

Metasurfaces are increasingly favoured for their simple structure and versatility compared to traditional technologies. They manipulate electromagnetic waves at a scale smaller than the wavelength, allowing precise control over properties such as beam shape [8]. Their thin structure and efficiency make them ideal for compact, integrated applications in various fields. Overall, metasurfaces offer advanced capabilities that drive innovation across different technologies. However, beam-scanning defeats the purpose of simplicity offered by MTSs. This is not a concept that is frequently discussed in the context of conventional MTSs. It remains a challenging undertaking, as it a priori necessitates the reconfiguration of each sub-wavelength metal patch of the MTS in order to alter the embedded element pattern (EEP) and the orientation of the beam.

Considering how phased array antennas function, this work shows how its concept is applied to MTS to allow it to perform beam scanning. While phased array antennas need a spacing $d \leq \lambda/2$, the MTS presented in this master thesis have a spacing of 2λ and can perform beam scanning as proven by 2D simulations realised in this parallel work [9]. The trade-off for this increased spacing is a reduction in the scan range. In the remainder of this work, we will refer to this particular type of MTS with a spacing larger than usual as a sparse-array metasurface antenna. The use of metasurfaces is therefore not so simple if we want to use them in a way similar to phased array antennas, but the solution presented in this work is promising. The metasurface antennas presented in this work aim to scan over a large rectangular window and use beam steering similar to the phased array antenna to scan in different directions. Additional information about the functioning and origin of metasurfaces is given in Chapter 2.

This master thesis takes place in the framework of the *FITNESS project* and focuses on the design of the feeding network of the sparse-array MTS [10]. It provides a 3D analysis of how the electromagnetic fields behave in the device and allows one to compare the actual radiation pattern with the one previously simulated thanks to simulations made using the software *CST Studio Suite 2022* (CST)[11].

1.3 Goal and Outline

To summarise, the objective of this master thesis is to design the feeding network of the sparse-array metasurface. To achieve this, the various options already available in the literature will be analysed and the transmission lines (TLINs) theory will be applied to the specific case presented in this work, taking into account the multiple challenges it presents. To determine when the feeding network is operational, CST is employed to simulate the interactions of the electromagnetic field within the model and to ascertain whether the currents flowing in the different ports (in terms of both magnitude and phase) meet the requisite specifications. Once the simulations have been completed and deemed satisfactory, the feeding network with the different layers and the metasurface patches (previously designed to obtain the desired rectangular EEP) are merged to observe the radiation pattern. It is only after these steps have been completed that the prototype of the MTS can be manufactured and tested in an anechoic chamber to observe whether it functions as intended, with a comparison between the observed results and the simulations.

This master thesis is organised into several chapters. First of all, Chapter 2 begins with a theoretical review of phased array antennas, followed by an examination of the state of the art in metasurfaces. This enables an understanding of the technological advances and the purpose of the MTS. Finally, the spectral field representation is discussed, and the equations describing the behaviour of the propagating field are derived. This chapter will provide an overview of the specific characteristics of the sparse-array MTS. The Chapter 3 will address the design and circuit analysis of the feeding network. It will begin by outlining the decisions made to determine its overall configuration explaining the various assumptions made. The preliminary designs are created using the *Advanced Design System* (ADS) [12]. The Advanced Design System (ADS) is a software tool frequently employed for microwave circuit analysis. It enables the simulation of the complete feeding network with TLINs in 2.5D, which is a representation halfway between 2D and 3D. This enables the identification of the most promising possibilities and the rejection of those that are not feasible, prior to commencing a 3D analysis of the model on CST. Chapter 4 is devoted to the design and full-wave analysis using CST. The objective is to optimise the feeding network in order to mitigate the impact of coupling generated by closely spaced connectors and between adjacent elements of the sparse-array MTS. Furthermore, the integration of the patches into the CST design will be examined to ascertain the necessary modifications for the prototype to function correctly and to achieve the desired radiation pattern. Once the feeding network is operational, a series of tests will be conducted to analyse the behaviour of the fields and the resulting radiation pattern. Finally, a comparison of the full-wave simulations performed with CST and 2D MATLAB simulations will be carried out. The final chapter concludes this work and offers suggestions for potential improvements and further avenues of investigation.

Chapter 2

Phased array antennas and metasurfaces

2.1 Phased array antennas

An antenna array is used to obtain different radiation patterns by modifying the individual phase of each antenna element (see Figure 1.1). The total radiation pattern is the result of the sum of the contributions from each radiating element. Assuming a similar amplitude for each antenna element, the total pattern is determined solely by the distribution of the antennas in the array and the phase differences induced in each element. Beyond the short introduction in the previous chapter, this section will serve as a more detailed theoretical review of phased array antennas explaining how they work. The equations discussed in this section are elaborated in greater detail in Chapter 2 of the course *LELEC2910 Antennas and Propagation* [13]. They aim to explain how the radiation pattern is determined and allow the derivation of the $\lambda/2$ constraint for phased array antennas density, which was mentioned in the introduction.

2.1.1 Array factor and embedded element pattern

Considering a set of N antennas arranged as shown in Figure 1.1, and denoting the electric field radiated by antenna n as $\overrightarrow{E}_n$, and thanks to the linearity of Maxwell's equations, one can write the total field radiated by the set of antennas as:

$$\overrightarrow{E} = \sum_{n=1}^{N} \overrightarrow{E}_n \tag{2.1}$$

where each field $\overrightarrow{E}_n$ radiated by a single antenna n is evaluated without other antennas active. In passing, this doesn't mean that the radiated field is the same as if the antenna was isolated, because there is still mutual coupling between the different antennas [13]. To sum up the contribution of different antennas, the translation and multiplication principle is considered to obtain easily the total radiated field of an array. It states that we can translate different sources to a central point with the only difference being the phase shift due to the difference of distance of propagation. Thanks to this principle and by considering that every antenna has the same radiation pattern, we can express the radiated field of an antenna array with only the radiated field of the central antenna and the different phase shifts due to other antennas. The hypothesis that each antenna has the same radiation pattern would be valid in the case of an infinite array. This is due to the fact that each antenna would have an identical number of antennas on its sides, regardless of its position within the array. Conversely, in a small array, we cannot assume that two radiation patterns will be identical if we compare the centre element of the array with another at the edge of the array. In that case, mutual coupling does not have the same effect on center and edge elements.

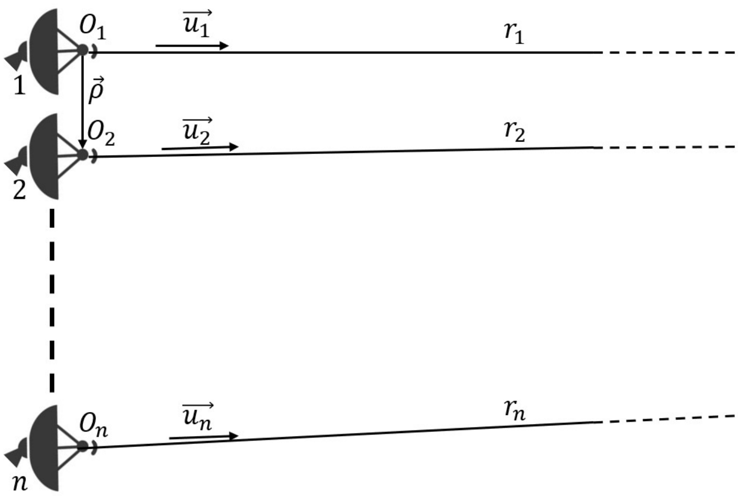

Figure 2.1: Antenna array with an illustration of the translation principle.

First of all, the radiated field of the source O_1 emitted at a large distance r_1 (i.e. the Fraunhofer region[1]) can be expressed depending on this distance as:

$$\overrightarrow{E}_1 = \frac{\exp(-jk\ r_1)}{r_1}\ \overrightarrow{F}(\vec{u}_1) \tag{2.2}$$

where $k = 2\pi/\lambda$ is the wavenumber, j is the imaginary unit, and $\overrightarrow{F}(\vec{u}_1)$ is the radiation pattern along the unit direction vector $\hat{u}_1$.

[1]Region where the radiation pattern does not change shape with distance r even though the fields still decay in $\frac{1}{r}$ [14].

The translation principle applied for a far-field region allows one to write the radiated field from O_2 as shown in equation 2.3. By applying this to each radiating source, one can easily express the total radiated field as:

$$\vec{E}_2 = \vec{E}_1 \exp(jk\ \vec{\rho} \cdot \vec{u}) \tag{2.3}$$

where $\vec{\rho}$ is the translation vector. It indicates the relative position shift between adjacent antennas in the array. The radiation pattern of an antenna n with respect to a chosen point O can be written as:

$$\vec{F}_{no}(\vec{u}) = a_n\ \vec{F}_o(\vec{u}) \tag{2.4}$$

where a_n is a complex number which indicates that the only differences between the radiation patterns from different antennas are their amplitude and phase.[2]
By merging equations 2.1 to 2.4, we can get the radiated field of the array denoted as:

$$\vec{E} = \sum_n \vec{E}_n = \frac{\exp(-jk\ r)}{r} \vec{F}_o(\vec{u}) \sum_n a_n\ \exp(jk\ \vec{\rho}_n \cdot \vec{u}) \tag{2.5}$$

It allows us to define the *array factor* (AF) as the only term depending on the *array* itself by writing:

$$R(\vec{u}) = \sum_n a_n\ \exp(jk\ \vec{\rho}_n \cdot \vec{u}) \tag{2.6}$$

The multiplication principle enables us to derive an expression for the radiation pattern directly, which links the radiation pattern of one antenna $F_o(\vec{u})$ with the array factor $R(\vec{u})$. This expression depends solely on the geometry of the array.

$$\vec{F}(\vec{u}) = \vec{F}_o(\vec{u})\ R(\vec{u}) \tag{2.7}$$

This is analogous to stating that the radiation pattern is the product of the embedded element pattern (EEP) and the AF, where $\vec{F}_o(\vec{u})$ is the EEP in this equation. In the time domain, it corresponds to the convolution of the inverse Fourier transforms (IFT) of the EEP and the AF (see Appendices A for a reminder).

For a linear array, the AF can be rewritten from equation 2.6 by solving the dot product $\vec{\rho} \cdot \vec{u} = x_n\ \cos(\theta)$ where x_n is the distance of antenna n respectively to the origin. When the N sources are spaced by a distance d and by placing the source $n = 0$ at the origin, the following expression is obtained:

[2]Since an imaginary number $a + j * b = r * \exp(j\theta)$ with the amplitude being $r = \sqrt{a^2 + b^2}$ and the phase $\theta = \arctan(b/a)$.

$$R(\theta) = \sum_{n=0}^{N} a_n \ \exp[jn(kd \ \cos(\theta))] \tag{2.8}$$

In the particular case of phased array antennas, it is common to use a phase varying linearly with position to steer the arrival angle as desired by adjusting the phase shift. In that case, one can write:

$$a_n = A_n \ \exp(jn\alpha) \tag{2.9}$$

with A_n being the amplitude of a_n and α is the chosen phase shift between consecutive array elements. This allows us to perform a change of variables as:

$$\psi = kd \ \cos(\theta) + \alpha \tag{2.10}$$

Finally, let us consider an odd number of source $N = 2M + 1$ and sources located symmetrically around the central source such that $A_{-n} = A_n$. The AF obtained can be written as:

$$R(\theta) = A_0 + 2 \sum_{n=1}^{M} A_n \ \cos(n\psi) \tag{2.11}$$

2.1.2 Grating lobes

Typical AFs can be represented as a real periodic function varying in $\cos(n\psi)$, as shown by the electric field expression in equation 2.2. An example with a certain number of elements N is shown in Figure 2.2.

As previously stated, the AF is a periodic function of the variable ψ. However, only a subset of the ψ domain represents the physically feasible radiation pattern, which is referred to as the *visible region*. As illustrated in the diagram, this region is represented by the circle and corresponds to:

$$0 < \theta < \pi \tag{2.12}$$

which can be written in terms of ψ from equation 2.10:

$$\alpha - kd < \psi < \alpha + kd \tag{2.13}$$

The shift of the circle by an angle α allows us to graphically draw the polar radiation pattern. The factor determining the part of the AF that appears in the visible region is therefore the *element spacing* d. In particular, we will exactly have one period of $R(\theta)$ in the visible region when $2kd = 2\pi$ or $d = \lambda/2$ since $k = 2\pi/\lambda$. If this spacing d is greater than $\lambda/2$, we can observe that the visible region will contain repetitions of the main lobe, which we want to avoid as much as possible. These

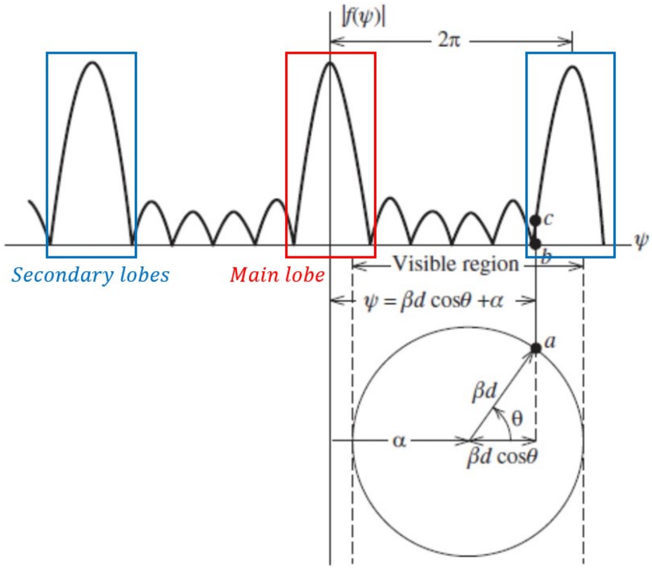

Figure 2.2: Graphical representation of the array factor [15].

grating lobes usually have a great amplitude; they lead to both power losses and ambiguities since the power is radiated in many directions. The spacing constraint introduced in the first chapter comes from this development and it is crucial for phased array antennas to respect this constraint if a high directivity is required.

The directivity which describes how focused the radiation pattern of an antenna array is, is also enhanced by taking a distance lower than $\lambda/2$. The directivity of an antenna is defined as the ratio of the radiation intensity in a given direction to the average radiation intensity in all directions. For a given angle θ_p, this can be rewritten as:

$$D(\theta_p) = \frac{4\pi}{\Omega_A} \tag{2.14}$$

where Ω_A quantifies the total power radiated by the antenna over all directions and is written as:

$$\Omega_A = \int_0^{2\pi} d\phi \int_0^{\pi} |R(\theta)|^2 \sin\theta \, d\theta = 2\pi \int_0^{\pi} |R(\theta)|^2 \sin\theta \, d\theta \tag{2.15}$$

As previously stated, the sparse-array MTS being designed in this work will have a spacing of 2λ between its elements. This spacing is not practical in the context of phased array antennas, as it leads to grating lobes. Consequently, the upcoming chapters will focus on the design of the feeding network and the subsequent analysis of the radiation pattern, with the primary objective of avoiding these grating lobes. To achieve this, a rectangular EEP is required to cut the grating lobes of the AF, as discussed in [16].

2.2 State of the Art and Origin of Metasurfaces

2.2.1 Metamaterials

To understand where these metasurfaces come from, let us first look at their origins, which lie in the field of *metamaterials*. The latter comes from the Greek "meta" and "material", meaning beyond materials. These artificial materials, fashioned from composites such as metals or plastics, cannot be found in nature and may exhibit unique properties in response to electromagnetic fields. They are composed of a multitude of sub-wavelength-sized objects, periodically arranged to form a 3D structure in such a way that they exhibit unique properties, such as negative permittivity and permeability, as represented in Figure 2.3 [17], [18].

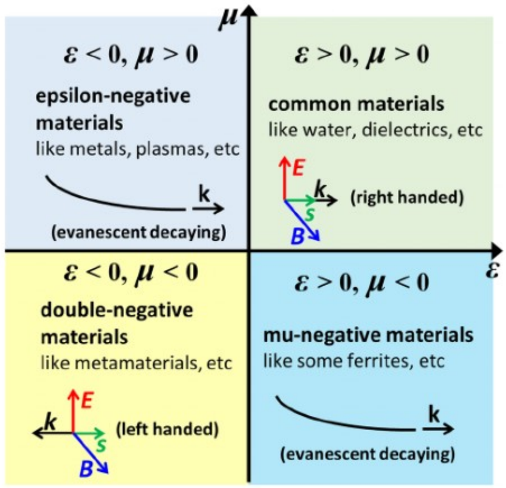

Figure 2.3: Categories of materials according to their permittivity (ϵ) and permeability (μ) [19].

Waves in double-negative or left-handed media, as shown above, behave in such a way that their direction of propagation k is opposite to their Poynting vector $\vec{S}$. The latter represents the directional energy flux of an electromagnetic field as:

$$\vec{S} = \vec{E} \times \vec{H} \tag{2.16}$$

where $\vec{E}$ and $\vec{H}$ are respectively the electric field vector and the magnetising field vector. It can be demonstrated that metamaterials are theoretically capable of producing a phenomenon whereby the energy propagates in a direction opposite to that of the waves themselves, as evidenced by [20]. The objects forming metamaterials can have different shapes and have their own properties depending on how they are arranged and how electric and magnetic fields interact with each object.

Figure 2.4 shows different existing ways to assemble objects to create metamaterials. These metamaterials have also proved their worth in improving chiroptical response

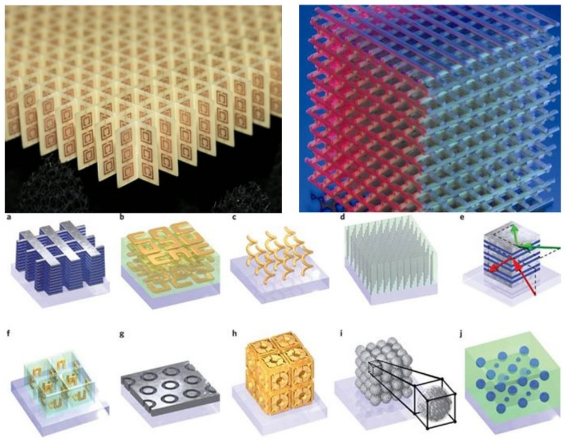

Figure 2.4: Different possible shapes of metamaterials [18].

by manipulating the amplitude, phase and polarisation of electromagnetic fields. Chiroptical refers to the optical properties of chiral substances, which are materials that have a non-superimposable mirror image, like left and right hands. These properties include how such substances interact with circularly polarised light, leading to phenomena such as optical rotation (the rotation of the plane of polarised light) and circular dichroism (differential absorption of left- and right-handed circularly polarised light) [21].

2.2.2 Metasurfaces

Metasurfaces can be seen as two-dimensional (2D) or planar versions of metamaterials and are constructed from stacked layers of dielectric materials interleaved with layers of conducting metals, forming a composite structure where patches are meticulously arranged on the top surface or even at each interface. The layer's thickness is small compared to the wavelength [21].

MTS antennas are designed and optimised to serve as a tool for controlling electromagnetic waves. They are treated periodically and the desired response at each point of the surface is obtained by slowly varying the shapes, sizes and orientation of the periodically repeated patches and their mutual arrangement. It enables precise control of the angle of reflection/transmission and to reach anomalous reflections or transmissions, but also to focusing waves towards a specific point, to absorb the incident waves, ...

The principle of the MTS is that the antenna is excited by a surface wave (SW) which propagates within the dielectric slab along the entire MTS and excites all the patches on its surface. As the SW propagates, it encounters and is affected by minor spatial variations resulting from the presence of the patches. That perturbation generates leaky-waves, potentially producing a well-controlled radiation pattern, contingent on the configuration of the patches in relation to one another [6].

When a MTS antenna is modulated at the wavelength scale (with a periodicity p), several spatial harmonics of the fundamental wavenumber are created, some of which may fall within the visible range and cause radiation. As the spatial harmonics interact with the modulation pattern, they can give rise to leaky-wave radiation. In this case, energy is gradually radiated away from the metasurface as the wave propagates, which can be used to generate a directional beam. These harmonics are called Floquet modes and correspond to the following wavenumbers:

$$k_x^{(n)} = k_{sw} + n\frac{2\pi}{p} \ \forall \ n \in \mathbb{Z} \tag{2.17}$$

where k_{sw} is the wavenumber of the SW. On the other hand, if the surface impedance is considered unmodulated (constant), the SW will propagate in the MTS but will not radiate because its wavenumber is outside of the visible region [9].

2.2.3 Global structure of the designed MTS

The operating frequency selected for this work is $f_c = 24$ GHz, which yields the free-space wavelength employed throughout the remainder of this work as follows:

$$\lambda = c/f_c = 12.5 \ mm \tag{2.18}$$

where $c \approx 3 \ 10^8$ [m/s] is the speed of light in vacuum. The metasurface structure presented in this work is unusual since it is divided into 7 identical cells of dimensions 2λ along the x-axis and 4λ along the y-axis, running consecutively along the x-axis, which corresponds to a MTS of dimensions $14\lambda \times 4\lambda$. On top of every cell, series of patches are periodically arranged as represented in Figure 2.5. Each of these cells with its respective patches is considered as an element of the metasurface array (in the case of phased array antennas, each antenna is individually controlled in the antenna set) and is composed of a feeding network within the bottom layers that will be discussed in Section 3.3.1. The spacing between consecutive unit cells is chosen to be twice the wavelength which is 4 times larger than the maximum element spacing used in phased array antennas, as explained in Section 1.1.2. In the remainder of this work, this particular type of MTS will be referred to as a *sparse-array metasurface antenna*.

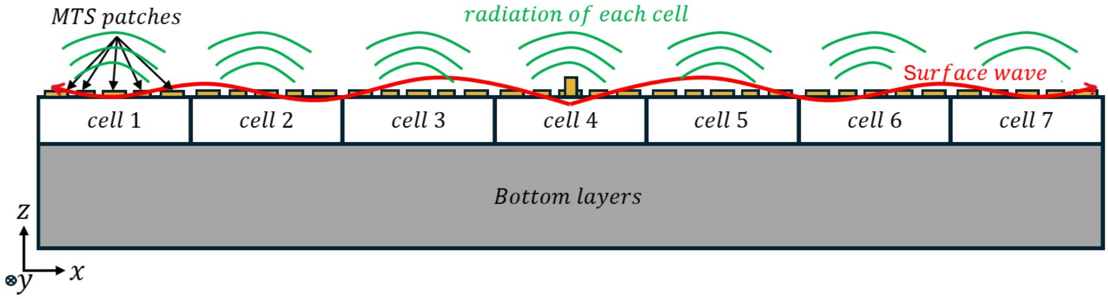

Figure 2.5: Representation of a metasurface composed of 7 cells with their radiation and the surface wave propagating.

The particularity of these sparse-array antennas is thus to have a large spacing between consecutive cells to drastically reduce the density of electronic components previously used for phased array antennas. However, as explained during the introduction and developed in Section 2.1.2, the greater the spacing, the higher the sidelobe level (SLL) will be, compared to the main lobe. These sidelobes must be avoided if we want the antenna to work as desired. To do so, the patches are designed to obtain a sharp rectangular EEP that filters out the grating lobes, as explained in Section 2.2.4.

2.2.4 Principle and desired behaviour in our case

The reference frequency used in previous work is 24 GHz. The relative bandwidth (BW) is determined according to the reference pattern obtained at the central frequency $f_c = 24$ GHz. The operating frequency limits are defined as the frequencies at which a 3 dB difference with respect to the reference pattern is observed. Simulations performed in [16] gave an approximated BW of 5%. The frequency range is therefore given by:

$$f_{low} = 24 - \frac{\Delta f}{2} \leq f \leq 24 + \frac{\Delta f}{2} = f_{up} \tag{2.19}$$

where $\Delta f = \text{BW} \times f_c = 0.05 \times 24$ GHz $= 1.2$ GHz. Thus, frequencies within the range of $[f_{low} - f_{up}] = [23.4 - 24.6]$ GHz yield results that are comparable to those previously simulated [22].

In this application, all patches are identical along the y-axis and they are separated by a distance $\Delta_y = \lambda/7$. Along the x-axis, however, they are periodically repeated every $2\lambda/3$ and separated by a distance of $\Delta_x = \lambda/12$. The desired behaviour is obtained when the propagating SW is invariant along the y-axis, so that each patch radiates similarly along that axis. This is also called a *planar wavefront* (PW) and represents a wave propagating along the x-axis that is in phase at each point along the y-axis. To obtain this PW, many SWs are generated directly so that the sum of these SWs can be approximated by a PW. In fact, 16 vertical elementary dipoles (VEDs) are evenly spaced by $\lambda/4$ along the y-axis of each cell, as shown in Figure 2.6. Each dipole is excited by the feeding network to generate a SW. The feeding network is therefore designed parameter by parameter to achieve the desired planar wavefront.

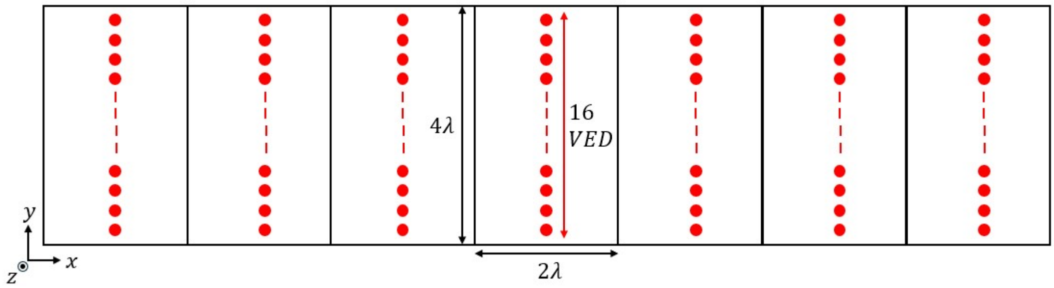

Figure 2.6: Representation of the MTS from the top with the 7 cells and 16 VEDs along the y-axis.

The proper operation of the sparse-array metasurface is checked through the analysis of the embedded element pattern (EEP) one gets when a single feed network is excited at a time. It will differ with respect to the cell being excited, since the position of the cell is important in a finite MTS. The truncation effects of the MTS cannot be avoided. These results will therefore allow us to compare the EEP obtained from each feeding network and observe the impact of array truncation along x. By supplying all the feeding networks, different phases can be applied to the different feeding networks, resulting in the generation of different propagating PWs with distinct phases and, consequently, different radiation patterns. Beam scanning is thus achieved by adding together the radiation patterns generated by each propagating PW.

The propagating SWs, stimulate the multitude of patches arranged on the upper substrate. The patches being excited will radiate depending on their shape and their mutual arrangement, creating a unique EEP [6]. In this specific case, the desired EEP is a sharp rectangle covering a region from $-\pi/a$ to π/a in the spectral domain as represented in Figure 2.7. Parameter a is the spacing between consecutive elements of the antenna array and corresponds to $a = 2\lambda$ in this specific case. It can be observed that the grating lobes exhibit a periodicity of $2\pi/a$ with respect to the spectral coordinate $k_x = k_0 \sin(\theta)$, where $k_0 = 2\pi/\lambda_0$ is the wavenumber and the steering angle in relation to the vertical is represented by the parameter θ.

This demonstrates that an increase in the spacing a results in a reduction in the total field of view. The latter is given by the following equation:

$$|\theta_{max}| = \arcsin\left(\frac{\pi}{ak_0}\right) \tag{2.20}$$

where θ_{max} is the maximum allowed steering angle with a spacing a. It gives a theoretical scanning range of:

$$2 \times \theta_{max} = 2 \times \arcsin(\frac{\pi}{ak_0}) = 2 \times \arcsin(\frac{\pi}{2\lambda\frac{2\pi}{\lambda}}) = 28.96^\circ \tag{2.21}$$

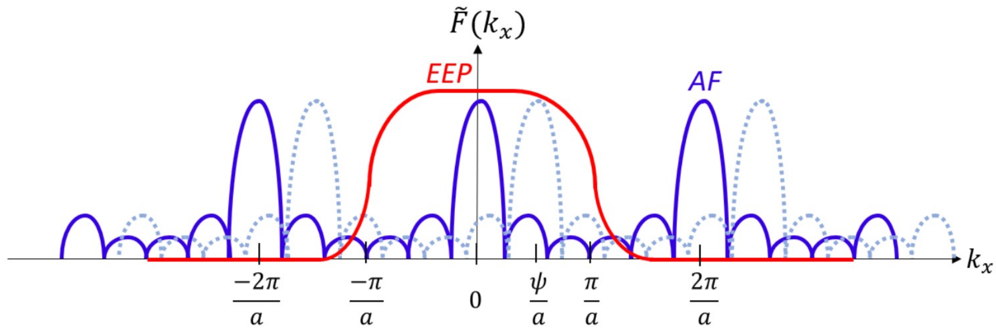

Figure 2.7: Desired EEP for filtering secondary lobes of the AF [9].

In the context of signals, and in accordance with *Fourier uncertainty principle*. This principle states that there is an inverse relationship between the width of a function in the time (or spatial) domain and the width of its Fourier transform (FT) in the frequency (or spectral) domain [23]. In other words, the more a function is localised in one domain, the more it is spread out in the other domain. In the case of the EEP presented, it is very localised in the spectral domain, which means that it will spread out a lot in the spatial domain. One can solve the IFT of the function EEP(k_x) to obtain the corresponding spatial function $f(x)$ as:

$$f(x) = \int_{-\infty}^{\infty} \text{EEP}\,(k_x)\, e^{jk_x x} dk_x = \int_{-\frac{\pi}{a}}^{\frac{\pi}{a}} e^{jk_x x} dk_x = \frac{2\pi}{a} \frac{\sin\left(\frac{\pi x}{a}\right)}{\frac{\pi x}{a}} \tag{2.22}$$

Which can be written in terms of the cardinal sine function as:

$$\frac{2\pi}{a} \frac{\sin(\frac{\pi x}{a})}{\frac{\pi x}{a}} = \frac{2\pi}{a}\ \text{sinc}(x) \tag{2.23}$$

If the EEP generated by the MTS is indeed a rectangular function, then the desired radiation from the MTS should have a shape similar to a sinc(x) with a localised peak in the centre and a decaying amplitude with increasing distance, spreading out quite widely as expected from the uncertainty principle, as shown in Figure 2.8. It is interesting to notice that this function has its zeros located at the other feed points.

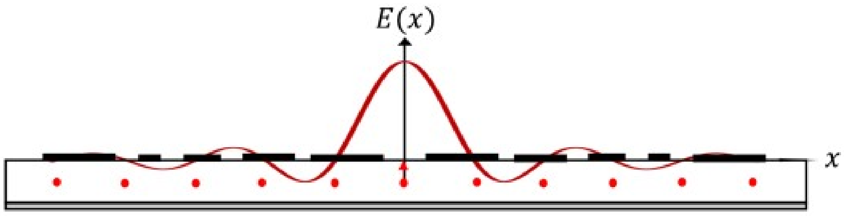

Figure 2.8: Sinc(x) shape of the desired radiated field from the entire MTS [9].

2.2.5 Analysis of 1D periodic metasurface antennas

The analysis of 1D periodic metasurface antennas involves understanding how individual patches within the periodic structure influence the overall electromagnetic performance. Each patch is specifically designed to contribute to the collective behaviour of the EEP. The impedance characteristics and mutual arrangement of these patches play a critical role in determining the radiation characteristics.

Metasurface (MTS) antennas can be analysed using full-wave simulations that consider the characteristics of each patch, or by approximating the entire surface with patches as a modulated sheet impedance, which means that it smoothly varies from place to place on the surface [24]. Patches can exhibit different resonant behaviour depending on their shape and configuration. For this MTS and full-wave analysis, the patches are either capacitive or inductive, as illustrated in Figure 2.9.

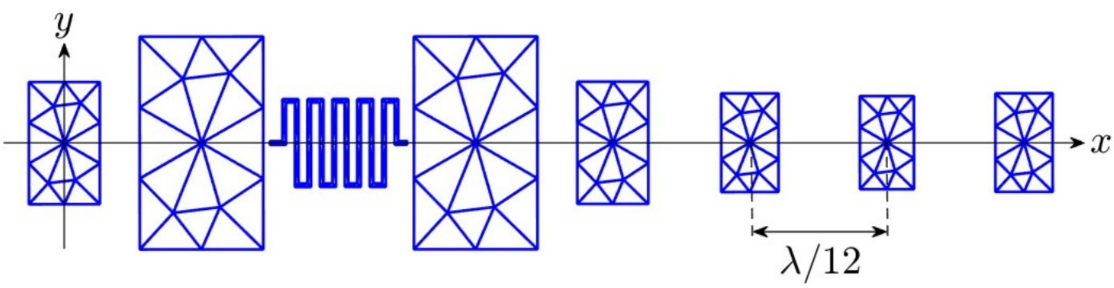

Figure 2.9: Square patches of varying sizes (capacitive) and meander lines (inductive) [9].

Sheet impedance

The leaky wave antenna concept is based on the propagating surface waves that are excited on an artificial sheet impedance and scattered by surface impedance variations to produce the desired radiation pattern [25]. As mentioned, each VED produces a SW that propagates along the x-axis; the high number of VEDs aims to create a PW invariant along the y-axis to excite every patch similarly along this axis. The periodic arrangement of patches is modulated by a periodic sheet impedance at the level of the array cell size $a = 2\lambda$ on the top grounded substrate of thickness $d_{sub} = 1.524$ mm.

Metasurface antennas are composed of a multitude of sub-wavelength patches. Their size and their periodic arrangement allow us to approximate the microscopic currents over a unit cell by surface-averaged polarisation densities and surface current densities from a macroscopic point of view. Assuming a set of similar electrically small unit cells leads to a homogenised model that can be replaced by a set of electrically and magnetically equivalent current sheets. These are characterised by surface current densities $\mathbf{J}_e$ and $\mathbf{J}_m$ [21]. This periodic homogenised model can be approximated by a sheet impedance using impedance boundary conditions (IBCs) that allow us to link the averaged tangential electric field and the surface current supported by the antenna. In this work, only the electrical currents will be used. Many methods exist to synthesise modulated metasurface antennas, but one relies on an entire-domain discretisation of the electric field integral equation (EFIE), as presented in [24], [26]. The Method of Moments (MoM) [27] is widely used in this type of discretisation and has been validated by comparing existing methods, such as full-wave analysis of a MTS and Gaussian ring-based functions in [28].

The sparse-array MTS antenna presented in this work was simulated using the sheet impedance method in [16]. The optimised impedance used for the modulation of the MTS is given by:

$$Z_s(x) = jX_0\Big(1 + M\sin\Big(3\frac{2\pi}{a}x\Big)\Big) \tag{2.24}$$

with an average reactance $X_0 = -1200\ \Omega$ and a modulation depth $M = 1.2$. The spatial coordinates x vary between $-a/2$ and $a/2$ for a total range of $a = 2\lambda$, which is the cell size. This impedance is then repeated for each cell to periodically modulate the entire MTS.

Full-wave analysis of MTSs

This approach uses electromagnetic simulation techniques to accurately model and study the interaction of electromagnetic waves with metasurfaces for both 1D and 2D models. Each patch within the periodic array is considered individually with its own characteristics (see Figure 2.9). The structure repeats along one dimension and periodic boundary conditions are applied to simplify the analysis. These conditions assume that the electromagnetic fields repeat periodically, which reduces the problem size and the computational complexity.

Once all the conditions are applied, the system based on Maxwell's equations is solved. It relies on numerical methods such as the Finite Element Method (FEM) or the Method of Moments (MoM). The results of these simulations are then processed to extract information about the electromagnetic fields, radiation patterns and other relevant parameters. References [16] and [29] respectively provide an example using sheet-impedance modelling and another one using full-wave analysis.

For a metasurface to be modeled effectively, the elementary basis functions used to represent the currents must be smaller than the wavelength. This ensures that the functions can capture the detailed variations in the current distribution, leading to more accurate simulations and designs. If the basis functions are too large, important details may be missed, leading to errors like grating lobes, which can degrade the performance of the metasurface. They are thus designed to work at certain frequencies determined by the global size of the structure [6]. The underlying concept is that an excitation source (often a vertical dipole) induces an electromagnetic field which reacts with the top layer substrate and creates surface waves (SW) propagating within the dielectric slab [30].

2.2.6 Different applications of metasurfaces

Metasurfaces are revolutionising the way devices can interact with waves, offering an extensive toolkit for manipulating them. One of their standout features is their ability to enhance antenna efficiency, ensuring better communication and connectivity. But their usefulness doesn't stop there; they can also be crafted into ideal absorbers, enabling applications like stealth technology and efficient energy harvesting. Moreover, metasurfaces open up possibilities for creating superlenses that defy conventional optical limitations [31], as well as cloaking devices that can render objects invisible at certain frequencies [32]. Additionally, they have shown promise in eliminating scattering, paving the way for clearer imaging and more precise sensing.

While these applications have primarily been explored in the domains of microwaves and optics, there is a real potential for metasurfaces to impact other fields [17], [33]. These applications have been tested and proven in numerous papers as mentioned above and hereunder, yielding very interesting results on potential technologies and new improvements that could emerge in the future. Some interesting applications have been developed in the different areas listed hereunder.

Holographic leaky-wave metasurfaces

The type of MTS used in this work is a holographic leaky-wave MTS. It is composed of a multitude of patches displayed on the top substrate. Changing the disposition of those patches results in a change in the sheet impedance of the MTS itself. We can observe both the sheet impedance and the resulting radiation pattern in the example on the right (see Figure 2.10) when changing the global holography of the MTS (the patches arrangement).

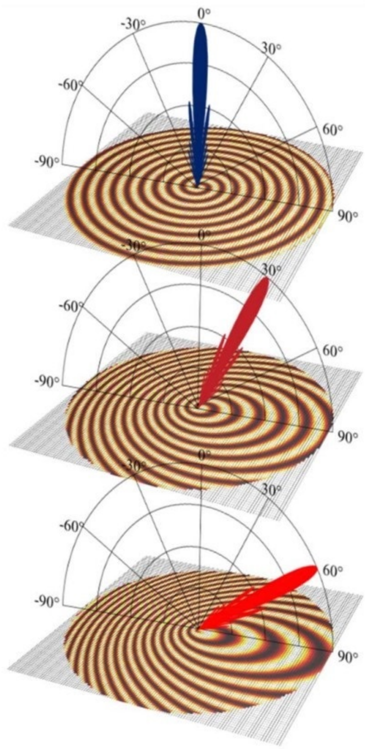

Figure 2.10: Different radiation patterns obtained with the adaptive holographic structure of a metasurface [6].

Different beam angles can be achieved by altering this holography, but it is not dynamically adaptive and therefore needs to be remanufactured for each change. Another problem is the bandwidth or frequency stability of the pattern. The bandwidth of the pattern is primarily limited by the mismatch between the wavelength of the SW and the periodicity of the IBCs, which occurs when the operating frequency deviates from the design frequency, as described in [34]. Nevertheless, this type of MTS structure is still the most feasible and accessible in terms of shape, direction and polarisation control [6], [35].

Reconfigurable Intelligent Surfaces

As explained in the comparison of phased array and metasurface antennas, the problem with a conventional MTS is that the steering angle can't be changed without reconfiguring the patches arrangement or using a method that allows dynamic control of the radiation pattern. Unlike these conventional MTSs, a reconfigurable MTS allows dynamic control of the structure. Many interesting methods for dynamically controlling the configuration of the MTS are described and developed in [36]. Advances in these methods will be particularly useful for solving current problems, as explained hereunder.

For example, in large cities, antennas on buildings often can't reach devices hidden behind other structures. The use of reconfigurable MTSs as anomalous transmitters can solve this problem by redirecting the emitted signal to the inaccessible targets with controlled anomalous reflection, providing wireless power transmission (see Figure 2.11) [37]. In addition, in satellite communications, reconfigurable MTSs can dynamically adjust beam directions to maintain stable connections with moving satellites, improving the reliability of data transmission while retaining the benefits of MTS compactness. These advances will be significant for urban communication networks and satellite systems, providing flexible and efficient solutions.

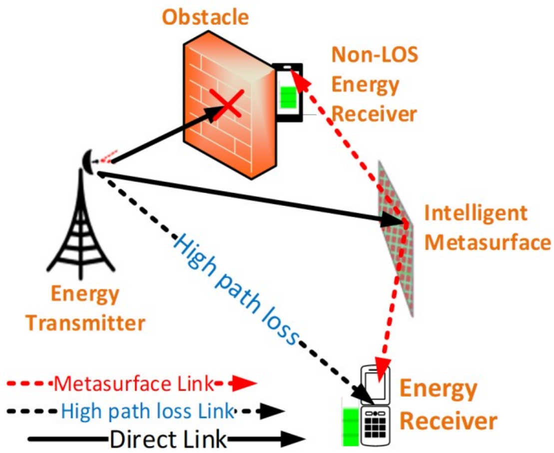

Figure 2.11: Cooperative networks based on Metasurface aided transmission [37].

Biomedical applications

The unique optical properties of metasurfaces have been explored for various biomedical applications, particularly in beam shaping for laser processing, light sheet fluorescence microscopy, HiLo microscopy and optical trapping, as discussed in [38]. Metasurface-based light-shaping devices are promising, offering capabilities difficult to achieve with conventional optical elements at the microscopic scale, making them ideal for advanced biomedical devices. The ultra-compact size and weight of metasurface-based optical elements can help to reduce the complexity of the design of the multi-view light sheet microscope systems. The metasurface enables the use of a single element for illumination that can be connected to the specimen holder, rather than using illumination from multiple directions as in previous methods.

Optical manipulation

Metasurfaces are widely used in optical applications. Significant progress has been made in holographic imaging thanks to metasurfaces. For instance, they enable multiple degrees of freedom in optical manipulation. In particular, the demonstration of helicity multiplexing or orthogonal physical channel multiplexing, such as polarisation, has been showcased, as described in [39]. In this work, by changing the helicity of circularly polarised light, it is possible to interchange two centrally symmetric and off-axis holographic images (flower and bee), as shown in Figure 2.12.

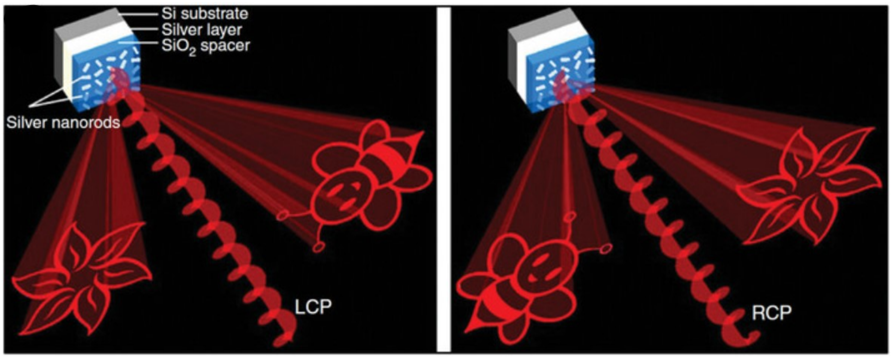

Figure 2.12: Helicity multiplexed metahologram producing flower and bee in the reflection domain under left and right circularly polarised illuminations [39].

2.3 Spectral field representation

This section develops the equations needed to understand how the fields emitted by the VEDs behave in a single layer grounded medium. This corresponds to the two top layers of the MTS, which are the substrate and the ground plane just below it, as represented in Section 3.3.1. As the SWs propagate within this dielectric slab, it is interesting to understand the equations behind the observations made. Once these equations are developed, they can be used to compare ideal fields and fields obtained with the values obtained from CST to analyse whether or not they behave as they should.

2.3.1 TE and TM modes

The surface wave at the origin of the leaky-wave radiation corresponds to a transverse magnetic (TM) mode. It is therefore interesting to understand the nature of transverse electric (TE) and transverse magnetic (TM) modes before moving on to the equations of the electric field. These modes describe the orientation of the electric and magnetic fields in relation to the direction of wave propagation. In TE modes, the electric field (E-field) is entirely transverse to the direction of propagation. This means that the electric field has no component in the direction of propagation, whereas the magnetic field has a component along the direction of propagation. Conversely, in TM modes, the magnetic field (H-field) is entirely transverse to the direction of propagation. This means that the magnetic field has no component in the direction of propagation, but the electric field has a component in the direction of propagation.

In an (x,y,z) Cartesian system of coordinates, the electric field can be written as:

$$\mathbf{E} = \mathrm{A}\ e^{-j(k_x x + k_y y + k_z z)} \tag{2.25}$$

where one can define the wavenumber $\vec{k}$ as:

$$\vec{k} = \begin{bmatrix} k_x \\ k_y \\ \pm k_z \end{bmatrix} \tag{2.26}$$

Furthermore, these plane waves can be represented in a layered medium with a specific vector basis, where $\hat{k} = \hat{e} \times \hat{m}$, is a unit vector in the direction of propagation, as shown in Figure 2.13. The characteristic directions, described in [40], are defined as:

$$\hat{k} \triangleq \frac{\vec{k}}{|\vec{k}|}, \quad \hat{m} \triangleq \frac{1}{\beta}\begin{bmatrix} -k_y \\ k_x \\ 0 \end{bmatrix}, \quad \hat{e}^{\pm} \triangleq \frac{1}{\beta|\vec{k}|}\begin{bmatrix} \pm k_x k_z \\ \pm k_y k_z \\ -\beta^2 \end{bmatrix} \tag{2.27}$$

where the subscripts + and − denote upward and downward propagating waves, respectively. While $\beta \triangleq k_x^2 + k_y^2$, represents the radial propagation constant that describes how the phase of the wave changes along the direction of propagation.

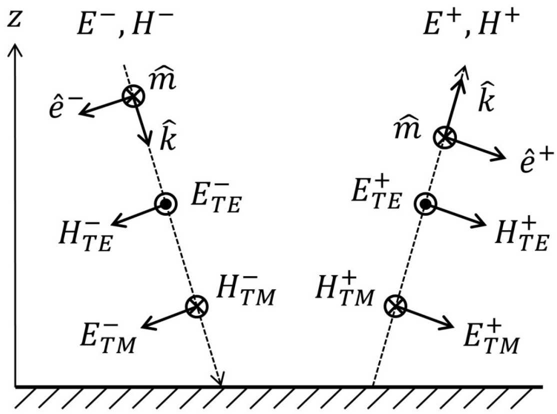

Figure 2.13: Representation of the vector basis [40].

Using this vector basis eases the analysis of the fields in layered media. Since $\hat{m}$ is always parallel to the interfaces, TE waves present an electric field solely along that direction. Similarly, TM waves present a magnetic field solely along $\hat{m}$. This will be very useful for deriving the equations of fields in Section 2.3.3.

2.3.2 Green's function

To compute the fields in layered media, it is first important to understand what the *Green's function* is. It corresponds to the field distribution associated with a given point source in a given material environment. From a mathematical point of view, they can be considered as the spatial impulse response of the radiation operator. In free-space, the expression of the Green's function is developed in [41]. For the magnetic vector potential, it can be written as:

$$\mathbf{G}(R) = \frac{e^{-jk_0R}}{4\pi R} \tag{2.28}$$

where $R = |r - r'|$ with r and r' being the points of observation and source, respectively. From there, electric and magnetic fields are easily derived.

In its most general form, the Green's function is dyadic, since fields and currents have components in both x and y directions, and is therefore written as a tensor. This function can be used to derive the amplitudes of TE and TM waves propagating away from an interface, either upwards or downwards, expressed in the spectral domain for each wavenumber pair of spectral coordinates (k_x, k_y). It can be obtained in the spatial domain by convolution of the Green's function $\mathbf{G}$ and the current distribution $\mathbf{J}$, which is equivalent to a product in the spectral domain. It can be written as:

- In spectral domain:

$$\tilde{\mathbf{E}}(k_x, k_y) = \tilde{\mathbf{G}}(k_x, k_y)\ \tilde{\mathbf{J}}(k_x, k_y) \tag{2.29}$$

- In spatial domain:

$$\mathbf{E}(r) = \mathbf{G}(r, r') \circledast \mathbf{J}(r') \tag{2.30}$$

In the case of the MTS antenna, the layered medium considered is a single grounded layer media and the final expression of the Green's function is given by:

$$\tilde{\mathbf{G}}(k_x, k_y) = \begin{bmatrix} \widetilde{G}^{xx} & \widetilde{G}^{xy} \\ \widetilde{G}^{yx} & \widetilde{G}^{yy} \end{bmatrix} = \widetilde{G}_A(k_\rho) \begin{bmatrix} 1 & 0 \\ 0 & 1 \end{bmatrix} + \widetilde{G}_V(k_\rho) \begin{bmatrix} k_x^2 & k_x k_y \\ k_x k_y & k_y^2 \end{bmatrix} \tag{2.31}$$

The development of this result is rigorously detailed in [40]. The two scalar potentials $\widetilde{G}_A(k_\rho)$ and $\widetilde{G}_V(k_\rho)$ for a single-layer substrate depends only on $k_\rho = \sqrt{k_x^2 + k_y^2}$ and their analytical expressions are developed in [40], [41].

2.3.3 Spectral representation of fields in layered media

The copper ground plane medium is considered as a perfect electrical conductor (PEC) to match with the assumptions made in [40]. Waves at this interface are fully reflected, giving the following reflection coefficients $\Gamma_{TE} = -1$ and $\Gamma_{TM} = 1$, defined as the ratio of the incident wave coefficient to the reflected wave coefficient. Plane waves propagating in layered media are generally described with their electric and magnetic fields as:

$$\mathbf{E}^{\pm} = \left(-\hat{m}E_{\mathrm{TE}}^{\pm} + \hat{e}^{\pm}E_{\mathrm{TM}}^{\pm}\right) e^{-jk_x x} e^{-jk_y y} e^{\mp jk_z z} \tag{2.32}$$

$$\mathbf{H}^{\pm} = \frac{1}{\eta}\left(\hat{e}^{\pm}E_{\mathrm{TE}}^{\pm} + \hat{m}E_{\mathrm{TM}}^{\pm}\right) e^{-jk_x x} e^{-jk_y y} e^{\mp jk_z z} \tag{2.33}$$

where $\eta = \sqrt{\mu/\epsilon}$ is the medium impedance, defined by the medium permeability μ and the medium permittivity ϵ. In the case of the MTS antenna shown, the excitations are VEDs. The electric field radiated by vertical equivalent currents along $\hat{z}$ produces only a TM component, which explains why the spectral field radiated by a VED contains only a TM component as developed in [40]. This simplifies a lot the analysis. For a VED oriented along $\hat{z}$ the electric field on the MTS along x and y can be rewritten as:

$$\tilde{\mathbf{E}}_z(k_x, k_y) = \widetilde{E}_{xz}(k_x, k_y)\hat{x} + \widetilde{E}_{yz}(k_y, k_z)\hat{y} + \widetilde{E}_{zz}\hat{z} \tag{2.34}$$

To obtain the radiated field in the spatial domain, the IFT can be applied directly to the expression found, but since the components of this equation are unknown, the Green's function is used to determine it instead.

- For a single VED:

$$\mathbf{E}_z(x,y) = \left(\frac{1}{2\pi}\right)^2 \iint \widetilde{\mathbf{G}}_z(k_x,k_y)\ e^{-j(k_x x+k_y y)} dk_x dk_y \tag{2.35}$$

where $\widetilde{\mathbf{G}}_z(k_x,k_y)$ corresponds to the field distribution associated to an infinite sheet of VEDs oriented along $\hat{z}$ in this case and with phase slopes along x and y, respectively. It is developed in detail in Appendix D.5 of reference [40].

- For the specific case presented of N = 16 VEDs aligned along $x = 0$:

$$\mathbf{E}_z(x,y) = \left(\frac{1}{2\pi}\right)^2 \iint \widetilde{\mathbf{G}}_z(k_x,k_y)\ \widetilde{J}(k_x,k_y)\ e^{-j(k_x x+k_y y)} dk_x dk_y \tag{2.36}$$

where $\widetilde{J}(k_x,k_y)$ is the current source distribution defined by the following FT:

$$\widetilde{J}(k_x,k_y) = \iint J(x,y)\ e^{j(k_x x+k_y y)} dx dy \tag{2.37}$$

with $J(x,y) = \sum_{p=0}^{N-1} \alpha_p\ \delta(y-y_p)\delta(x)$ where each VED_p is located at $(x_p,y_p) = \Big(0\ \ ,-2\lambda + \lambda(1+2p)/8\Big)$ and α_p being the current weight of the VED_p. Imperfections and mutual coupling within the feeding network may lead to large variations among the α_p coefficients (see Section 4.2.2). It then becomes:

$$\widetilde{J}(k_x,k_y) = \int \sum_p \alpha_p\ \delta(y-y_p)\ e^{jk_y y} dy \int \delta(x)\ e^{k_x x} dx \tag{2.38}$$

$$\widetilde{J}(k_x,k_y) = \sum_p \alpha_p\ e^{jk_y y_p} \tag{2.39}$$

which gives:

$$\mathbf{E}_z(x,y) = \left(\frac{1}{2\pi}\right)^2 \iint \widetilde{\mathbf{G}}_z(k_x,k_y)\ \sum_p \alpha_p\ e^{jk_y y_p}\ e^{-j(k_x x+k_y y)} dk_x dk_y \tag{2.40}$$

- Considering an infinite number of VEDs with unitary weights, one gets:

$$\widetilde{J}(k_x,k_y) = \int e^{jk_y y} dy \int \delta(x)\ e^{k_x x} dx \tag{2.41}$$

$$\widetilde{J}(k_x,k_y) = 2\pi\delta(k_y) \tag{2.42}$$

This gives the following expression of the electric field in spatial domain:

$$\mathbf{E}_z(x,y) = \left(\frac{1}{2\pi}\right)^2 \iint \widetilde{\mathbf{G}}_z(k_x,k_y)\ 2\pi\delta(k_y)\ e^{-j(k_x x+k_y y)} dk_x dk_y \tag{2.43}$$

$$\mathbf{E}_z(x,y) = \frac{1}{2\pi} \int \widetilde{\mathbf{G}}_z(k_x,k_y=0)\ e^{-jk_x x} dk_x \tag{2.44}$$

Chapter 3

Design and circuit analysis of the Feeding Network

3.1 Feeding Network

As mentioned in the previous chapter, the goal is to excite the metasurface and its numerous patches by first supplying a row of vertical elementary dipoles (VEDs) to generate the surface waves (SWs) propagating all along the MTS. To achieve this goal, a feeding network must be designed to power these feeding poles. The objective is to establish a connection between the input point situated beneath the MTS and the power cable, while ensuring that the power is distributed equally among all the feeding poles. The purpose of the feeding network is to achieve a uniform current magnitude and phase in each of the dipoles. There are multiple approaches that could be employed to attain this goal; however, the challenge lies in supplying power to 16 ports simultaneously, while incorporating the feeding network within a relatively confined metasurface cell.

The design methodology behind this feeding network makes use of transmission lines theory. There are numerous potential solutions for powering multiple ports, but most are not feasible in a case like the one described here due to the complex geometry.

3.1.1 Serial versus parallel feeds

Considering the case where we must supply 16 VEDs all aligned in the same plane, there are two well-known methods for achieving this type of powering. Those are the serial and parallel (also called corporate) feeding networks, as depicted in Figure 3.1.

Serial power supply network
In a serial power supply network, the power source is connected sequentially to each output terminal. This means the power signal passes through each component or load before reaching the next. As a result, the current and voltage characteristics at each output can vary due to the cumulative effects of the preceding components. Specifically, the phase of the signal at each subsequent output can shift due to the interactions and impedance of each load, leading to phase differences across the outputs. This can be problematic in applications requiring uniform phase and magnitude across all outputs.

Parallel power supply network
Conversely, a parallel power supply network connects each output terminal directly to the power source, independently of the other outputs. It is achieved using equal line lengths and power dividers for each element. This configuration ensures that each output receives the same input signal directly from the power source, maintaining consistent current magnitude and phase across all outputs. The parallel configuration is ideal for applications where uniformity in the power signal's characteristics is critical.

For these reasons, the supply network for this metasurface can only be achieved with a parallel supply network and will therefore be examined in greater detail in this work.

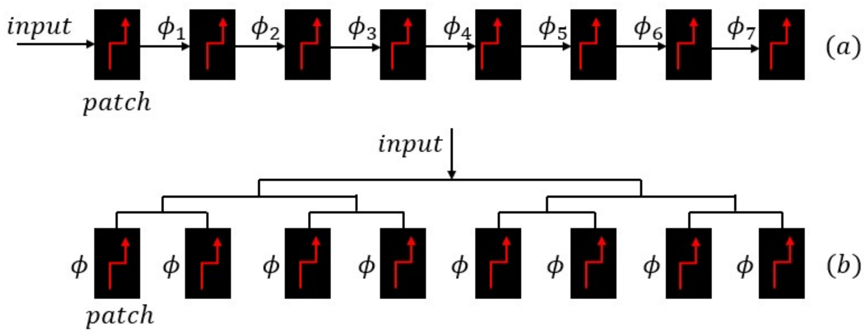

Figure 3.1: Series (a) and parallel (b) feeding networks.

3.2 Constraints and Innovations

The design of this feeding network is the main subject of this master thesis and it requires a significant amount of time and effort to develop something operational. This task was much challenging than it initially appeared for several reasons listed below.

The main problem in designing this feed is the proximity of all the transmission lines and VEDs. This is due to the limiting factor of the available size in which the feed network has to fit. As mentioned above, a cell of the MTS is $2\lambda \times 4\lambda$ along the x-axis and y-axis respectively. In this space we need to fit a feeding network capable of powering 16 VEDs simultaneously, ideally using as little space as possible to avoid mutual coupling between adjacent cells. This presents a significant challenge, as it constrains the potential design options, which may occupy a greater space than is actually available.

Speaking of coupling, this is the most difficult problem to solve because it depends directly on the proximity between the excited VEDs, which is only $\lambda/4$. Coupling is omnipresent in this network because everything is close to everything else. Lines are coupled, VEDs are coupled, and different feeding networks are coupled together also. This is by far the most challenging aspect of the design due to the hazardous nature of the coupling with constructive and destructive current densities originating from all directions. The design optimisation process is based on a number of hypotheses and a certain degree of trial and error, with parameter sweeps performed to achieve the closest possible approximation to the desired outcome. As the design progresses, new challenges emerge, which will mostly be addressed in Chapter 4.

The innovative aspect of this work will be based on the improvements made to achieve the objective. A number of simulations and designs have been carried out to identify the optimum solution. However, there are likely to be alternative approaches to designing this feed network that could meet the requirements.

3.2.1 Reflected Power Quantification

Before moving on to the more practical side of feeding networks, it is important to understand how to determine whether our antenna is working properly. The most common approach to analysing this is through the use of the *reflection coefficient* Γ. It is expressed thanks to the Scattering matrix [42]. This matrix is constructed according to the power reflected and transmitted at each port (S_{ii} is reflected and S_{ji} is transmitted from port i to port j).

In the 2-ports example, shown in Figure 3.2, the port 1 is fed and the other port is considered as the output. It is essential that the S-parameters behave properly. Therefore, we must ensure that the ratio between the forward power and the reflected power into the input port, represented by the parameter $\Gamma = S_{11} = b_1/a_1$, is as small as possible at the operating frequency. Conversely, the value of $S_{21} = b_2/a_1$

should be as high as possible, as this represents the gain transmitted through the network. The reflected power is given by:

$$P_{reflected} = |\Gamma|^2 \ P_{incident} \ [\mathrm{W}] \tag{3.1}$$

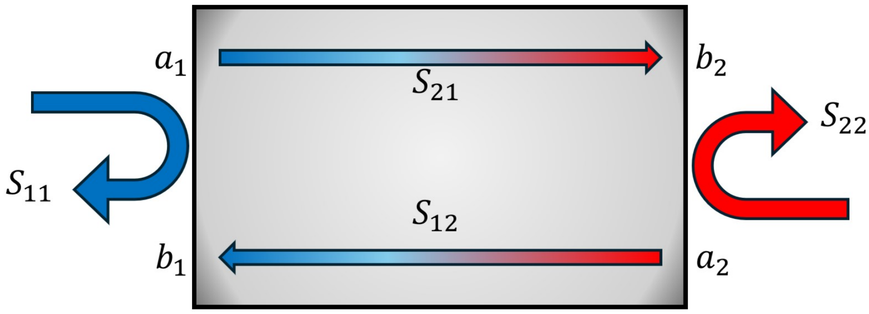

Figure 3.2: Example of a two-ports network.

One can also write the reflection coefficient as a function of the load impedance (Z_L) and the source impedance (Z_0) which represents the matching between the two impedances as:

$$\Gamma = \frac{Z_L - Z_0}{Z_L + Z_0} \tag{3.2}$$

More details can be found in [43]. The reflected power from equation 3.1 can be rewritten in dB as:

$$P_{reflected} = 20 \ log_{10}(|\Gamma|) \ [\mathrm{dB}] \tag{3.3}$$

In the remainder of this work, the magnitude of the S-parameters observed is always expressed in dB. Consequently, the value of S_{11} directly represents the reflected power in dB, and is considered to be relatively insignificant if its magnitude is less than -10 dB. Such a value indicates that less than 1/10th of the incident power is being reflected.

3.3 Structure and Assumptions

3.3.1 Comparison between stripline and microstrip lines

Stripline and microstrip lines are two types of transmission lines used in microwave circuits and antenna designs, each with distinct characteristics. A microstrip consists of a conductive strip separated from a ground plane by a dielectric substrate, with its electromagnetic field distributed both in the air and within the dielectric. This makes microstrip lines easier to design and manufacture, but it typically has higher losses due to radiation and surface wave propagation [44]. In contrast, a stripline consists of a conductor sandwiched between two parallel ground planes, as depicted in Figure 3.3. It is fully embedded within a dielectric material, confining the electromagnetic field entirely within that dielectric. The stripline supports a Transverse Electromagnetic (TEM) mode with lower losses and better impedance control [44]. However, the design is more complex due to the need for precise alignment within the dielectric layer and two ground planes.

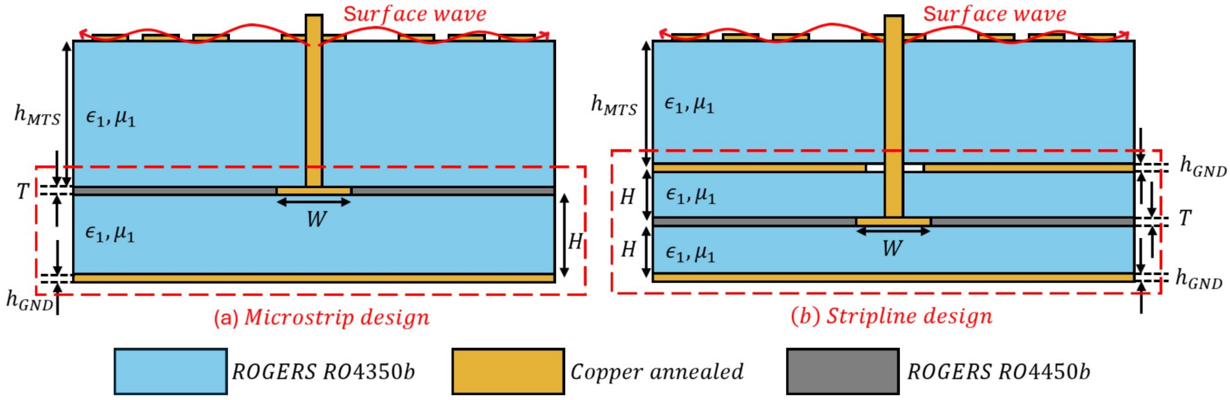

Figure 3.3: (a) Microstrip & (b) stripline models with all layers.

The stripline is particularly advantageous for metasurface applications due to its field confinement, lower losses, and precise impedance control. The confined electromagnetic field within the dielectric layer of the stripline ensures minimal external interference while the lower losses in the stripline enhance efficiency, maintaining the integrity of signals, which is essential for the high-frequency and high-precision nature of metasurfaces. The symmetric structure of the stripline also allows for better impedance control and reduces crosstalk between closely packed elements, making it ideal since many elements are packed very closely. References such as Bahl and Bhartia's Microstrip Lines and Slotlines [45], [46], Wheeler's studies on stripline properties [47], and Pozar's Microwave Engineering [42] provide in-depth insights into the advantages of stripline for these applications.

The relative pros and cons of the two designs were considered in order to determine the most suitable model for metasurface applications. It seems that the stripline design is more appropriate for this type of application, as previously discussed. The implementation process using both the ADS and CST software will be based on the stripline model. Each layer will be carefully dimensioned according to the sizes available in the datasheets for the various materials. Table 3.1 shows the thicknesses used for each material according to the design standards and the material data. The symbols can be seen in Figure 3.3.

Thickness of each layer		
Symbol used	Description of the symbol	Value (mm)
T	Conductor/prepreg thickness	0.018 or 0.5 mil
h_{MTS}	Metasurface substrate (RO4350b)	1.524
H	Top and bottom substrate of the stripline (RO4350b)	0.762
h_{GND}	Ground plane thickness	0.018 or 0.5 mil

Table 3.1: Thicknesses and their respective description.

Most of the materials and thicknesses used are chosen based on the metasurface previously built in 2023, as referenced in [48]. The standard thickness of the conductor for this type of application is typically 0.018 mm. 1 mil is a unit often used for short lengths and corresponds to 1/1000 inch which is ≈ 0.035 mm.

Prepreg, short for pre-impregnated composite fibres, is a dielectric resin used to bond the top and bottom parts of the stripline in our case. Its properties used for the simulations are similar to those of the two substrates embedding the conductor. In this case, it is simulated as RO4450b, from ROGERS, which has a relative permittivity $\epsilon_r = 3.7$ instead of $\epsilon_r = 3.66$ for the RO4350b used for the substrates, as described in the datasheets [49], [50].

3.3.2 Stripline impedance calculator

The first step in designing the feeding network is to compute the stripline impedance of each line. This can be done using various methods, such as online stripline impedance calculators [51], analytical formulas, or software tools available in ADS[1] and CST[2], which incorporate these calculations directly. The impedance of a stripline is primarily determined by its width, making it the critical factor we aim to determine using these different tools. Each method or tool may provide slightly different results due to variations in their underlying algorithms and assumptions. To address these discrepancies and facilitate comparison, Table 3.2 presents the different impedance values obtained from each method, allowing for a clearer understanding of how each tool measures up against the others. This comparison

[1]LineCalc tool used for stripline (SLIN) can be used directly in the Advanced Design System

[2]In the macros tools, the line impedance calculator can be found and used for many applications such as stripline

is essential to ensure the accuracy and reliability of the impedance values used in the feeding network design.

Widths for each impedance with different methods			
Methods	**Impedances and their width W [mm]**		
	50 Ω	70.7 Ω	100 Ω
CST	0.852	0.432	0.164
ADS	0.776	0.358	0.108
Online calculator	0.708	0.353	0.108
Analytical formula	0.85	0.421	0.221

Table 3.2: Widths obtained for each impedance using different tools.

The analytical formula is taken from the book of *Pozar, Section 3.8*, [42] and can be written as:

$$Z_0 = \frac{30\pi}{\sqrt{\epsilon_r}} \frac{b}{W_e + 0.441b} \; [\Omega] \tag{3.4}$$

where $\epsilon_r = 3.66$ is the relative permittivity of the dielectric layer, b is the total stripline thickness such that $b = 2H + T$ with H and T represented in Figure 3.3, and W_e is the effective width of the centre conductor given by:

$$\frac{W_e}{b} = \frac{W}{b} - \begin{cases} 0 & \text{for } \frac{W}{b} > 0.35 \\ (0.35 - W/b)^2 & \text{for } \frac{W}{b} \leq 0.35 \end{cases} \tag{3.5}$$

Impedance values for online calculator and ADS are similar and were therefore used for the implementation in ADS. Whereas the values from the analytical formula and CST were tested on CST to compare the results obtained with lines of different widths.

3.4 Preliminary design with ADS

The journey to design this complex structure started with the *Advanced Design System* (ADS), distributed by Keysight Technologies Inc. The method employed by ADS for the simulations conducted by the momentum solver is the Method of Moments (MoM). The current distribution on metal surfaces is determined by the Momentum solver through the conversion of the problem into integral equations and subsequent solution using the MoM, as outlined in [12]. It is particularly effective for 2D or quasi-3D structures.

The power dividers described in the existing literature were tested in this software, as it allows for a more straightforward evaluation of the functionality of the feeding network. This section will provide a brief overview of the papers that have inspired this work in order to facilitate an understanding of the various possibilities for designing an operational power divider and how to achieve effective power division. Furthermore, this section will highlight the considerable disparity between models, despite the fact that the dimensions may exhibit significant variations when they are no longer very small compare to the wavelength.

3.4.1 Literature review and ADS implementations

Many feeding networks have been implemented either in microstrip or stripline for decades. Some of them are interesting to mention since they inspired the design of the final feeding network presented in this thesis.

a. Compact non-homogeneous Corporate Feed Network

As documented in reference [52], the quarter-wavelength power divider ($\lambda/4$ power divider) is employed to divide the power in an equal manner between non-identical rectangular microstrip antenna elements. The elements in question feature varying lengths of TLIN and intermediate impedances, which are designed to ensure accurate matching between the outer and inner lines. Figure 3.4 illustrates the implementation of this concept.

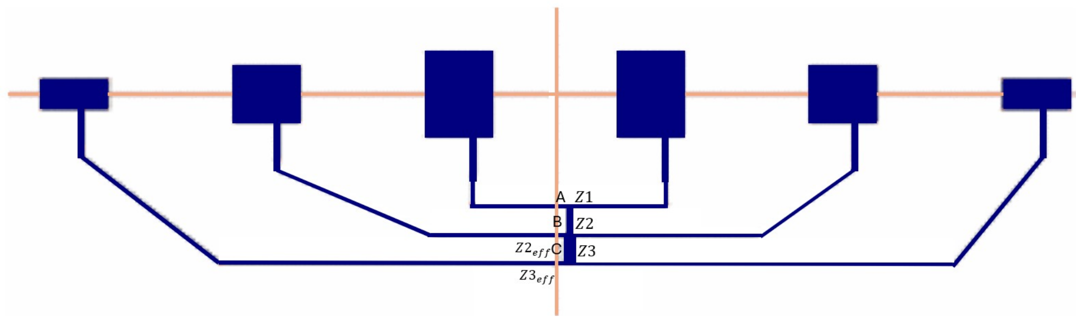

Figure 3.4: Compact Modified Corporate Feed Network for Antenna Arrays with non-identical Rectangular Microstrip antenna elements [52].

The reason for its inapplicability in this work is due to the difference in scale and the number of elements that must be excited. The microstrip feeding in this example is approximately ten times wider than that being designed in this work, and the number of elements is $\mathbf{N = 6}$, rather than $\mathbf{N = 16}$ present in the design of the sparse-array MTS. The assumptions made and issues encountered do not align with those presented in this master thesis. For example, the very long lines presented here would not be feasible if they were positioned in closer proximity. In the case of the MTS designed, the proximity is such that it would result in a high degree of coupling.

b. Wilkinson Power Divider

This power divider, sketched in Figure 3.5, is known to be very robust since it meets nearly all the requirements. Its Scattering matrix reveals that the network is *reciprocal* ($S_{ij} = S_{ji}$, which is often the case in power dividers), that the terminals are *matched* ($S_{11} = S_{22} = S_{33} = 0$) considering that there are 3 entries, and also that the output terminals are isolated ($S_{23} = S_{32} = 0$). Finally, an *equal power* division is achieved ($S_{21} = S_{31}$) [53]. The only condition that this power divider can't satisfy is the *loss-less* condition. An ideal power divider would result in an ideal division of the input power, with no loss of power. Upon each division of the power by two, a reduction of 3 dB is observed at the output terminal. This can be expressed as follows:

$$S_{j1} = \mathrm{N} \times 10 \log_{10}(\frac{1}{2}) = -3 \times \mathrm{N}\ [\mathrm{dB}] \tag{3.6}$$

In this context, the value of N represents the number of divisions by two that are necessary to achieve an equal distribution of power across 2^{N} ports. For instance, dividing the input power equally in $2^{\mathrm{N}} = 16$ ($\mathrm{N} = 4$) output terminals result in $S_{j1} = -12$ dB if no additional loss is taken into account. It is not possible to achieve the ideal scenario of zero loss in this case, due to the inevitable loss of power introduced by the resistor. However, this promising power divider has been successfully implemented in ADS, both with and without the resistor, as illustrated in Figure 3.5. This resistor serves the function of an insulator, with the power reflected from ports 2 and 3 dissipated in the resistor. This ensures that S_{23} and S_{32} are isolated, as referenced in [42].

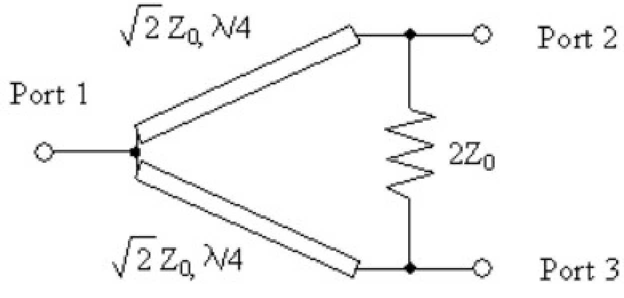

Figure 3.5: Ideal two-port Wilkinson splitter [54].

The results obtained with and without the resistor confirm what was said above, since the coupling disappears completely when this resistor is added. The problem is that resistors cannot be added easily in planar feeding networks such as stripline, and this is the reason why this model is not used as the ideal power divider it could have been. This problem was also pointed out in [55], which implemented an 8-way Wilkinson power divider.

Figure 3.6 depicts the two designs and the S_{j1} entries of the scattering matrix obtained (where the j-index denotes the output terminals). The lower part of Figure 3.6 illustrates the impact of the resistor on the S-parameters.

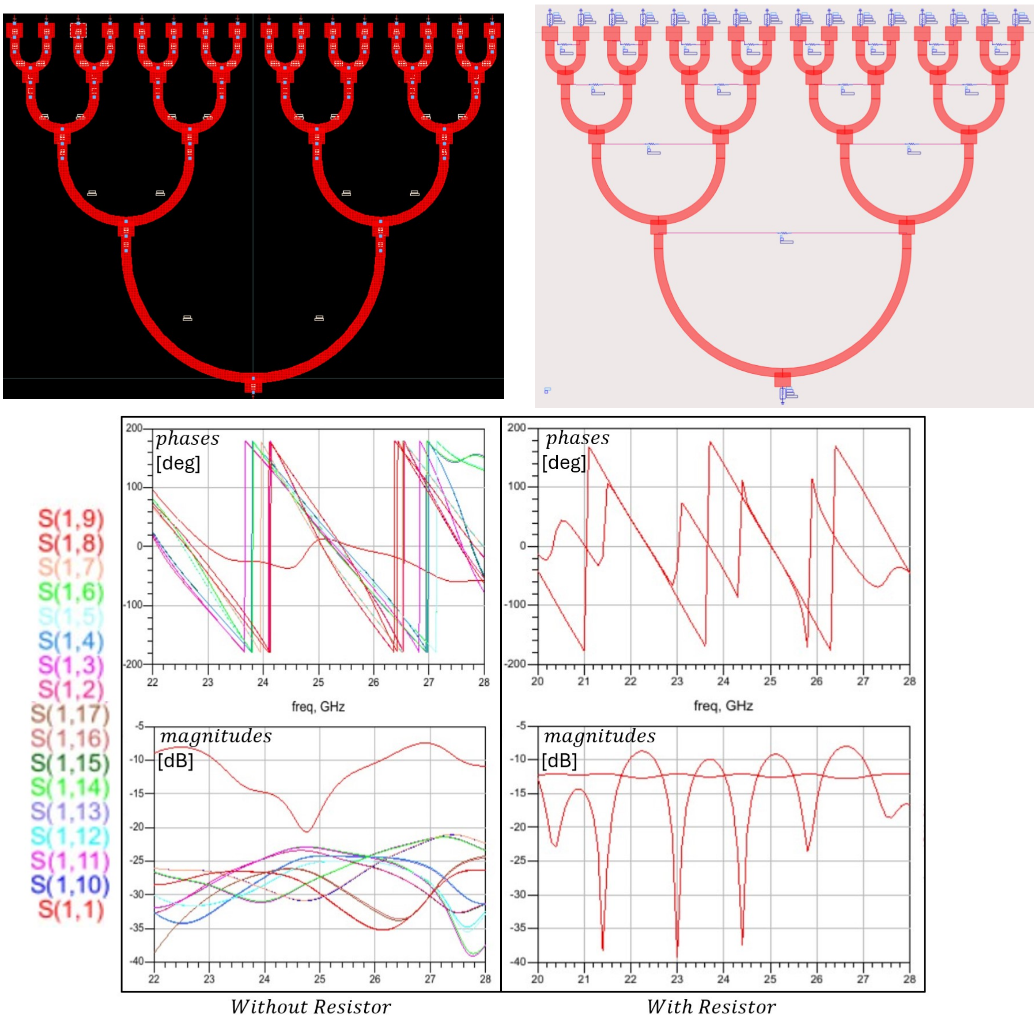

Figure 3.6: Wilkinson Power divider respectively without and with 100 Ω resistor between every separation and their respective S_{1j} parameters both in phase and magnitude $[dB]$.

It can be observed that in the absence of a resistor, the curves are symmetrical 2-by-2 along the central axis (port 1 being the input, port 2 behaves as port 17, 3 as 16, and so on). In contrast, when a resistor is present, the curves are all superimposed[3]. Furthermore, one can see in the upper right plot that all $S_{j1} : j \neq 1$ correspond to an approximate loss of -13 dB, which is almost the minimum loss in such a power divider with 4 outputs separations, as explained in equation 3.6. However, the power divider was not properly designed to match at the frequency of 24 GHz, which explains why the S_{11} curve don't yield optimal results at that frequency in these simulations.

c. Classical Quarter-wavelength Power Divider

This power divider is one of the most well-known since it applies transmission lines theory to split the power equally in all branches. In this case, we want to match the 50 Ω impedance from the input terminal and find the same 50 Ω impedance at every output terminal. The main idea for designing such a power divider, is that we divide the power by two when we separate the initial TLIN of 50 Ω into two TLINs. The impedance in each new line should be 100 Ω so that the equivalent impedance seen at the intersection is $100 \parallel 100 = 50$ Ω. The impedance seen at every output terminal is then 100 Ω instead of 50 Ω as desired. To deal with this and match the 100 Ω lines to the 50 Ω lines, quarter-wavelength transformers are used by putting an intermediary line of impedance $\sqrt{2} * Z_{50} = \sqrt{Z_{100} * Z_{50}} = \sqrt{100 * 50} = 70.7\ \Omega$. The latter has a particular length of $\lambda/4$ to cancel reflections at the desired frequency. The signal will pass through the transformer, and since its length is $\lambda/4$, the reflected power with a lower amplitude results in constructive interference with the incident power [56].

This is how one can guarantee that the designed power divider functions correctly at the operating frequency. It should be noted that this relationship with the wavelength does not imply that the bandwidth will be zero. In practice, it will be a few percent, as will be demonstrated at the end of this section. Finally, the length of the 100 Ω line is of no importance and can take any value, zero included. This is what was implemented in ADS, as depicted in Figure 3.7 where only 50 Ω and 70.7 Ω impedance lines are used. The model is inspired from the work presented by Mauricio Sánchez Barbetty in [57].

[3] If the condition of equal power division is not achieved, as indicated by the inequality $S_{j1} \neq S_{k1}$ for $k \neq j$, it can be concluded that the main purpose of the power divider is lost when the resistors are removed.

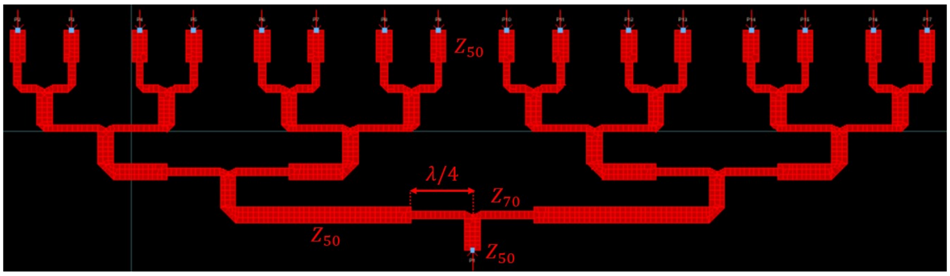

Figure 3.7: Quarter-wavelength power divider with Z_{50} and Z_{70} impedances.

The results are presented in Figure 3.8 and are promising, as all the *S-parameters* from the output terminals are superimposed in magnitude and phase, with a difference of approximately 13-14 dB relative to the input terminal at the 24 GHz operating frequency. This is nearly the optimal behaviour that can be expected from a power divider. When simulating S-parameters for a circuit in ADS, the inclusion of dielectric losses is dependent on the definition of appropriate material properties, such as the relative permittivity (ϵ_r) and the loss tangent ($\tan\delta$). These properties directly influence the insertion loss and, consequently, the S-parameters observed. An additional perspective of the current density distribution in the feeding network can be seen in Appendices B, where all ports are fed similarly.

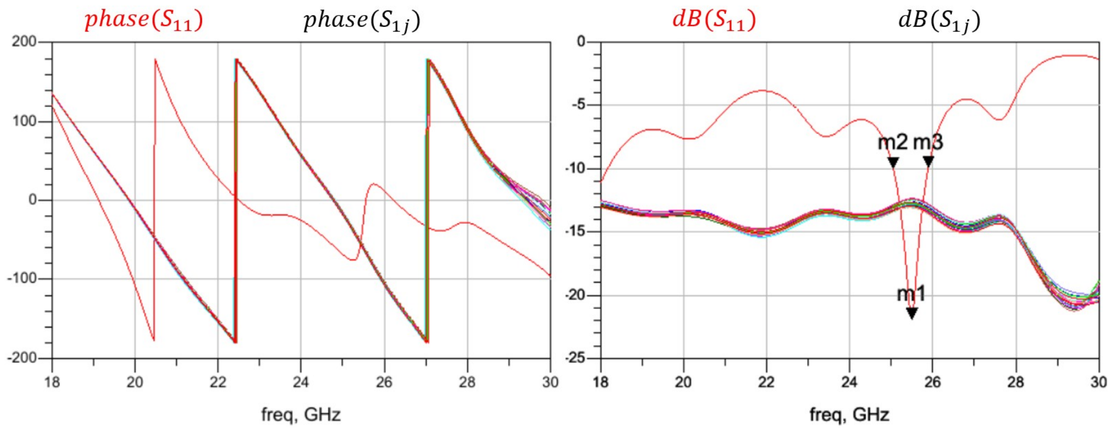

Figure 3.8: S_{ij} parameters of the quarter-wavelength power divider: phase (left) and magnitude (right).

The markers present in the right-hand side plot of the figure show the bandwidth obtained for such a power divider design. In fact, the power is correctly transmitted in the circuit if its S_{11} has a reflection coefficient below -10 dB, which is the case between about $[25, 26]$ GHz. This results in a 4% bandwidth at the centre frequency of 25.5 GHz with a reflection coefficient of -21.87 dB. However, it can be seen that the peak is centred at 25.5 GHz instead of 24 GHz, but it is possible to move this peak by changing the parameters of the various TLINs in the feed network. Before further research in this area, it is better to ensure that this first design works properly for a 3D display by considering coupling and truncation effects. It is therefore implemented in CST in the next chapter.

3.4.2 Decision based on ADS results

When designing radio frequency (RF) power distribution networks, choosing the right type of power divider is crucial for achieving the desired performance in terms of insertion loss, impedance matching, and port isolation.

A quarter-wavelength power divider uses TLIN segments that are one-quarter of the wavelength ($\lambda/4$) of the incident wave. These segments have specific characteristic impedances that enable effective signal splitting through impedance transformation (as explained in subsection 3.4.1). The simplicity of this design makes it an attractive option for many applications. In contrast, a Wilkinson power divider is a three-port network that uses resistors and $\lambda/4$ TLIN segments to achieve good isolation between the output ports while maintaining perfect impedance matching. It consists of two $\lambda/4$ TLINs and a resistor connected between the two output ports.

One major advantage of the quarter-wavelength power divider is thus its simplicity. It requires only TLIN segments without additional components like resistors, making it easier to design and manufacture. This simplicity also translates to lower insertion loss, which is critical in high-frequency applications where every decibel of loss matters. Moreover, quarter-wavelength dividers integrate well into stripline structures, as they do not need discrete components that could complicate manufacturing and integration because adding resistors would mean going beyond the 2D aspect of powering a network circuit.

However, the quarter-wavelength power divider has a limitation: it does not provide isolation between the output ports. This lack of isolation can lead to interference if the output loads are not well-matched. Despite this, in many stripline applications, the trade-off is acceptable due to the benefits of reduced complexity and lower losses. The Wilkinson power divider, while offering excellent isolation and perfect impedance matching, thanks to the added resistor, introduces additional complexity and higher insertion loss due to the inclusion of the resistors. This added complexity can be a disadvantage in stripline designs where manufacturing simplicity and low loss are prioritised. For those reasons, stripline applications often prefer the quarter-wavelength power dividers [42], [56], [58].

Chapter 4

Design and full-wave analysis with CST

The aim of this thesis is to design an optimal power divider for the sparse-array metasurface with 16 VEDs per MTS cell and to validate its performance by simulation. In the previous chapter, the ADS software was used to evaluate different power dividers, focusing on the quarter-wavelength power divider and the Wilkinson divider. The analysis showed that the quarter-wavelength power divider offers significant advantages in terms of simplicity, lower insertion loss and ease of integration, despite its lack of port isolation.

Based on these findings, we are now using *Computer Simulation Technology* (CST), distributed by Dassault Systèmes, to perform detailed 3D electromagnetic simulations of the selected power divider. The methods used by this software for 3D electromagnetic (EM) simulations are the finite integration technique (FIT) for the time domain solver, and the finite element method (FEM) for the frequency domain solver. The FIT method is used to discretise Maxwell's equations in both time and space. It is powerful for transient analysis and provides a wideband frequency response from a single simulation. Whereas, the FEM solver discretises the problem domain into finite elements and solves Maxwell's equations in the frequency domain, which is ideal for narrowband applications [11]. CST provides a more comprehensive simulation environment, allowing us to verify and refine our ADS conclusions with greater accuracy. Contrary to ADS, CST includes all the effects of mutual coupling between the VEDs. This step is critical to ensuring that the selected power divider not only meets theoretical expectations, but also performs effectively in practical scenarios.

4.1 Goal of full-wave simulation

This section is essentially used to simulate and analyse the behaviour of the currents in the various output ports and the fields throughout the model to see how they interact with the circuit. The initial aim is to obtain currents with same phases and magnitudes in each of the output ports. In order to optimise the similarity of these currents, various methods will be tested and their effects will be discussed in this section. Designing the prototype to obtain identical currents in each VED turns out not to be the best way to produce a perfect planar wavefront in the MTS layer because of the truncation effect, which will be discussed later in this section.

Once this objective has been met as well as possible for a model with a single feeding network, the various optimisation steps will be repeated with several feeding networks, as the coupling between these different networks will influence the results obtained previously for a single feeding network.

Subsequently, a number of methods for reducing the coupling between feeds (referred to in this context as different unit cells) are presented and tested. The most affordable and effective of these is then implemented in the final model that will be manufactured. The patches of the MTS will also be implemented on CST to make many observations, such as their impact on the coupling, the radiation pattern emitted from the MTS, and comparisons with the simulated MTS.

4.1.1 Input and output ports

In order to understand the following sections, it is important to understand what assumptions have been made for the input and output measurements. Power is supplied via the *53029-005J* coaxial cable from *Southwest Microwave* [59]. For the simulations, the coaxial cable is excited by a *waveguide port* located at the bottom of the coaxial cable and the outer conductor is connected to the bottom ground plane of the MTS as can be seen in Figure 4.1. The inner and outer conductors are separated by a dielectric material with a typical relative dielectric constant of $\epsilon_r = 4$. The inner conductor passes through the lower layers until it reaches the transmission lines, where it transmits power by making contact with them. However, for a question of impedance matching, the coaxial cable used for the simulations is not the one from the datasheet because it does not match the 50 Ω impedance in CST even though it is supposed to match it according to the datasheet.

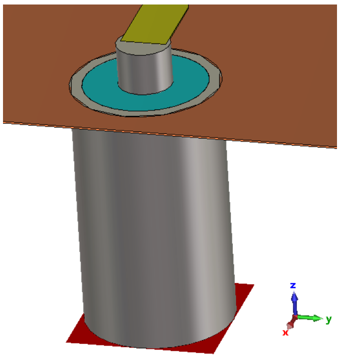

Figure 4.1: 3D perspective view of the coaxial cable.

Regarding the output ports, there are many options available in CST, but very few can be applied to the case of a VED. One cannot simply define a port at the top of the VED, because no current should reach the top, as it is similar to an open circuit. The idea then was to remove a thin layer from the VED, with a thickness of $t_{cut} = h_{Gr} = 0.1$ mm at the level of the top ground plane of the MTS (see Figure 3.3) and to use either a *discrete port* or a *lumped element* between the two parts of the VED. The discrete port has the advantage of providing information about the S-parameters in that port, but as it is not a physical component, the cut in the VED acts as a capacitor and the current through it is not sufficient to obtain consistent measurements. It is also much more consuming in terms of simulations. On the other hand, lumped elements can be defined as very low resistors, such as 1 mΩ, through which currents flow easily. This gives information about the current, such as its phase, magnitude or even its real and imaginary parts. The results obtained by this second method are more realistic and sufficient to analyse the behaviour of currents. A 3D perspective view showing how the cut in the VED was made in relation to the different layers can be seen in Figure 4.2.

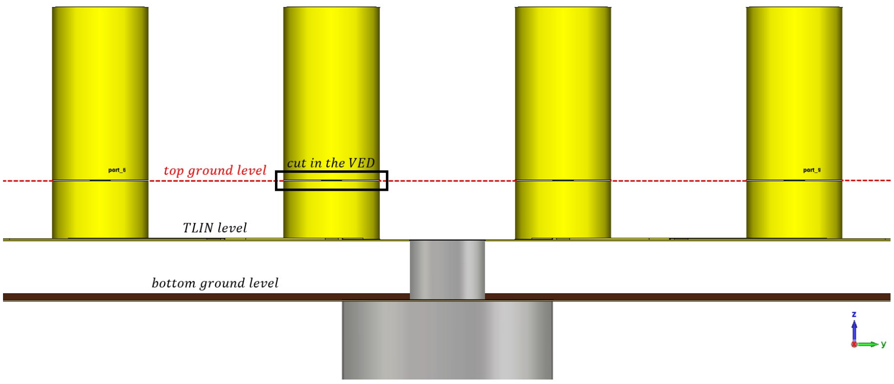

Figure 4.2: 3D perspective view of the VEDs and how the ports are implemented.

4.1.2 Single feeding network implementation

As decided after discussions about the implementations on ADS, designs made on CST are only based on the quarter-wavelength power divider concept. It starts gradually with 2, 4, 8 and 16 output ports before moving on to multiple cells, and provides qualitative information about the *S-parameters* and current characteristics, such as their phase and magnitude. Other ways are used to analyse if the design works as it should or not, those different methods are described in this section also. All the designs implemented to obtain the final feed network are not presented for reasons of readability, but the important changes are shown to understand how the feeding network evolved toward its final version.

16-ports equivalent to the ADS implementation

As mentioned earlier, the reason for using CST instead of ADS is that CST allows a proper full-wave 3D analysis. In ADS, the last design presented worked as expected in terms of currents. However, it was not possible to design the VEDs and the entire feed network was planar, meaning that the input power was fed directly into the circuit without any transmission via a coaxial cable to the TLINs. In summary, ADS does not take into account the MTS truncation effects, the mutual coupling between the VEDs, and it does not allow any 3D transmission from the coaxial cable to the TLINs or from the TLINs to the VEDs. All these effects are very important because this is how the real prototype will work. Figure 4.3 shows the CST implementation of the network while Figure 4.4 shows how the current phases and magnitudes behave now that all these effects have been taken into account.[1]

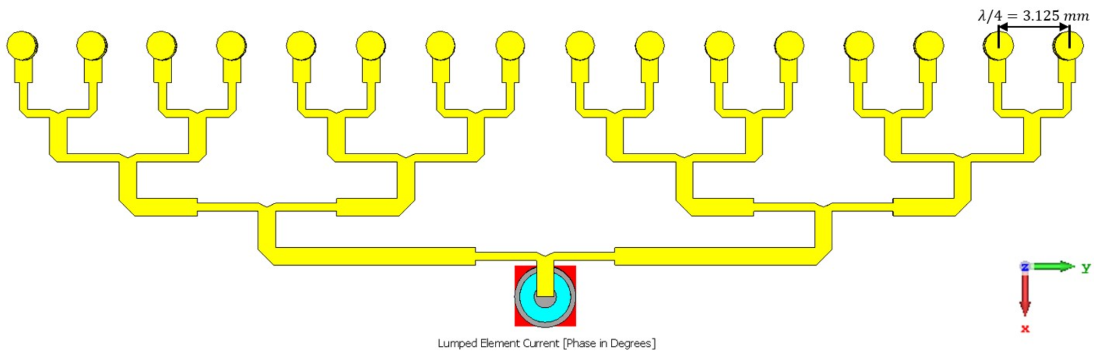

Figure 4.3: CST equivalent 16-port power divider.

[1]The different layers of the MTS are hidden for reasons of visibility, to show only the feed network itself, but they are present during the simulations.

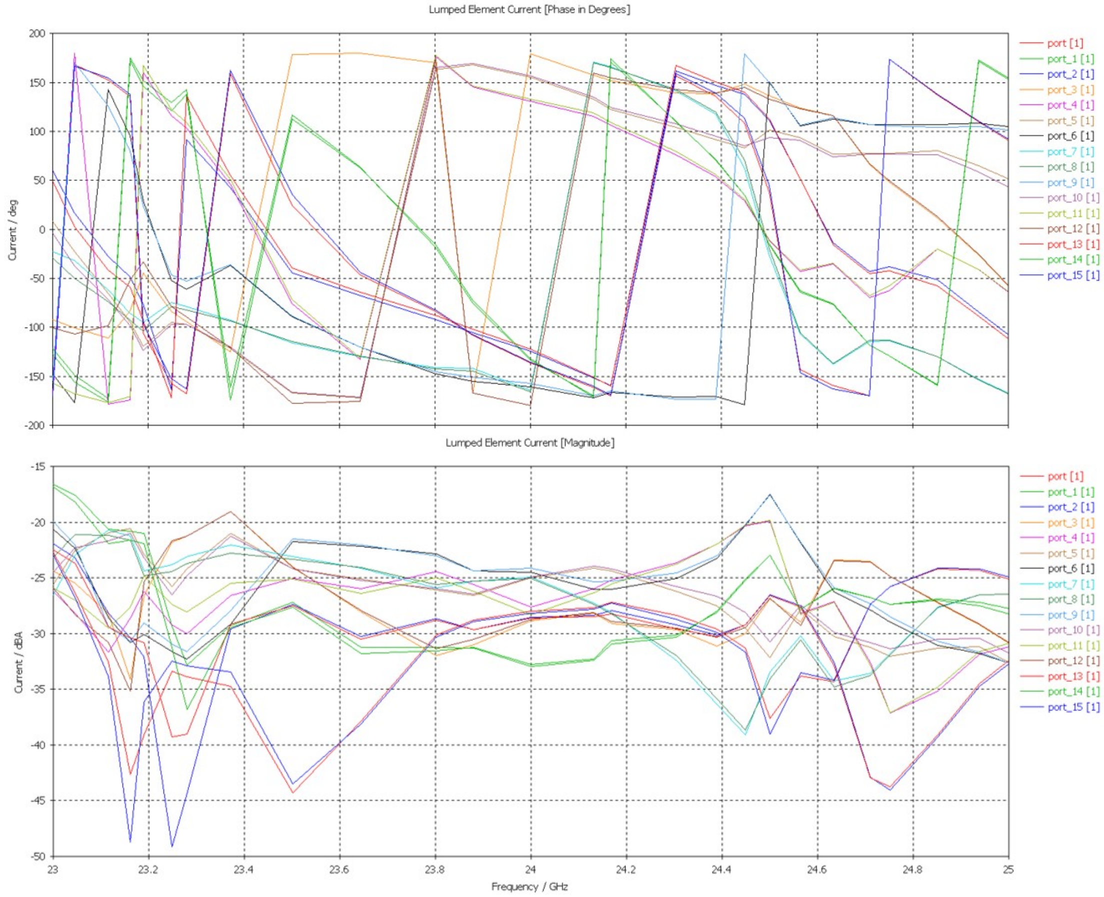

Figure 4.4: Current phases and magnitudes of the CST equivalent implemenation.

As illustrated, the feeding network is no longer operational as it was in ADS, as there are no observable similarities between the currents. It is notable that the symmetry between opposite ports is conserved. This design will not be used as a basis for further CST implementations.

Primary 8-port power divider

Following the ADS implementation, the first design presented in this master thesis is an 8-port power divider supplied by a single coaxial cable as represented in Figure 4.5. The power is then divided into many branches to supply the VEDs equally. This specific feeding network was designed at a larger scale with the feeding pins spaced of $\lambda/2$ instead of $\lambda/4$ as would be expected according to the specifications set out in Section 2.2.4.

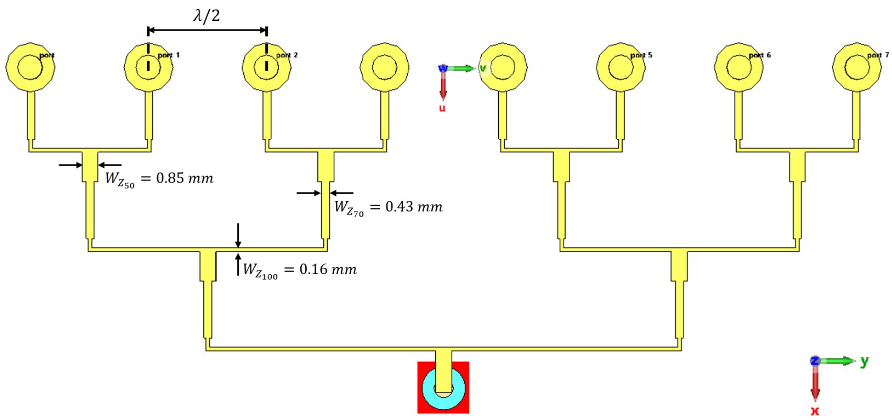

Figure 4.5: Primary model of an 8-port power divider designed using CST.

This first model applies the concepts of the $\lambda/4$ *transformer* with Z_{50}, Z_{70}, and Z_{100} impedances as illustrated. Unfortunately, due to the high coupling between the VEDs and the high reflection coefficient at the various junctions, the resulting distribution of currents is highly uneven and there is no homogeneity between the different ports, as evidenced in Figure 4.6.

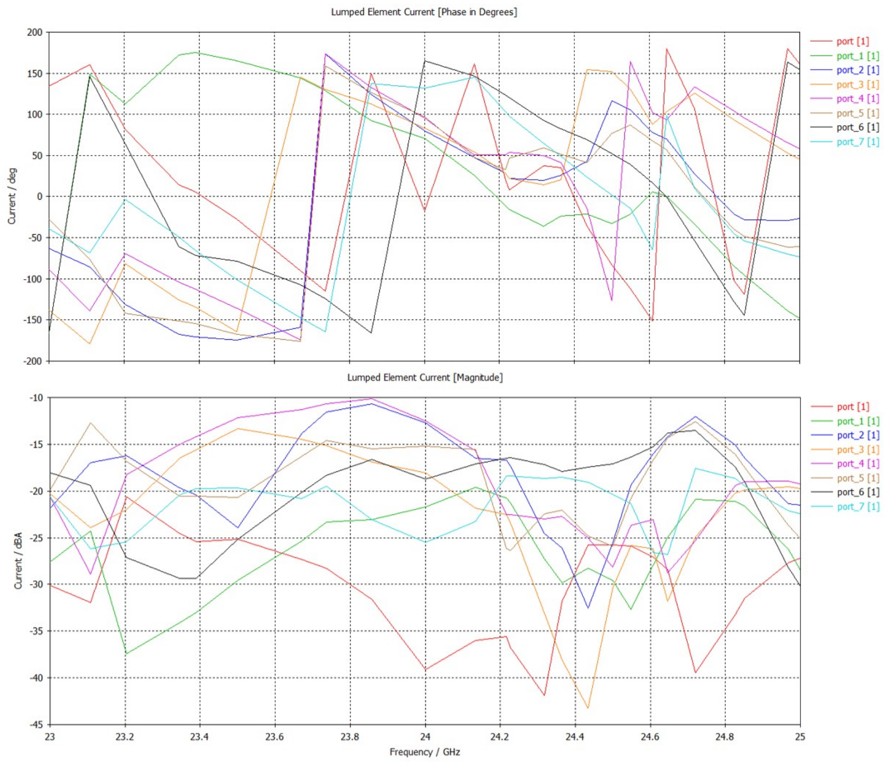

Figure 4.6: Currents phases and magnitudes in the various output ports.

In order to better comprehend the configuration of the prototype, the two 3D views presented in Figure 4.7 offer a global, 3D perspective of the MTS, illustrating its constituent layers and the feeding network extending from its input to its outputs. The views are captured from an identical angle of observation.

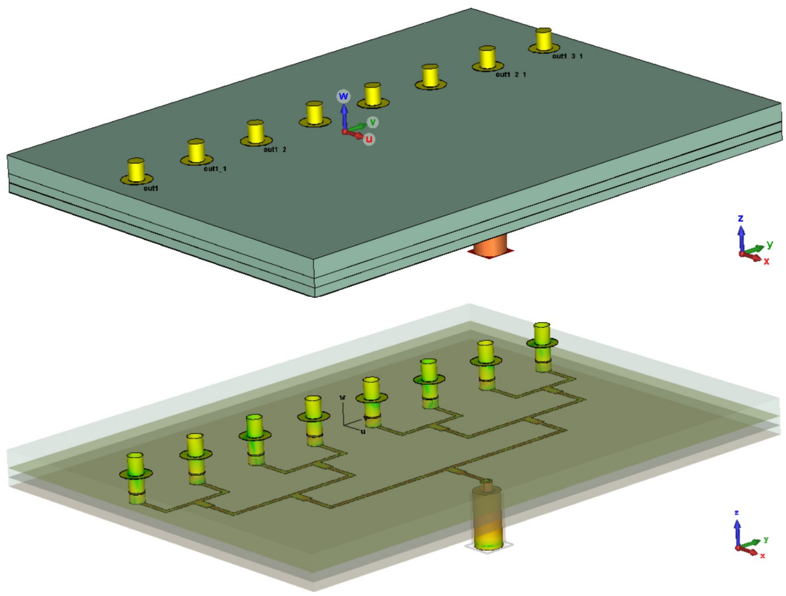

Figure 4.7: 3D perspective views of the entire MTS and its feeding network.

Techniques for decreasing the parasitic effects.

There are many possible causes for the high reflected power observed. Each time the network splits in half or turns to follow the path, the signals encounter what we call *discontinuities* (or junctions). These discontinuities exert an influence on the overall performance of the network, affecting the impedance matching and power distribution between the branches. It is therefore essential to ensure that these discontinuities are properly designed and optimised in order to minimise reflections and losses and guarantee efficient power transmission throughout the network.

In this case, there are three discontinuities that cause parasitic effects in the power transmission. These are the *angle bends junctions*, the *T-junctions* and the *step-width junctions*, as represented with their equivalent circuit in Figure 4.8. The techniques described below will assist in minimising parasitic effects, such as the reflection coefficient at the various junctions. The most effective of these techniques will be applied to the following models of feeding networks. They are inspired from [44], [60], [61] and [62] and tested with CST.

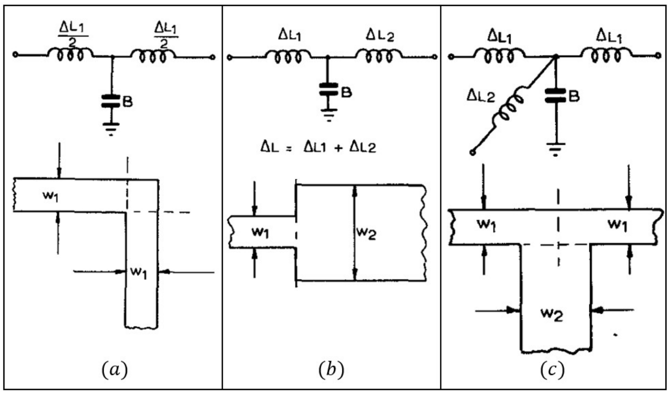

Figure 4.8: Different discontinuities encountered and their equivalent circuit. (a) Right-angled bend, (b) Step-width junction, and (c) T-junction [62].

- **Decreased capacitance technique for bends:** Chamfering the corner decreases the input reflection coefficients. The optimum one was achieved with a 45° chamfer of $l = 1.8 \times width$ as represented in Figure 4.9(a).
- **Step-width junction:** A better transition from the 70.7 Ω to the 50 Ω TLIN with less parasitic effects due to the width variation is achieved by the smooth variation of the width from w_1 to w_2 as shown in Figure 4.9(b).
- **T-junction:** This arrow-shaped TLIN, inspired from [44] and [63], allows a better transition from the 50 Ω impedance to the T-junction of 100 Ω thanks to the smooth variation of the width from w_1 to w_2 as shown in Figure 4.9(c).

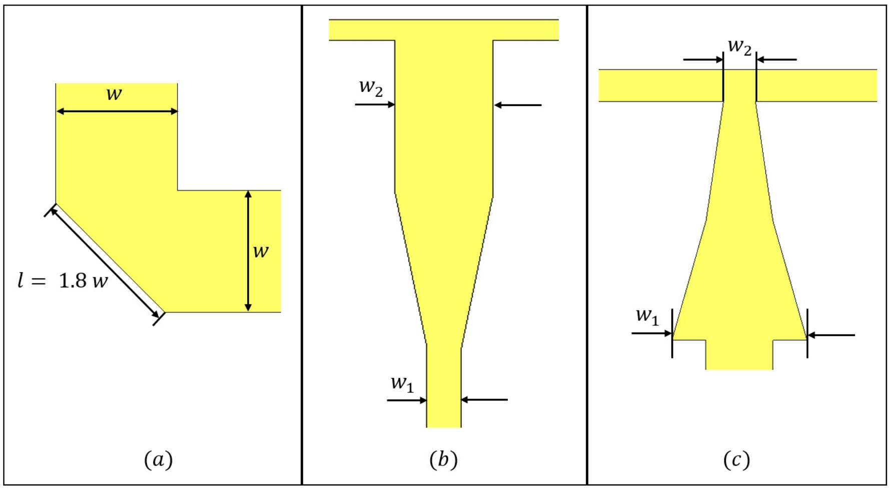

Figure 4.9: Techniques implemented in CST for decreasing parasitic effects due to discontinuities. (a) Chamfered corner, (b) Smooth step from w_1 to w_2 with $w_2 > w_1$, (c) Smooth step from w_1 to w_2 with $w_1 > w_2$.

These techniques were tested in CST, where only the bends and T-junctions were improved and retained for further modelling, as the step-width junction did not give much better results than the original model without any adjustments.

16-port power divider with improved discontinuities

The design presented here uses these various techniques to reduce parasitic effects. Other changes were made to the length/width of certain TLINs to change their line impedance value. A higher impedance would result in less current flowing through that TLIN, a higher impedance means a thinner line. Conversely, a wider line corresponds to a lower line impedance and should carry more current. This was used to achieve similar magnitudes in the different output ports. It is shown in Figure 4.10.

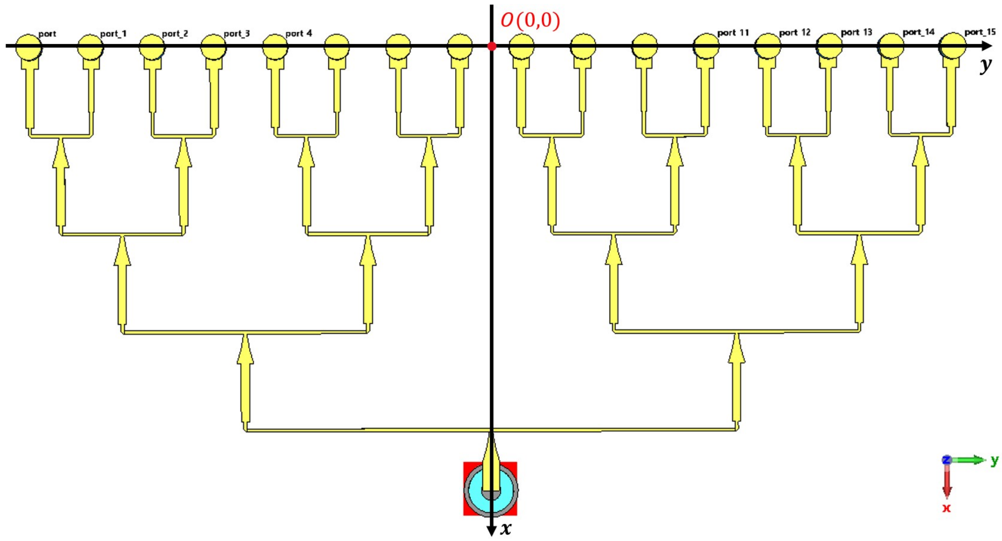

Figure 4.10: 16-port power divider improved with its T-junctions, corners, and magnitude matching.

The results obtained with such a design were promising, but there was still a problem with the phases of the currents in the different output ports. As can be seen in Figure 4.11. The frequency at which the currents are the most in phase is at ≈ 23.5 GHz, it is also the frequency at which the S_{11} is the lowest.

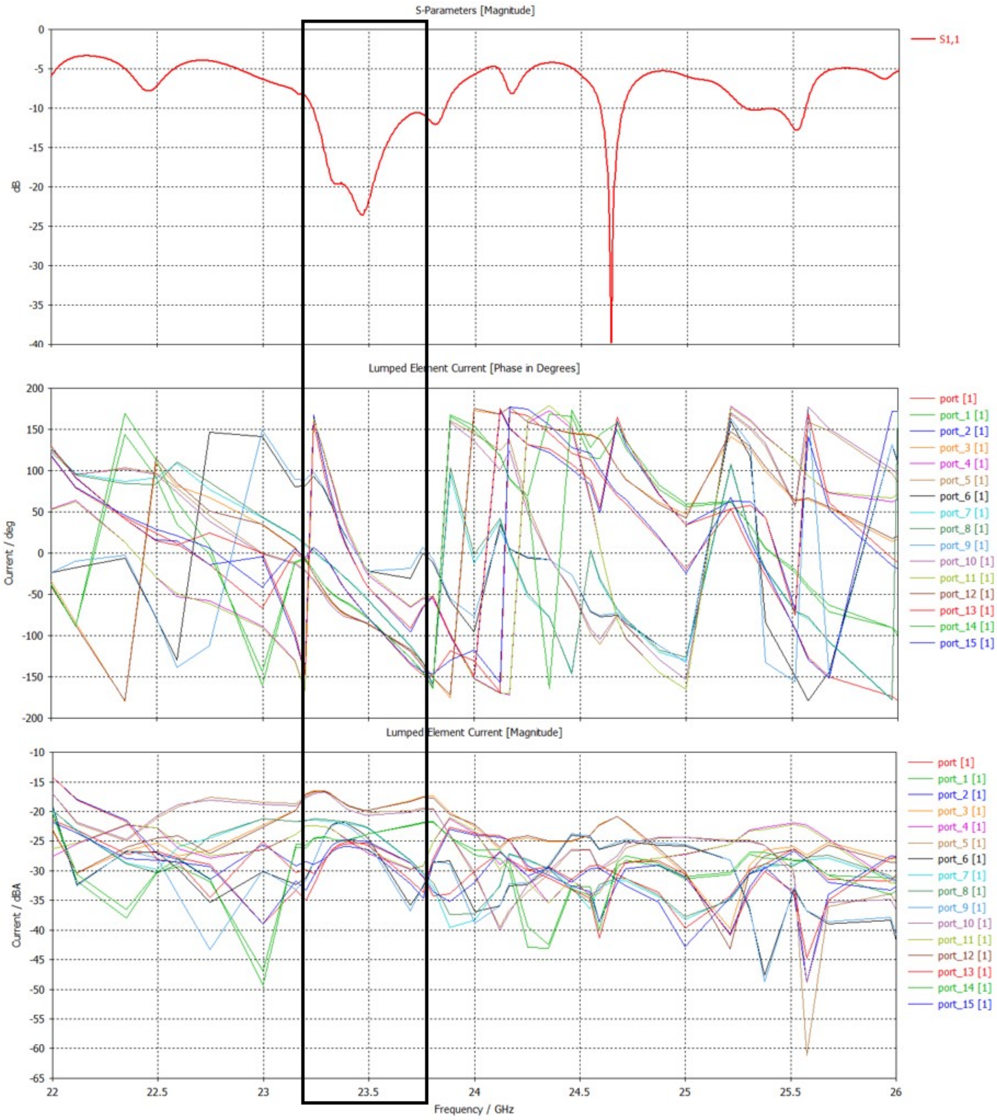

Figure 4.11: S_{11} parameter, current phases, and magnitudes in the different VEDs.

This feeding network is completely symmetrical with respect to the x-axis, which runs through the centre of the feeding network. This means that any changes made to the left part of the network are also made to the right part. This decision was made based on results that verified the left-right symmetry between the ports; they behave similarly in magnitude and phase.

Currents homogeneity quantification

While comparing the currents, it is interesting to quantify their homogeneity. A way to achieve this is by using the *standard phase deviation.* It is given by the formula extracted from [64], and applied to the current phases as:

$$\sigma_\phi = \sqrt{\frac{1}{N}\sum_{i=1}^{N}\left(\phi_i - \bar{\phi}\right)^2} \quad \text{[degree]} \tag{4.1}$$

where ϕ_i is the phase at the i^{th} output port, $\bar{\phi}$ is the mean phase, and N is the number of output ports.

A frequency is deemed *operational* if its associated standard phase deviation is sufficiently low. In the case of 16 VEDs, frequencies with values of $\sigma_\phi \leq 30°$ will be considered to exhibit good performance, whereas those with $\sigma_\phi \geq 60°$ will be considered to exhibit poor performance, and deemed *non-operational.* The choice of quantifying the currents in terms of their phases rather than magnitudes is driven by the necessity of ensuring that the launched SWs exhibit a similar phase, in order to achieve a propagating surface wave that is as planar as possible. Attempting to address the differences in magnitudes tends to present a more challenging task in the design of this feeding network than dealing with the phases.

Final version of the feeding network for a single cell

Mutual coupling between the TLINs themselves or between the feeding pins is inevitable, resulting in unpredictable current phases. To counteract these effects, the width and length of each final TLIN have been tuned to yield currents in the pins that are as similar as possible, as shown in Figure 4.12. In order to find the optimal parameters and minimise the computational time, parameter sweeps and optimisations were performed directly with CST. Parameter sweeps were useful in identifying the range of values for each parameter over which the design performed better. Optimisations were then performed to find the optimum value within this range for each parameter to achieve as similar currents as possible. Following the previous feeding network, this is the revised design with the few changes made to achieve the desired homogeneity between currents. It is the best design achieved for a single cell with 16 VEDs and will be used as the basis for the multi-cell implementations.

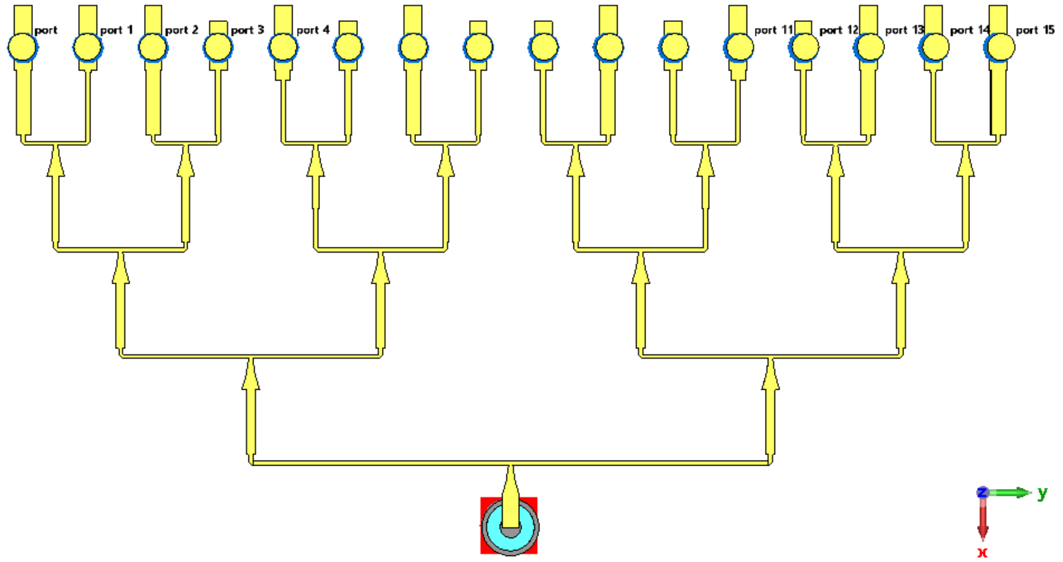

Figure 4.12: Best design obtained for a single cell with 16 VEDs.

For a better understanding regarding the currents homogeneity quantification, Figure 4.13 shows the standard phase deviation obtained in function of the frequency based on the results presented in Figure 4.14. Two frequencies, considered non-operational ($f_1 = 24.5$ GHz) and operational ($f_2 = 23.5$ GHz), are selected from the frequency ranges and according to the S_{11} obtained, to be used for further comparison.

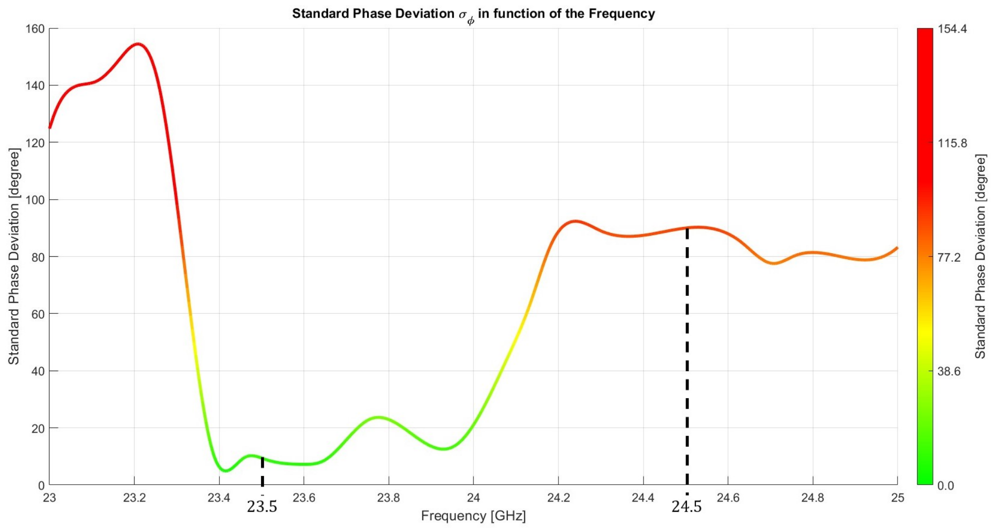

Figure 4.13: Standard phase deviation of the feeding network in function of the frequency.

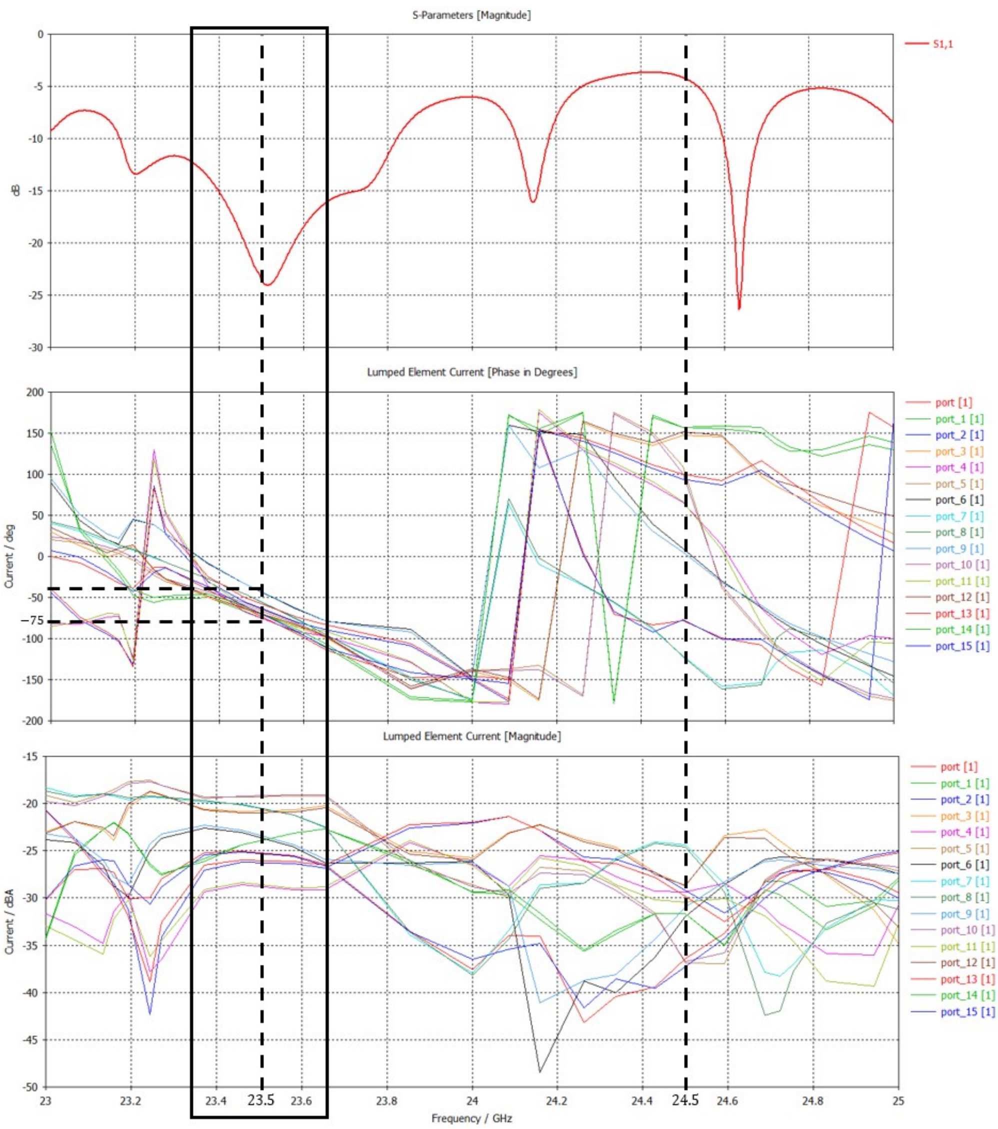

Figure 4.14: S_{11} parameter and current phases in the different VEDs of the improved design.

The design of a functional feeding network now permits a comparison of the planar wavefront generated at the two frequencies mentioned above. The field observed in Figure 4.15 is the x-component of the total propagating field in the dielectric slab. As mentioned earlier, the surface waves generated by the VEDs should propagate along the x-axis and form a wavefront that is as planar as possible. For this reason, the currents flowing through each VED must be sufficiently similar in phase and magnitude so that each generated SW is in phase with each other.

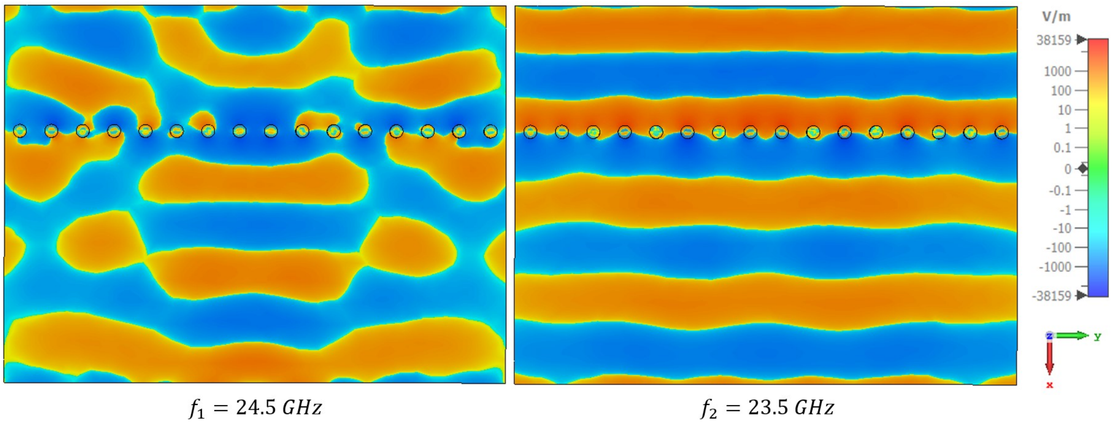

Figure 4.15: Propagating electric field in the dielectric slab of the MTS respectively at $f_1 = 24.5$ GHz and $f_2 = 23.5$ GHz.

These results show the importance of having similar phases for the different currents. At the non-operational frequency, no real planar wave is generated because the launched SWs are destructive to each other during generation. Conversely, the PW generated by the VEDs at the operational frequency $f_2 = 23.5$ GHz is very close to the ideal planar wavefront. One can observe some irregularities in the propagating PW, which could be due to the fact that the phases and magnitudes of the generated SWs are not 100% the same. The black rectangle in Figure 2 represents the BW at which the SWs generated can be approximated by a PW. In this range, the current's behaviour remains identical. The bandwidth can be determined from the x-component of the electric field propagating in the MTS at these distinct frequencies, as illustrated in Appendices C. The range of frequencies between approximately 23.3 and 23.7 GHz provides a suitable PW, resulting in a bandwidth of $0.4/24 = 1.7\%$ instead of the 5% previously stated in [16].

4.1.3 Double feeding network implementation

Following the positive results achieved with the final version of the single feed network, the next step is to assess the impact on the generated fields of incorporating another feeding network. There are now two cells side by side, as will be the case in the prototype to be manufactured. By placing a second feeding network next to the first, the results obtained are quite different, but a more important observation is that the second feeding network senses practically as much current in its VEDs as the one being fed, as can be seen in Figure 4.16.

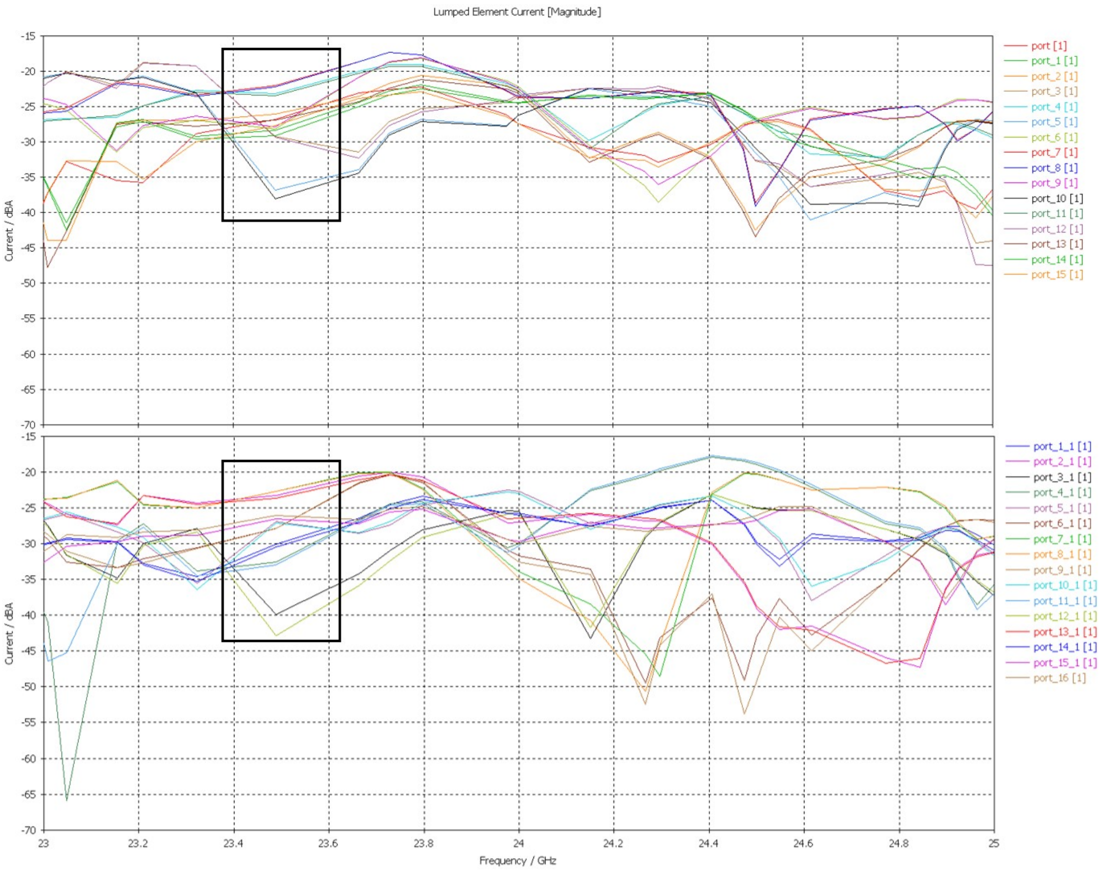

Figure 4.16: Current magnitudes in the fed VEDs and in the VEDs excited by mutual coupling, respectively on the top and bottom of this figure.

There are many possibilities that could explain the changes in the fed VEDs, such as the mutual coupling between the feeding networks, and the changes in the truncation since the substrate is larger than before. Mutual coupling will be investigated with three cells to understand where it comes from and many ways to reduce it will be discussed.

4.1.4 Implementation of a feeding network with three cells

As demonstrated by the double feeding network analysed in Section 4.1.3, the incorporation of an additional cell and its associated feeding network into the prototype leads to significant changes. The final prototype will comprise seven identical cells. To reproduce the effects of having two cells adjacent to the central one, which represents the worst case in terms of coupling, a design with three cells was developed. This also corresponds to the maximum computational capabilities of the computer itself when the patches are added to the simulations.

Origins of the mutual coupling between different feeding networks

A number of simulations have been conducted with the aim of gaining insight into the origin of the coupling. A variety of approaches have been considered, including the use of a perfect electrical conductor (PEC) to simulate a Faraday cage by surrounding the supplied network, as illustrated by the grey wall in Figure 4.17. Monitoring the S-parameters and the currents in the different feeding networks can provide valuable insights into the coupling between them. To further investigate this, an experiment was conducted to examine the dielectric plate by digging into it. This involved analysing whether the main cause of mutual coupling is the SWs propagating on the MTS side and providing power to the other feeds. This second experiment is illustrated in Figure 4.18.

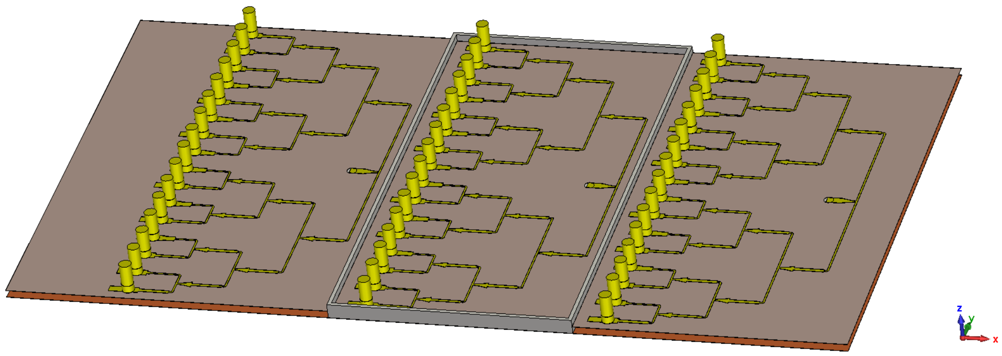

Figure 4.17: PEC cage for reducing mutual coupling from the TLINs.

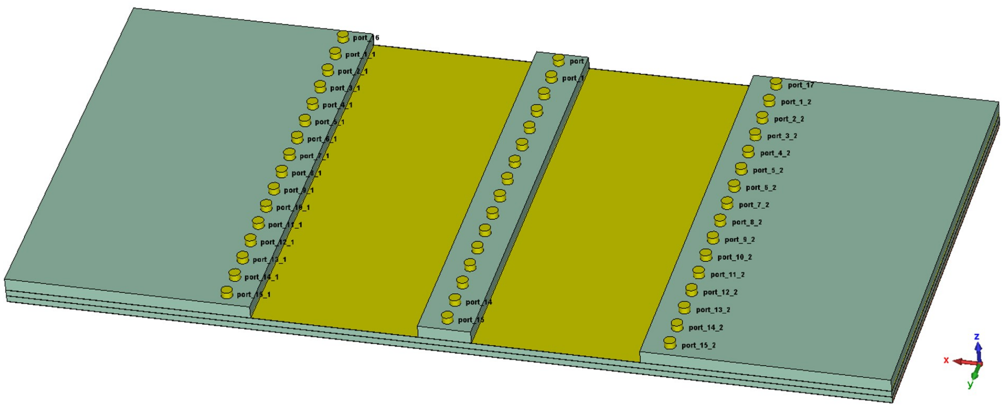

Figure 4.18: Trenches in the MTS substrate for reducing mutual coupling from the SWs propagating on the MTS side.

The results are respectively represented in the Appendices D and E. Both experiments indicate a slight variation in the mutual coupling, accompanied by a reduction in the magnitude of the currents in the other cells. It shows that the currents in VEDs of the different cells are strongly influenced by the powered feeding network, even though they are not powered themselves. It can be concluded that the mutual coupling is a result of both the SWs propagating on the MTS side and the TLINs on the feeding network side, or more specifically, the SW generated by the coaxial cable. The most prevalent mode generated by a coaxial cable is a transverse electromagnetic (TEM) mode that propagates between the two ground layers in this instance. Further analysis of the results with three cells revealed that the cell adjacent to the entry of the feeding network being fed senses a higher current in its VEDs than the other cell that is not being fed. It is likely that this discrepancy can be attributed to the asymmetry of the feeding network, given that the central coaxial cable is situated nearly three times closer to the pins on its right than on its left (see Figure 4.17). Further details about the magnitudes of the currents can be found in Appendices D. For reference, *cell 1* is the cell on the right and *cell 2* is the cell on the left (relative to the Figure 4.17).

Solutions for reducing mutual coupling

The first method investigated to reduce this mutual coupling is the use of blind vias between the two ground planes, which act as a reflective wall to separate the different feed networks. It is illustrated in Figure 4.19 and was optimised by varying many parameters such as the position of the vias wall, the size of the vias, and the spacing between the vias.

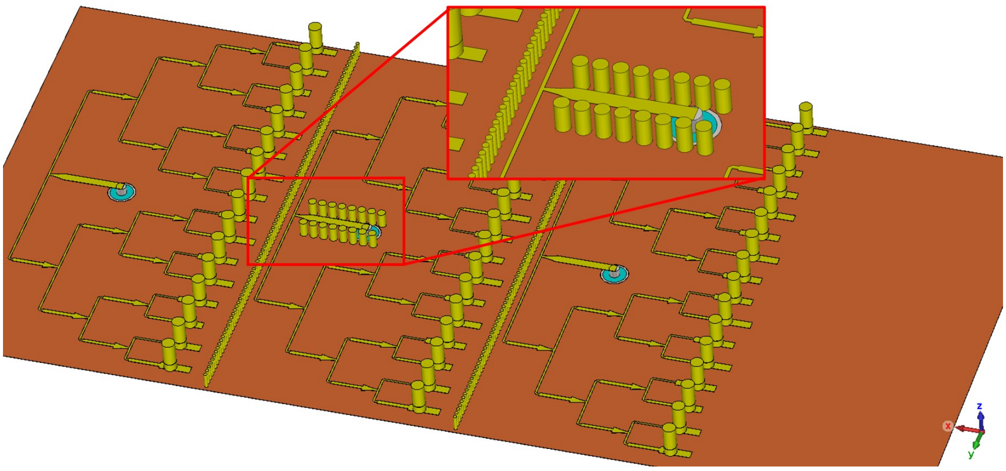

Figure 4.19: Blind vias used as a reflective wall for separating the adjacent feeds.

It can be observed that the use of vias serves two distinct purposes. Firstly, they act as a *reflecting wall*, separating the different feeding networks. Secondly, they function as a *waveguide* at the output of the coaxial cable, reducing the dispersion of the field. The results obtained using this method to reduce mutual coupling are promising, although not perfect, since the coupling from the propagating SWs within the top dielectric slab cannot be avoided and will remain. However, the results shown in Figure 4.20 are satisfactory in both magnitude and phase around the frequency $f = 23.8$ GHz. The selected frequency differs from the initially selected 24 GHz operating frequency. However, there is some flexibility regarding the frequency used, and the design can be rescaled later towards the target frequency if necessary.

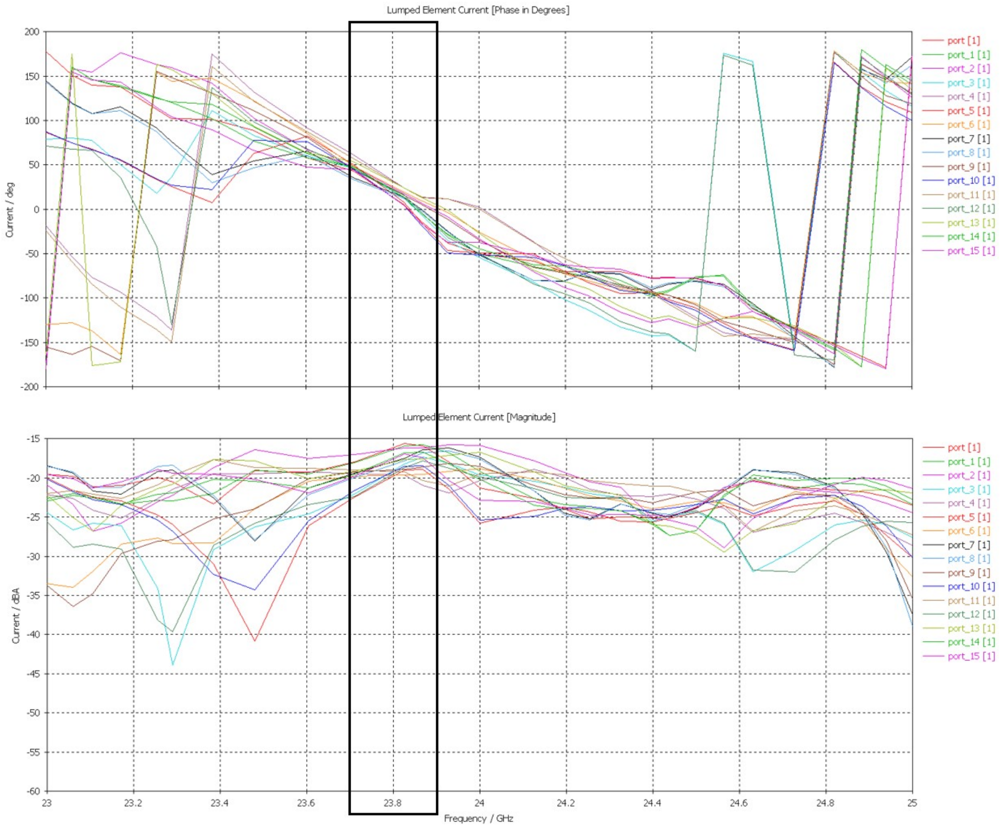

Figure 4.20: Phase and magnitude of the currents in the different VEDs of the excited feeding network.

A difference of about 5 and 10 dB is observed in the magnitudes of the currents in the other two feeding networks, which can be seen in the Appendices F. Now that the results for several adjacent cells are likely to be statistically significant, the patches can be added to observe their effect on the results and the emerging radiation pattern. The EEP obtained will determine whether the results were indeed convincing.

4.1.5 Three-cell feeding network with additional patches

The array of patches being repeated all along the MTS that was used for the simulations in [16] did not take into account the concomitant presence of the MTS patches and the VEDs. It results in the removal of some patches that may change the radiation pattern obtained. The MTS design is now complete for three cells out of seven, as can be seen in Figure 4.21.

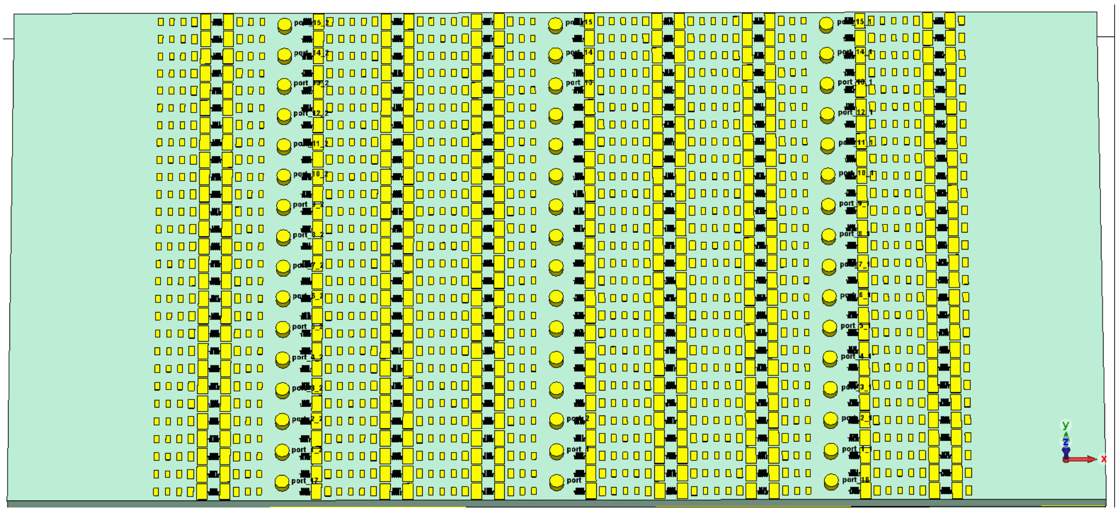

Figure 4.21: Metasurface patches displayed on the three-cells MTS.

The radiation pattern obtained from the patches excited over three cells is expected to have a shape similar to a rectangle, but less sharp than that expected with more cells. To get a clearer idea, Figure 4.22 shows a 3D view of the radiation pattern.

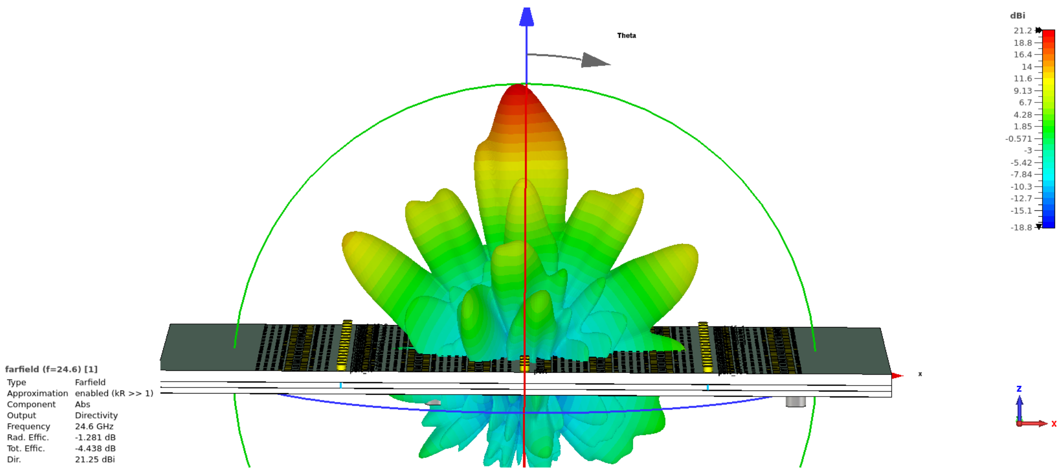

Figure 4.22: 3D radiation pattern obtained with the MTS designed.

Figure 4.23 shows a 1D comparison of the radiation pattern obtained directly in CST with this specific design and the ideal one simulated in MATLAB either with unitary current weights, or simulated with an infinite wall of VEDs.

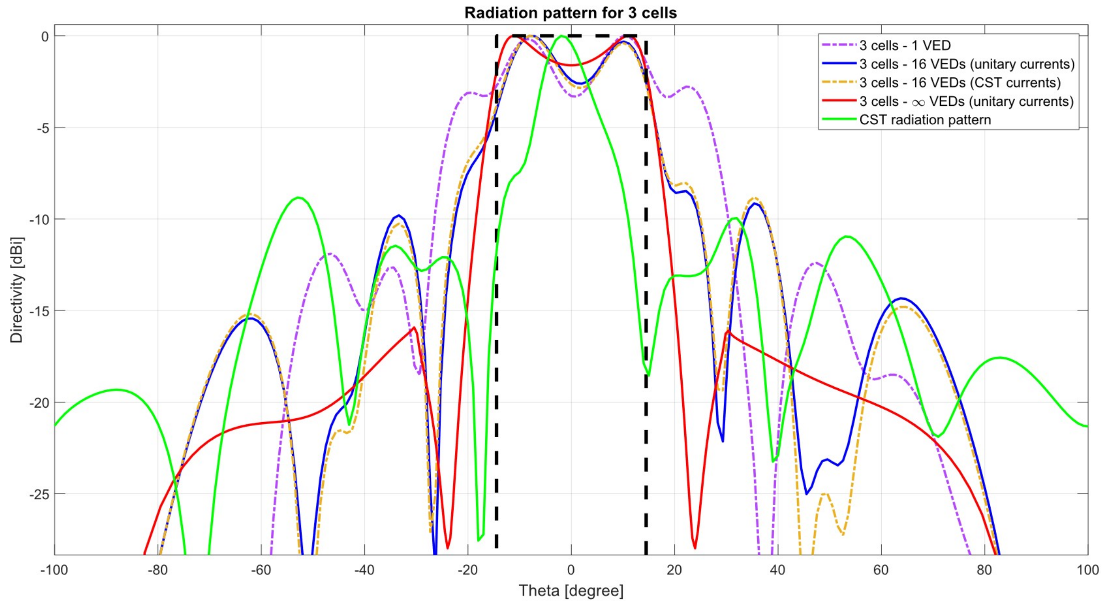

Figure 4.23: Radiation patterns with 3 cells compared to the ideal EEP (black dashed line).

The radiation pattern obtained with the CST simulation only has an angular width of $\approx 10°$ while it should be $28.96°$, as derived in Section 2.2.4. The quasi-rectangular shape of the radiation pattern desired is not yet achieved. However, it is worth noting that the radiation pattern's zeros are similarly placed in both CST and MATLAB simulations. The sidelobe level (SLL) is ≈ 10 dB lower than the main lobe magnitude, which is also similar to the magnitudes observed in the MATLAB simulated radiation patterns.

There are numerous potential explanations for the discrepancy between the anticipated and actual radiation patterns observed in CST. Firstly, the VEDs are not included in the MATLAB simulations; they are superimposed by patches, which are therefore removed in CST and do not contribute to the total radiated field. Secondly, the coupling between the cells also affects the behaviour of the PW, which is not as planar as expected and does not excite each patch in the same way. Finally, the asymmetry observed in the radiation pattern provided by CST could be due to the asymmetry of the feeding network itself, which is immutable for an odd number of cells.

4.1.6 Final design after discussion with the manufacturer

The final design presented in this work was developed after consulting with the manufacturer. Some modifications were necessary to align with the manufacturing conditions, including:

- The blind vias in between the two ground planes introduced in Section 4.1.4, are not feasible and must be removed. It is necessary to consider alternative solutions for reducing the mutual coupling on the feeding network side. The resulting feeding network, designed with the objective of minimising mutual coupling by increasing the distance between adjacent feeding networks, is illustrated in Figure 4.24.

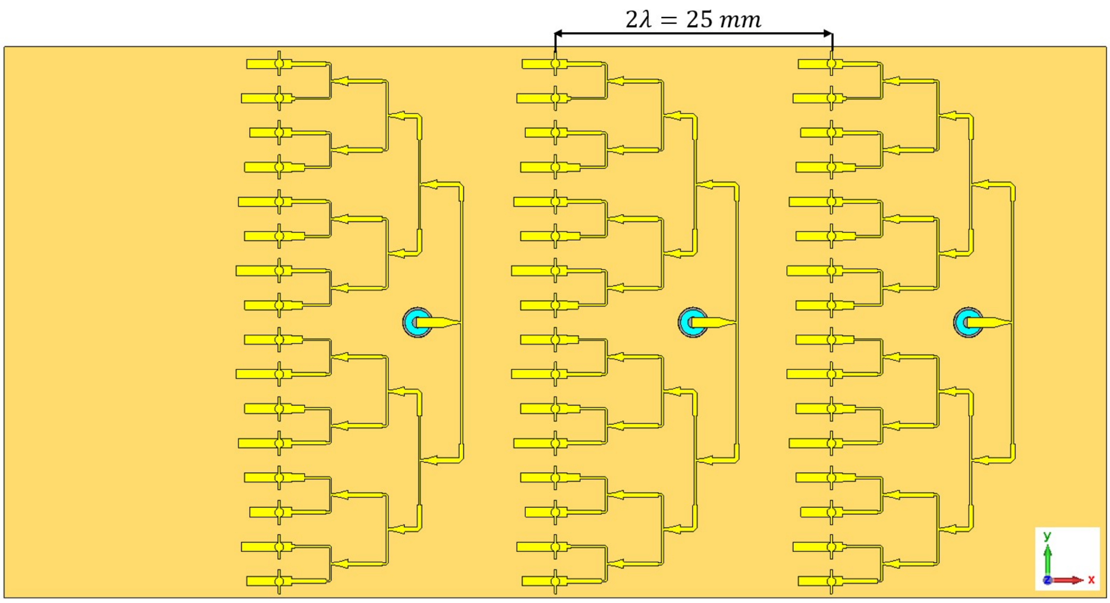

Figure 4.24: Feeding network without the blind vias for reducing the coupling.

- The minimum width of the conductor should be 100 μm, while the width of the meander patches was approximately 26 μm. The meander patches were therefore redesigned to match the requirements.

- It is not possible for the vertical pins (VEDs) to pass through the MTS; they must be flush with the MTS. The top view of the MTS with the patches and the flush pins is shown in Figure 4.25. An additional modification was implemented by reducing the radius of the initial VEDs, thereby enabling the incorporation of two patches per cell that were previously excluded.

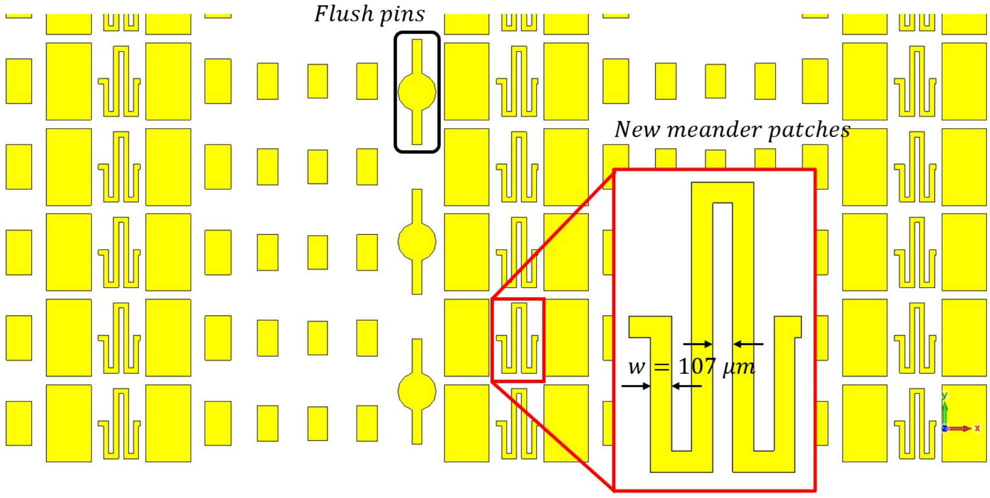

Figure 4.25: Top-view of the MTS with the new meander lines and flush pins.

The results provided by the ports in the VEDs such as the current phases, magnitudes and S-parameters for this design can be found in Appendices G.1. The noteworthy finding is that the radiation patterns obtained with the new patches exhibit greater similarity to the desired patterns than those obtained prior to adjustment. This results in a quasi-rectangular radiation pattern, as illustrated in Figure 4.26.

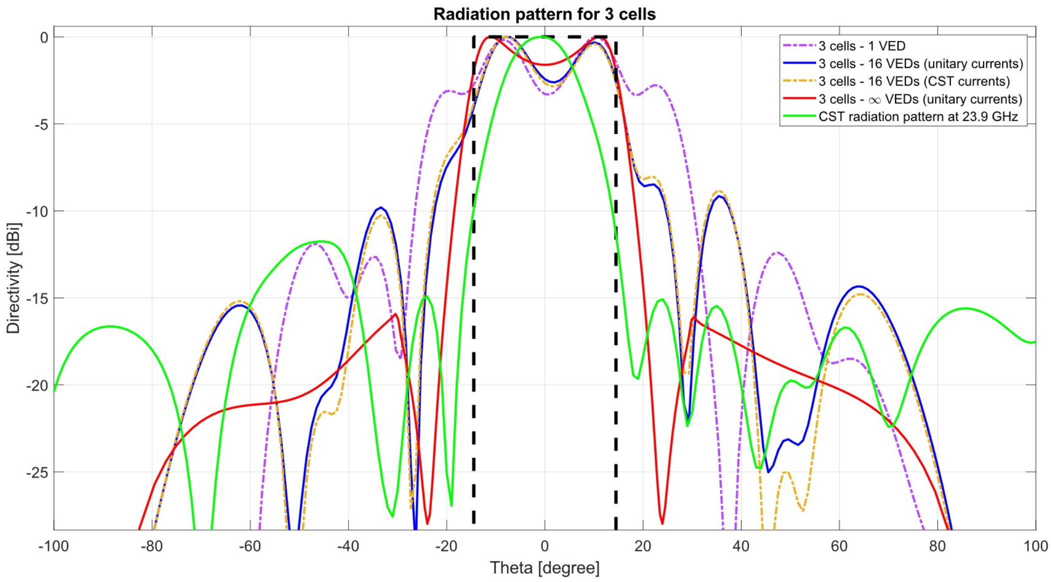

Figure 4.26: Radiation pattern obtained with CST at the frequency of $f = 23.9$ GHz compared with simulated ones in MATLAB.

It can be seen that the angular width of $\approx 18°$ obtained is greater than that previously observed. The bandwidth (BW) obtained with this design can be determined by looking at the different radiation patterns obtained for a range of frequencies. The radiation patterns obtained in this range are shown in Figure 4.27.

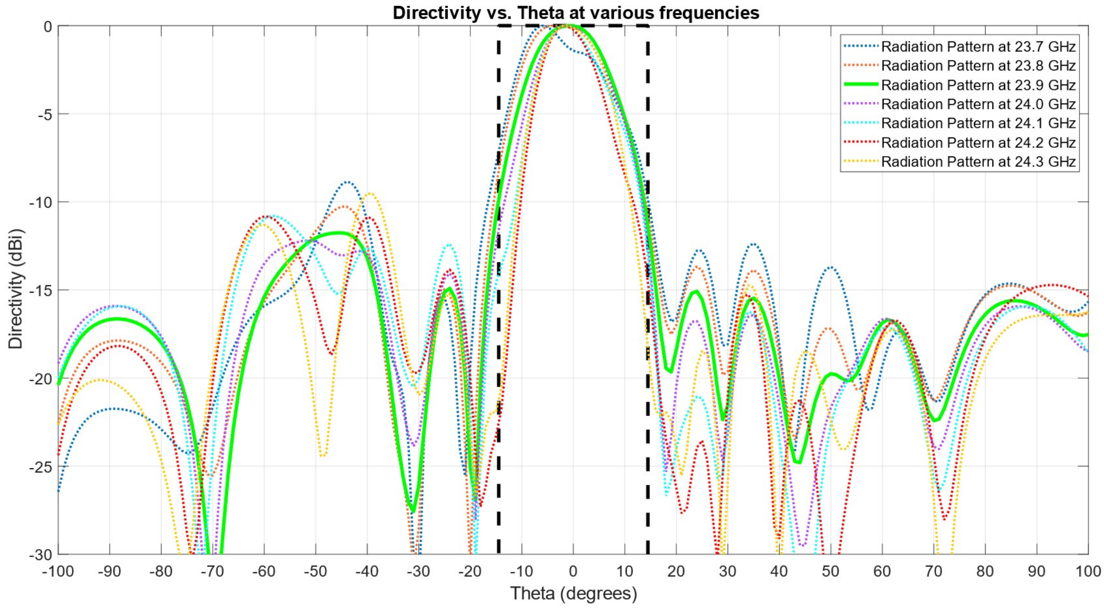

Figure 4.27: Comparison of the radiation patterns obtained at many frequencies.

The optimal bandwidth (BW) for this design is between 23.7 and 24.3 GHz, despite the angular width diminishing as the frequency increases. The resulting bandwidth is thus $0.6/24 = 2.5\%$, which is an improvement over the previous result. The sidelobe level (SLL) is observed to be at a minimum at the frequency of $f = 23.9$ GHz, exhibiting a value that is approximately 12 dB lower than that of the main beam. An additional 3D view of the radiation pattern is provided in Appendices G.2 to compare it with the one previously obtained.

Further details regarding the propagating field at the specified frequency of $f = 23.9$ GHz can be found in Appendices G.3. The analysis employs both the spectral field representation and a 2D graphical representation of the x-component propagating field.

Power losses and radiated

A useful tool provided by CST enables the identification of losses and their sources, while simultaneously providing the total radiated power. This information can be obtained for all frequencies within the scope of the analysis, as illustrated in Figure 4.28.

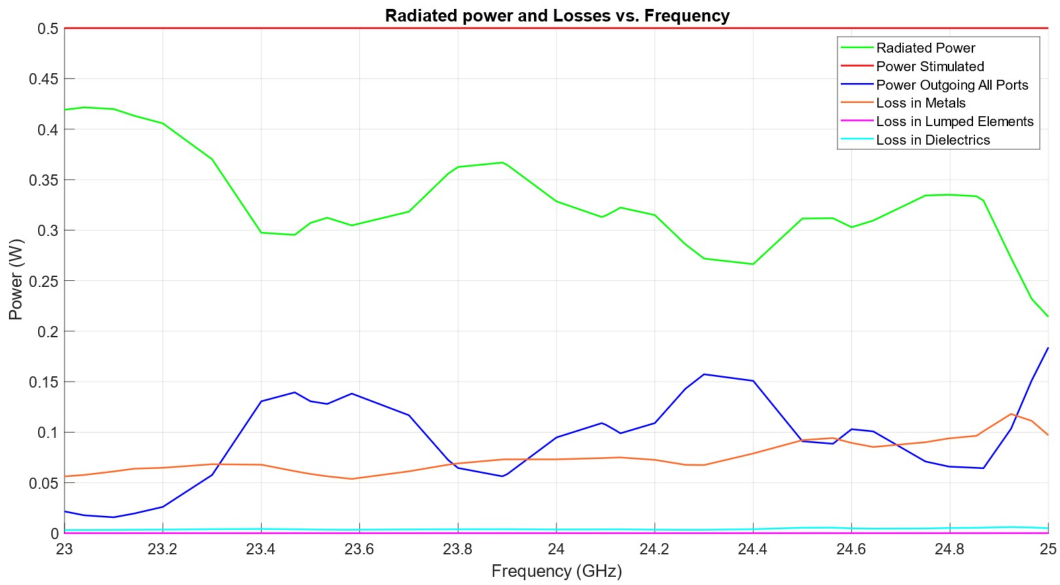

Figure 4.28: Total radiated power and sources of loss.

The primary source of loss that results in a reduction of the radiated power is the outgoing power from all ports. This is attributable to both the reflection coefficient at the input port (i.e. the matching of loads) and the high mutual coupling between adjacent cells where power flows and is lost. As evidenced by the S-parameters, the power transmitted from the fed port to two other coaxial cables is not negligible and represents the primary source of discrepancies in the radiation pattern.

Despite the numerous attempts to reduce this mutual coupling, the desired results have not been achieved. Decoupling methods, including the use of electromagnetic band-gap (EBG) structures inspired from [65] and [66], have been implemented but have not yielded more favourable outcomes. Another unsuccessful method was inspired by the reflection structure of Yagi-Uda antennas, as described in [67], [68].

4.2 CST and MATLAB simulations based on spectral field representation

Based on Section 2.3.3, an analysis of the electric field in the middle plane ($y = 0$) can now be conducted since the equations describing the radiated field in the spatial domain due to VEDs have been established. It can be expressed as follows:

$$\mathbf{E}_z(x, y = 0) = \mathbf{E}_{zx}(x, y = 0) + \mathbf{E}_{zy}(x, y = 0) \tag{4.2}$$

The diverse cases outlined in Section 2.3.3 can be evaluated in comparison to one another in order to analyse the behaviour of the fields when employing the current weights extracted in CST. This is achieved through the numerical integration of the electric field equations and the utilisation of the Green's function associated with the VED along $\hat{z}$.

4.2.1 Infinite number of VEDs

In this first case, one wants to observe how the fields behave if an infinite wall of VEDs is launching SWs. It is shown in Figure 4.29.

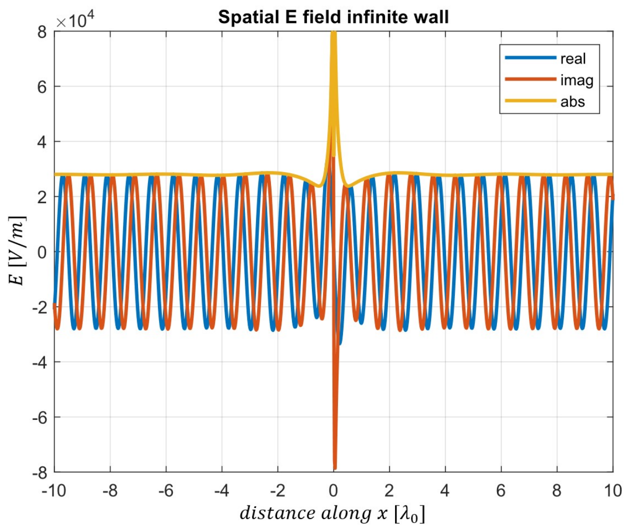

Figure 4.29: Field E along the x-axis with an infinite wall of VEDs.

It can be observed that for an infinite number of VEDs (with N = 1000 considered), the propagating field amplitude remains constant along the x-axis. In the next case, a finite number of VEDs is considered, and it is therefore of interest to ascertain how the field should behave and whether the 16 VEDs are a sufficient number to approximate an infinite wall of VEDs.

4.2.2 Unitary versus CST weights

This second case with a finite number of 16 VEDs evaluates if the number of VEDs chosen is sufficient to approximate the infinite wall simulated before, it also shows the difference between unitary current weights and simulated ones from CST. The model chosen to observe the impact of the currents homogeneity on the propagating field is the one described in Section 4.1.2. The x-component of the electric field propagating along the x-axis is evaluated at the two frequencies previously discussed in that section, designated as $f_1 = 24.5$ GHz and $f_2 = 23.5$ GHz, respectively. Their respective field magnitudes are illustrated in Figure 4.30.

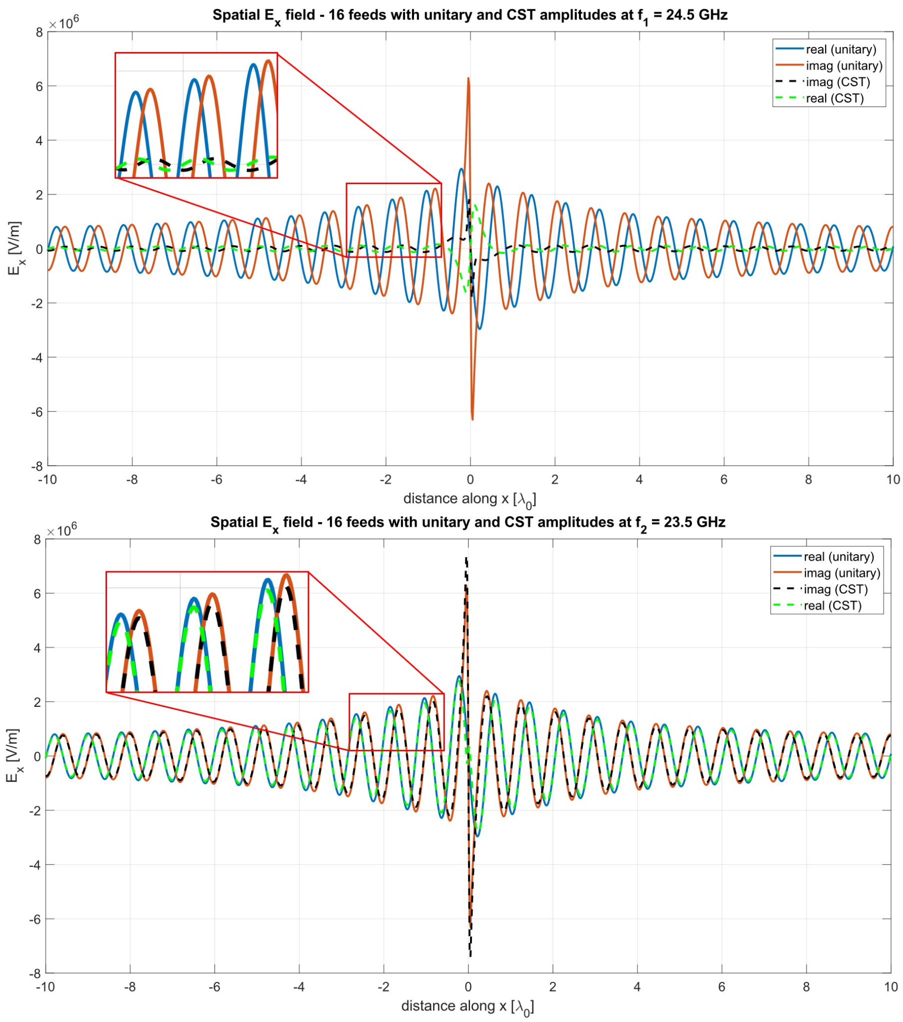

Figure 4.30: Comparison of the E_x propagating along the x-axis for 16 VEDs with unitary and extracted weights from CST, respectively at an operational and non-operational frequency is presented.

It can be observed that the x-component of the field along the x-axis exhibits a markedly different behaviour at the non-operational frequency f_1 in comparison to the E_x field obtained with unitary weights. Conversely, at the frequency f_2, the weights extracted from CST yield an E_x that behaves in a manner that is nearly identical to that of the unitary weights. This result confirms that the x-component of the field along the x-axis propagates as expected. One can also analyse the y-component of the electric field propagating in the MTS, as shown in Figure 4.31.

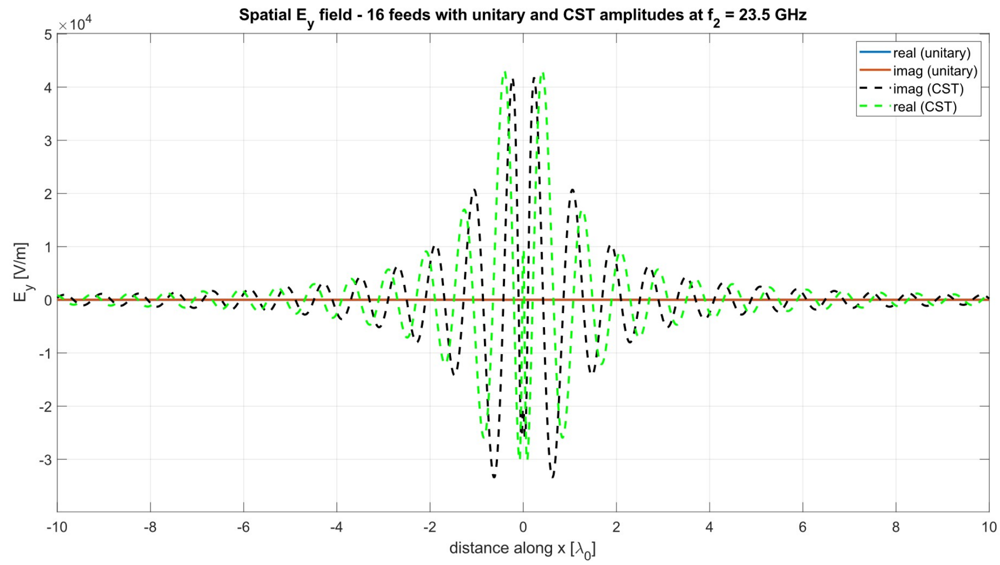

Figure 4.31: Comparison of the E_y propagating along x-axis for 16 VEDs with unitary and simulated weights at the operational frequency $f_2 = 23.5$ GHz.

One can observe that the amplitudes are quite different from what is expected, they should tend to be very close to zero. The important point here is to ensure that the E_y component is negligible compared to E_x. A ratio of $\frac{E_x}{E_y} \approx 200$ is reached after a distance of $2\lambda_0$, and overall the E_y component decreases faster than the E_x component.

The MTS antenna aims to have a zero E_y component along the $y = 0$ axis. The antisymmetry observed in Figure 4.32 indicates that the E_y component along the $y = 0$ axis should be close to zero. However, as evidenced by the MATLAB simulations, this is not the case, as achieving perfect symmetry without perfectly synchronised SWs is challenging. As stated in Section 4.1.2, the currents in port$_i$ and port$_{16-i}$ are assumed to be homogeneous. However, the actual currents exhibit a greater degree of inhomogeneity than is necessary to achieve the desired result of $E_y = 0$ along that axis.

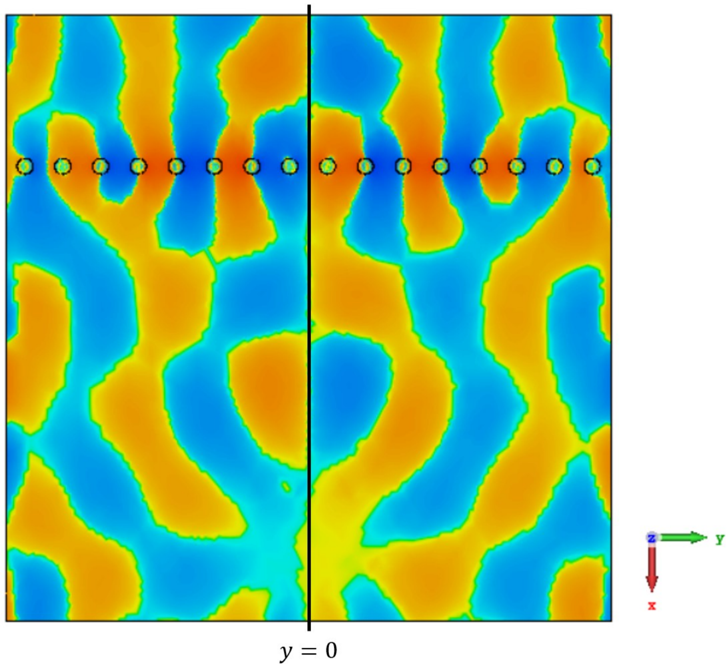

Figure 4.32: Antisymmetry of the E_y component at the $y = 0$ axis in the MTS substrate.

Chapter 5

Conclusion and future work

5.1 Conlusion

This research took place in the framework of a project aiming at the generation of sparse regular arrays, i.e. with spacing larger than the wavelength, at the expense of a reduced field of view. This suppose the generation of quasi-rectangular embedded element patterns.

The aim of this work was to realise the feeding network of a sparse-array MTS, but also to validate its performance by comparing 2D simulations carried out in a previous work with 3D simulations carried out with CST. Before these results could be compared, a large number of feeding networks were designed to meet specific requirements. Rows of 16 vertical elementary dipoles (VEDs) fed by the network allowed the generation of a planar surface wave that would propagate uniformly along the x-axis to excite the numerous patches arranged on the MTS. To ensure that the surface waves (SWs) generated by the different VEDs were in phase, it was important to measure the currents directly in the VEDs to observe their homogeneity.

The different models of the feeding network were designed step by step, understanding which parameters could be tuned to meet the requirements, and based on the literature review. The path to these results involved several key stages, including parametric testing and optimisation. First, a theoretical model of the feeding network was constructed based on transmission line theory. The model was then subjected to a series of parametric tests, during which design parameters such as the width and length of the transmission lines were adjusted in order to control the magnitude and phase of the currents in the VEDs. These tests were essential to understand how each parameter affected the behaviour of the MTS. Once the homogeneity of the currents was maximised, a spectral analysis could be carried out to determine whether the propagating field was consistent and whether the embedded element pattern generated by the MTS was similar enough to the predicted one.

Throughout this research, significant progress has been made towards achieving the stated objectives. The results show satisfactory success, with a good concordance between the 2D and 3D simulations in terms of radiation patterns, but also in terms of generation of the surface wave within the MTS, where the propagating fields behaved as expected from the simulations. The transition to 3D simulations was an essential step in the continuation of the *FITNESS project* and before any structure could be manufactured, as it takes into account the full spatial configuration and interactions within the MTS.

Although the results are promising and the full-wave simulations suggest that the design would perform well in practice, final validation through physical testing in an anechoic chamber could not be completed within the timeframe of this master thesis. The manufacturing process required to produce the prototype typically takes three months, preventing the planned tests from being carried out. However, the consistency between the 2D and 3D simulations strongly indicates that the feeding network and the MTS itself would perform as expected in practical scenarios.

5.2 Future work

Despite this satisfactory outcome, a number of challenges and areas for further research were identified. One of the main challenges was the issue of mutual coupling between the cells of the sparse-array MTS. Mutual coupling, which refers to the interaction between adjacent cells in the array, can cause deviations in the radiation pattern and reduce performance at certain frequencies. However, mutual coupling is already included in our full-wave simulations. It is likely that mutual coupling contributed to the small radiation pattern variations observed in the simulations.

For future work, addressing the issue of mutual coupling on the feeding network side should be a priority. Potential approaches could include redesigning the physical layout of the VEDs to minimise coupling, or introducing decoupling elements to the feeding network or in between the two ground planes. Furthermore, it would be advantageous to investigate alternative feeding network designs that are less prone to mutual coupling between consecutive ports. A further avenue for future research will be to conduct physical testing in an anechoic chamber once the prototype is available. This will provide empirical validation of the simulated results and additional insights into the performance of the feeding network. Furthermore, the full-wave simulations conducted with CST were constrained by the associated computational expense. The use of a more powerful computer would have enabled the simulation of a MTS with seven cells, rather than the three cells that were used. Another idea for future work is to implement beam scanning in 2D (θ, ϕ). This will allow the metasurface to cover a larger scanning area, thereby enhancing its ability to adapt to a variety of scenarios.

In conclusion, the primary objectives of this thesis have been successfully achieved, demonstrating the feasibility and effectiveness of a feeding network design for a sparse-array metasurface. Although the final physical validation is still pending, the significant concordance between the 2D and 3D simulations provides substantial confidence in the design's performance. It is essential to address the challenges of mutual coupling on the feeding network side and to complete the experimental testing in order to further refine and enhance this innovative metasurface technology.

Bibliography

[1] F. Ahmed, K. Singh, K. P. Esselle, and D. Thalakotuna, "Metasurface-driven beam steering antenna for satellite communications," *5th Int. Conf. Commun., Signal Process. Appl. (ICCSPA)*, 2022, pp. 1–5.

[2] N. ud Din, A. Afzaal, J. Tahir, and N. Hafeez, "Electronic beam scanning for radar applications," *8th Int. Conf. High-Capacity Opt. Networks Emerging Technol.*, 2011, pp. 355–358.

[3] R. Mittra, D. Oueslati, A. Nasri, R. K. Arya, and A. Ghalib, "Fixed- and scanned-beam antenna arrays for 5G applications," in *Signals and Commun. Techn.* Springer, Jan. 2021, pp. 145–207.

[4] *What is a phased array antenna?* Jun. 2020. [Online]. Available: `https://www.everythingrf.com/community/what-is-phased-array-antenna`.

[5] N. T. Huong, "Beamforming phased array antenna toward indoor positioning applications," in *Intech Open eBooks*, Intech Open, Sep. 2020.

[6] O. Quevedo-Teruel *et al.*, "Roadmap on metasurfaces," *Journal of Optics*, vol. 21, no. 7, p. 073 002, Jul. 2019.

[7] S. Maci, "Design of modulated metasurface antennas," *2017 IEEE Int. Symp. Antennas Propag. & USNC/URSI Nat. Radio Sci. Meeting*, San Diego, CA, USA, 2017, pp. 1939–1940.

[8] M. Bodehou, E. Martini, S. Maci, I. Huynen, and C. Craeye, "Multibeam and beam scanning with modulated metasurfaces," *IEEE Trans. Antennas Propag.*, vol. 68, pp. 1273–1281, Mar. 2020.

[9] J. Dessy, "Metasurface antennas for radar applications," M.S. thesis, Univ. Cath. Louvain., June 2023.

[10] *Metasurface technologies*, Jun. 2023. [Online]. Available: `https://fitness-pathfinder.eu/technology/#metasurface`.

[11] Dassault Systèmes, *CST studio suite 2022*, 2022. [Online]. Available: `https://www.3ds.com/products-services/simulia/products/cst-studio-suite/`.

[12] Keysight Technologies, *Advanced Design System (ADS)*, PathWave Design, 1985. [Online]. Available: https://www.keysight.com/en/product/cad/advanced-design-system-ads.

[13] C. Craeye and C. Oestges, *LELEC2910 - antennas and propagation*, Lecture note, Chapters 1-2, 2023-2024.

[14] P. Bevelacqua, *Antenna-theory.com - field regions*, 2024. [Online]. Available: https://www.antenna-theory.com/basics/fieldRegions.php.

[15] W. L. Stutzman and G. A. Thiele, *Antenna Theory and Design*, 3rd. John Wiley & Sons, 2012, ISBN: 978-0470576649.

[16] J. Dessy, M. Bodehou, J. Cavillot, and C. Craeye, "Sparse-array metasurface for beam scanning," accepted for publication in IEEE Trans. Antennas Propag., Dec. 2023.

[17] A. Ali, A. Mitra, and B. Aïssa, "Metamaterials and metasurfaces: A review from the perspectives of materials, mechanisms and advanced metadevices," *Nanomaterials*, vol. 12, no. 6, p. 1027, Mar. 2022.

[18] *Metamaterials*, http://nanolase.fis.unical.it/index.php/research/metamaterials, Accessed: Jul. 23, 2024.

[19] G. Fan, K. Sun, Q. Hou, Z. Wang, Y. Liu, and R. Fan, "Epsilon-negative media from the viewpoint of materials science," *EPJ Applied Metamaterials*, vol. 8, p. 11, Apr. 2021.

[20] W. Contributors, *Poynting vector*, *Wikipedia*, https://en.wikipedia.org/wiki/Poynting_vector, Accessed: Aug. 14, 2024.

[21] S. A. Tretyakov and C. Simovski, *Introduction to metamaterials and nanophotonics*, Lecture notes, Chapter 4, 2023-2024.

[22] W. Contributors, *Bandwidth (signal processing)*, May 2024. [Online]. Available: https://en.wikipedia.org/wiki/Bandwidth_(signal_processing).

[23] W. Contributors, *Uncertainty principle*, *Wikipedia*, https://en.wikipedia.org/wiki/Uncertainty_principle, Accessed: Jul. 23, 2024.

[24] M. A. Francavilla, E. Martini, S. Maci, and G. Vecchi, "On the numerical simulation of metasurfaces with impedance boundary condition integral equations," *IEEE Trans. Antennas Propag.*, vol. 63, no. 5, pp. 2153–2161, 2015.

[25] B. H. Fong, J. S. Colburn, J. J. Ottusch, J. L. Visher, and D. F. Sievenpiper, "Scalar and tensor holographic artificial impedance surfaces," *IEEE Trans. Antennas Propag.*, vol. 58, no. 10, pp. 3212–3221, Oct. 2010.

[26] M. Bodehou, C. Craeye, E. Martini, and I. Huynen, "A quasi-direct method for the surface impedance design of modulated metasurface antennas," *IEEE Trans. Antennas Propag.*, vol. 67, no. 1, pp. 24–36, Jan. 2019.

[27] W. Contributors, *Method of moments (electromagnetics)*, *Wikipedia*, `https://en.wikipedia.org/wiki/Method_of_moments_(electromagnetics)` Accessed: Aug. 09, 2024.

[28] M. Bodehou, D. Gonzalez-Ovejero, C. Craeye, and I. Huynen, "Method of Moments simulation of modulated metasurface antennas with a set of orthogonal entire-domain basis functions," *IEEE Trans. Antennas Propag.*, vol. 67, no. 2, pp. 1119–1130, Feb. 2019.

[29] J. Cavillot, M. Bodehou, and C. Craeye, "Metasurface antennas design: Full-wave feeder modeling and far-field optimization," *IEEE Trans. Antennas Propag.*, vol. 71, no. 1, pp. 39–49, Jan. 2023.

[30] C. Simovski and S. Tretyakov, *An Introduction to Metamaterials and Nanophotonics.* Cambridge University Press, Nov. 2020, pp. 63–82.

[31] M. S. M. Mollaei and C. Simovski, "Dual-metasurface superlens: A comprehensive study," *Physical Review B*, vol. 100, no. 20, Nov. 2019.

[32] C. Wang *et al.*, "Multi-frequency metasurface carpet cloaks," *Optics Express*, vol. 26, no. 11, pp. 14 123–14 131, May 2018.

[33] A. Li, S. Singh, and D. Sievenpiper, "Metasurfaces and their applications," *Nanophotonics*, vol. 7, no. 6, pp. 989–1011, Jun. 2018.

[34] G. Minatti, M. Faenzi, M. Sabbadini, and S. Maci, "Bandwidth of gain in metasurface antennas," *IEEE Trans. Antennas Propag.*, vol. 65, no. 6, pp. 2836–2842, Jun. 2017.

[35] B. H. Fong, J. S. Colburn, J. J. Ottusch, J. L. Visher, and D. F. Sievenpiper, "Scalar and tensor holographic artificial impedance surfaces," *IEEE Trans. Antennas Propag.*, vol. 58, no. 10, pp. 3212–3221, 2010.

[36] Z. Zhang *et al.*, "Recent advances in reconfigurable metasurfaces: Principle and applications," *Nanomaterials*, vol. 13, no. 3, p. 534, Jan. 2023.

[37] H. Ojukwu, B.-C. Seet, and S. U. Rehman, "Metasurface-aided wireless power transfer and energy harvesting for future wireless networks," *IEEE Access*, vol. 10, pp. 52 431–52 450, 2022.

[38] C. H. Chu, S. Vyas, Y. Luo, P.-C. Yang, and D. P. Tsai, "Recent developments in biomedical applications of metasurface optics," *APL Photonics*, vol. 9, no. 3, Mar. 2024.

[39] W. Liu *et al.*, "Design strategies and applications of dimensional optical field manipulation based on metasurfaces," *Advanced Materials*, vol. 35, no. 30, Jun. 2023.

[40] J. Cavillot, "Fast electromagnetic analysis of large objects involving planar layered media: Application to antenna arrays and metasurfaces," Ph.D. dissertation, Univ. cath. Louvain., 2021.

[41] C. Craeye, *LELEC2350: Electromagnetic waves chapters 8 to 14*, Lecture notes, Univ. cath. Louvain., Aug. 2022.

[42] D. M. Pozar, *Microwave Engineering*, 4th ed. John Wiley & Sons, 2011.

[43] D. Flandre and C. Oestges, *LELEC1755 - physique des dispositifs électroniques et des lignes de transmission*, Lecture notes, weeks 1-4, 2023-2024.

[44] Y. Iulian Rosu, *Microstrip vs Stripline.* [Online]. Available: `https://www.qsl.net/va3iul/Microstrip_Stripline_CPW_Design/Microstrip_Stripline_and_CPW_Design.pdf`.

[45] I. Bahl and P. Bhartia, *Microstrip Lines and Slotlines.* Artech House, 2003.

[46] K. Gupta, R. Garg, I. Bahl, and P. Bhartia, *Microstrip Lines and Slotlines.* Artech House, 1996.

[47] H. A. Wheeler, "Transmission-line properties of a stripline between parallel planes," *IEEE Trans. Microw. Theory Techn.*, vol. 25, no. 8, pp. 631–647, 1977.

[48] M. Bodehou, A. Guth, K. A. Khalifeh, D. Heberling, and C. Craeye, "Multifeed metasurface antennas: Direct numerical design and experimental validations," *IEEE Access*, vol. 11, pp. 35 754–35 762, 2023.

[49] *RO4350B^{TM} Laminates*, 2024. [Online]. Available: `https://www.rogerscorp.com/advanced-electronics-solutions/ro4000-series-laminates/ro4350b-laminates`.

[50] H. Proto-Electronics, *Pcb - cuivre / épaisseur*, 2024. [Online]. Available: `https://www.proto-electronics.com/fr/pcb-cuivre-epaisseur`.

[51] *Stripline impedance calculator*, 2024. [Online]. Available: `https://www.pasternack.com/t-calculator-stripline.aspx`.

[52] B. Singh, N. Sarwade, and K. P. Ray, "A compact modified corporate feed network for antenna arrays with non-identical rectangular microstrip antenna elements," *Proc. IEEE Antennas Propag. Soc. Symp. (APSURSI)*, IEEE, Dec. 2016, pp. 1–2.

[53] W. Contributors, *Wilkinson power divider*, *Wikipedia*, `https://en.wikipedia.org/wiki/Wilkinson_power_divider`, Accessed: Jul. 23, 2024.

[54] *Wilkinson power splitters*, https://www.microwaves101.com/encyclopedias/wilkinson-power-splitters, Accessed: Jul. 23, 2024, Microwaves101.com, 2023.

[55] M. G.S, "Design and simulation of an eight-way binary wilkinson power divider," Apr. 2016.

[56] C. A. Balanis, *Antenna Theory: Analysis and Design*, 3rd ed. Hoboken, NJ: John Wiley & Sons, 2005, Chapter 14.

[57] M. Sánchez-Barbetty, "Design and implementation of a transceiver and a microstrip corporate feed for solid state x-band radar," Thesis, 2005. [Online]. Available: https://hdl.handle.net/20.500.11801/2413.

[58] J.-S. Hong and M. J. Lancaster, *Microstrip Filters for RF/Microwave Applications*, 2nd ed. John Wiley & Sons, 2011.

[59] Southwest Microwave, *0.9 mm supermini jack (female) 2 hole .438 long - southwest microwave*, Accessed: Jul. 29, 2024. [Online]. Available: https://mpd.southwestmicrowave.com/product/53029-005j-0-9mm-supermini-jack-female-2-hole-438-long/.

[60] D. Lederer, *LELEC2700 - microwaves*, Lecture notes, Chapitre 4 & Exercices 4-5, 2023-2024.

[61] C. Li, Y. Wang, and Z. Zhang, "A feed network of microstrip array antenna," *2017 IEEE 2nd Inf. Technol., Netw., Electron. Autom. Control Conf. (ITNEC)*, IEEE, Dec. 2017, pp. 610–613.

[62] A. F. Thomson and A. Gopinath, "Calculation of microstrip discontinuity inductances," *IEEE Trans. Microw. Theory Techn.*, vol. 23, no. 8, pp. 648–655, 1975.

[63] L. Liu, S. W. Cheung, and T. I. Yuk, "Compact mimo antenna for portable uwb applications with band-notched characteristic," *IEEE Trans. Antennas Propag.*, vol. 63, no. 5, pp. 1917–1924, May 2015.

[64] Wikipedia Contributors, *Standard deviation*, *Wikipedia*, https://en.wikipedia.org/wiki/Standard_deviation, Accessed: Aug. 13, 2024.

[65] N. Llombart, A. Neto, G. Gerini, and P. de Maagt, "Planar circularly symmetric ebg structures for reducing surface waves in printed antennas," *IEEE Trans. Antennas Propag.*, vol. 53, no. 10, pp. 3210–3218, 2005.

[66] M. Ettorre, S. Bruni, G. Gerini, A. Neto, N. Llombart, and S. Maci, "Sector pcs-ebg antenna for low-cost high-directivity applications," *IEEE Antennas Wireless Propag. Lett.*, vol. 6, pp. 537–539, 2007.

[67] B. S. Abirami and E. F. Sundarsingh, "Ebg-backed flexible printed yagi–uda antenna for on-body communication," *IEEE Trans. Antennas Propag.*, vol. 65, no. 7, pp. 3762–3765, 2017.

[68] Y. He, C. Oakley, P. Chahal, J. Albrecht, and J. Papapolymerou, "Aerosol jet printed 24 ghz end-fire quasi-yagi-uda antenna on a 3-d printed cavity substrate," *2017 Int. Workshop Antenna Technol. (iWAT)*, pp. 179–182.

[69] J. Hendrickx, P.-Y. Gousenbourger, and S. Guérit, *LEPL1106: Mathématiques appliquées : Signaux et systèmes*, Lecture notes, Mar. 2023.

Appendices

A Convolution of two functions

The convolution of two functions $f(t)$ and $g(t)$ in the time domain is defined as:

$$(f \circledast g)(t) = \int_{-\infty}^{\infty} f(\tau)g(t-\tau)\, d\tau \tag{1}$$

In this context, the convolution operation $\circledast$ represents the integral of the product of the two functions after one is reversed and shifted. This operation combines the two functions into a single function that describes how the shape of one is modified by the other [69].

B Current density repartition in the quarter-wavelength model

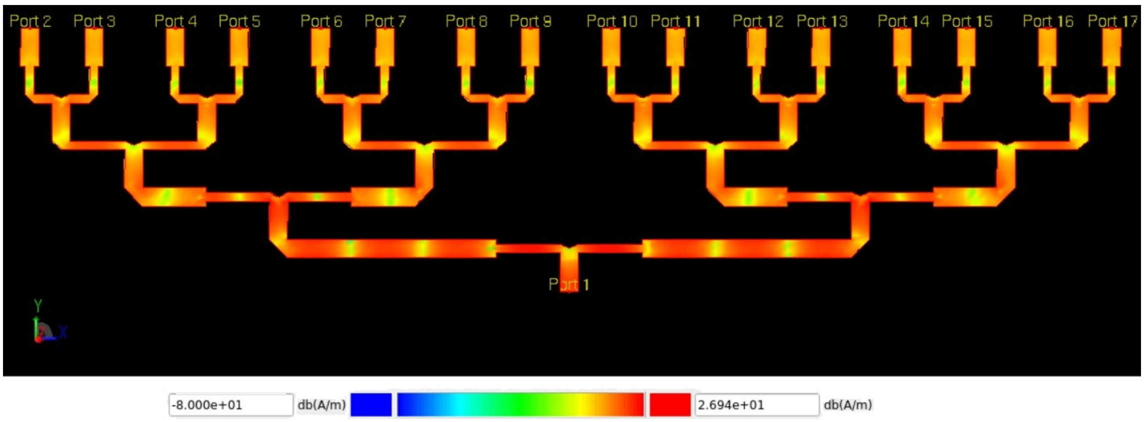

Figure 1: ADS momentum visualisation of current density in quarter-wavelength model

C Bandwidth observable thanks to the surface waves propagating at different frequencies

Figure 1 illustrates that a proper PW is generated for a frequency range of 23.3 to 23.7 GHz with a specific phase of 40°. This range corresponds to the interval during which the current's behaviour remains constant, as explained in Section 4.1.2.

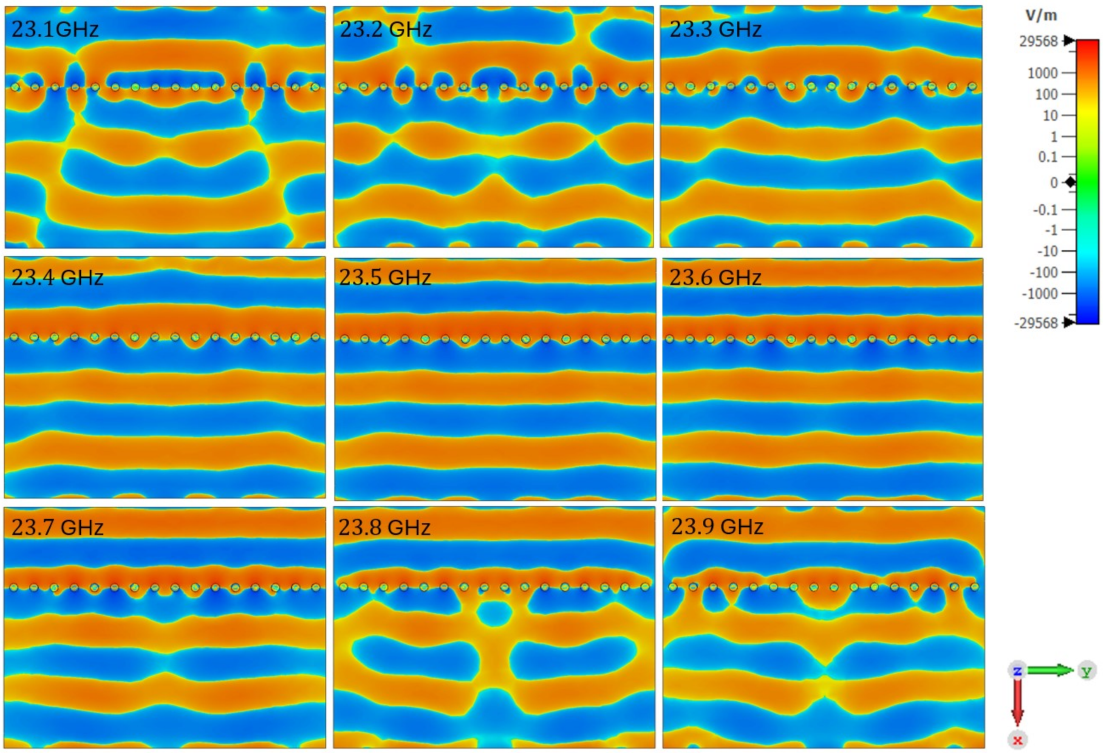

Figure 2: Surface waves propagating at different frequencies.

D Results obtained with the PEC cage

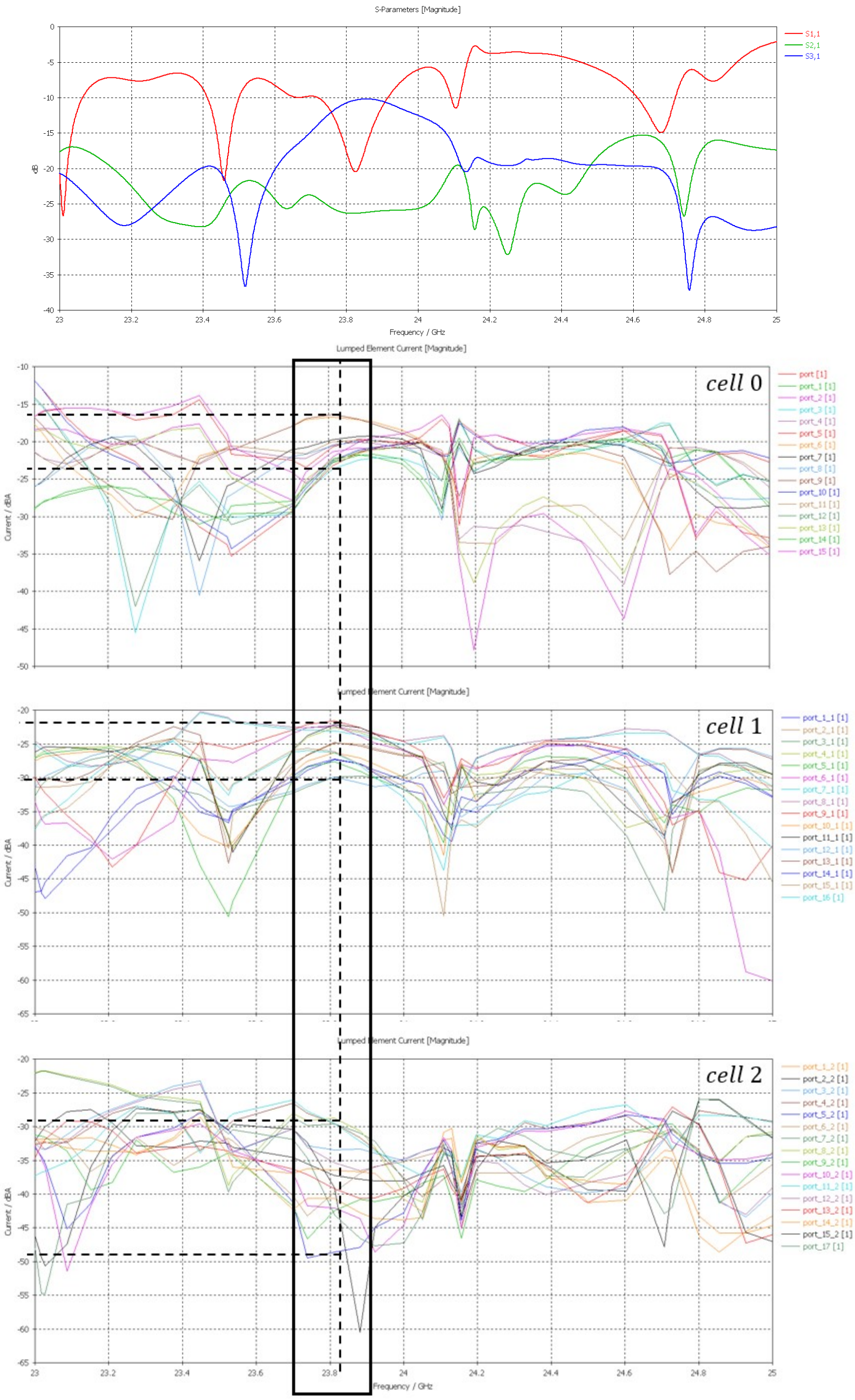

Figure 3: Results obtained with the PEC cage.

E Results obtained with the trenches in the top dielectric slab

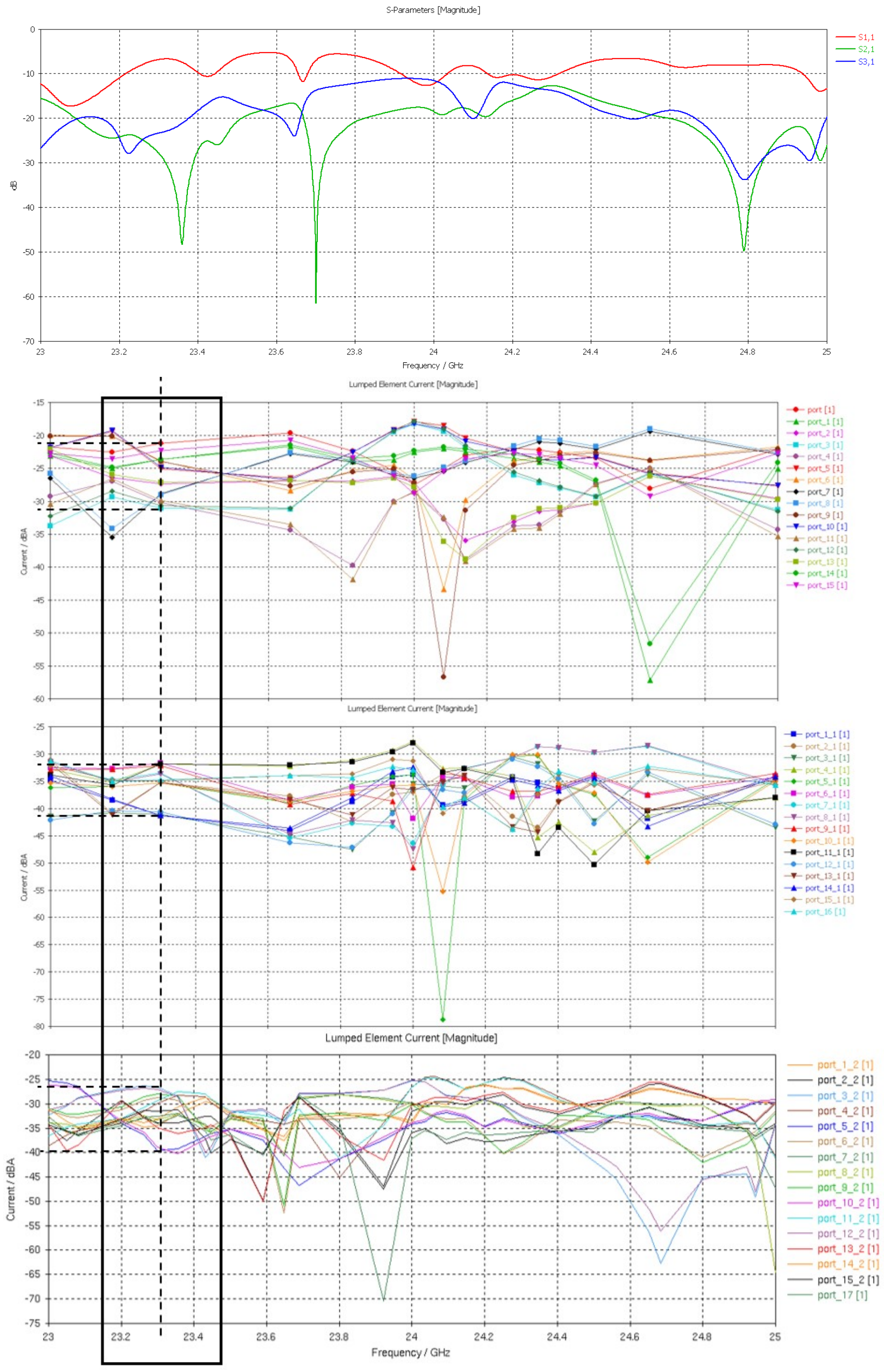

Figure 4: Results obtained with the trenches in the top dielectric slab.

F Results obtained with the blind vias added between the two ground planes

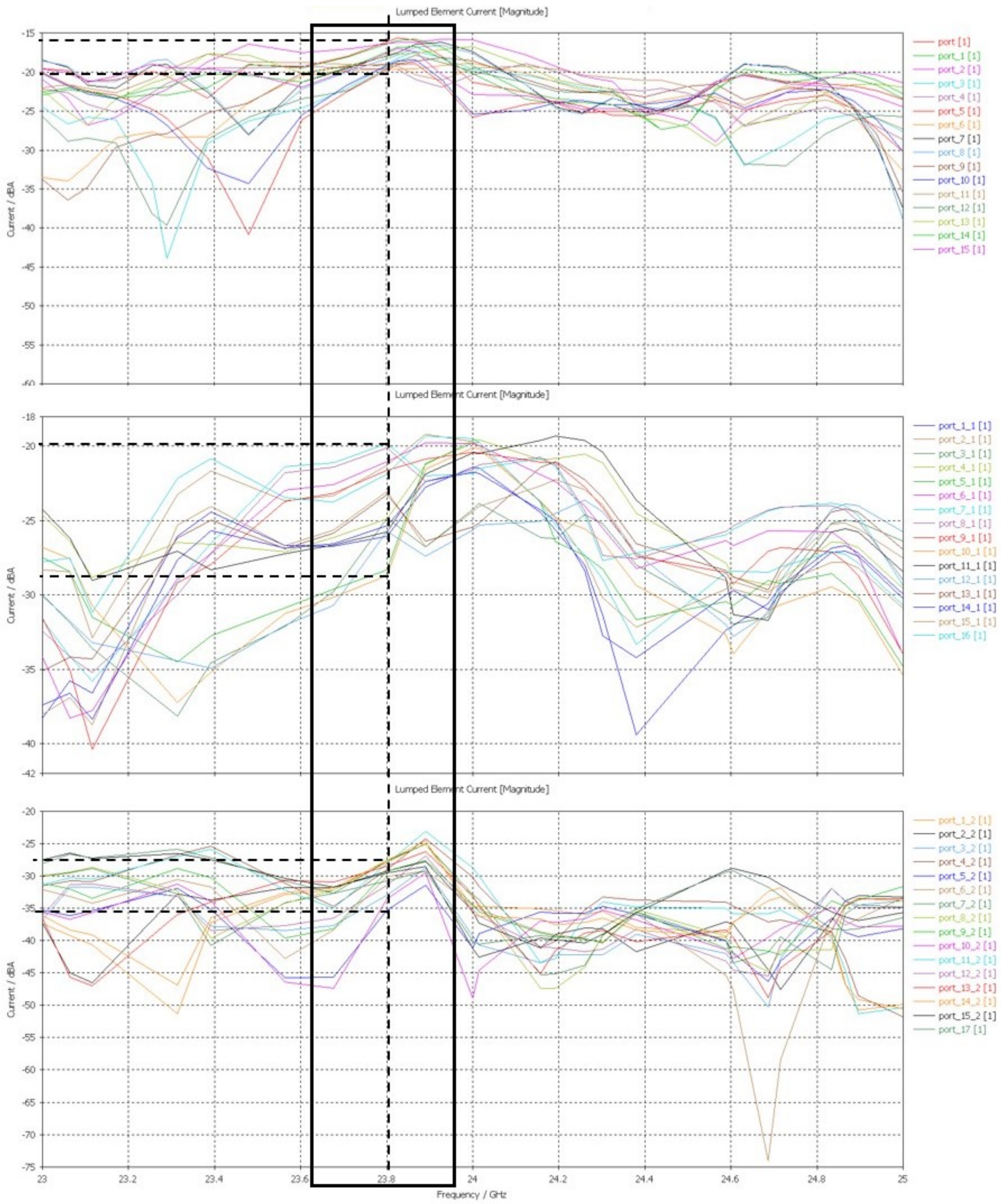

Figure 5: Results obtained with the vias walls added between the two ground planes.

G Results obtained with the final design

G.1 S-parameters, currents phases and magnitudes

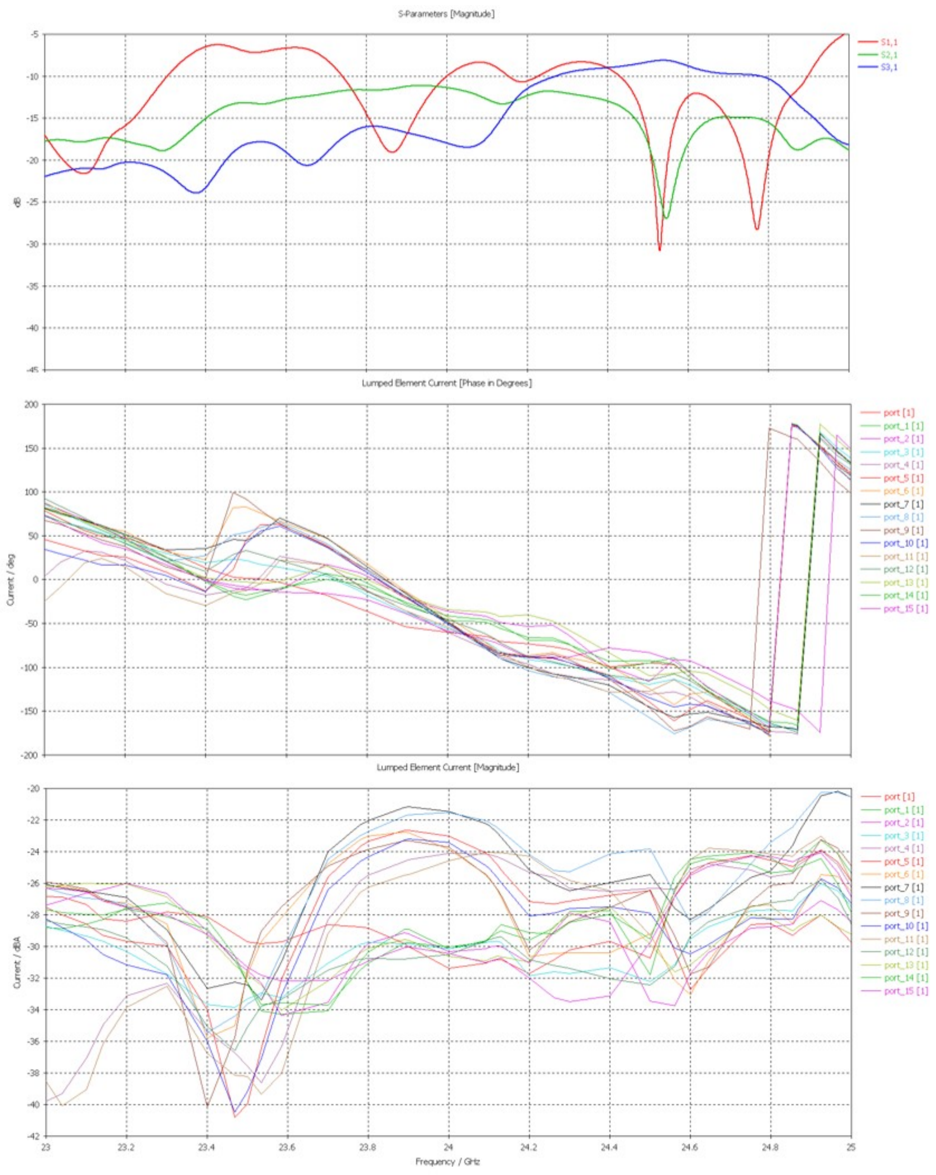

Figure 6: Results obtained with the final design after consulting with the manufacturer.

G.2 3D representation of the radiation pattern

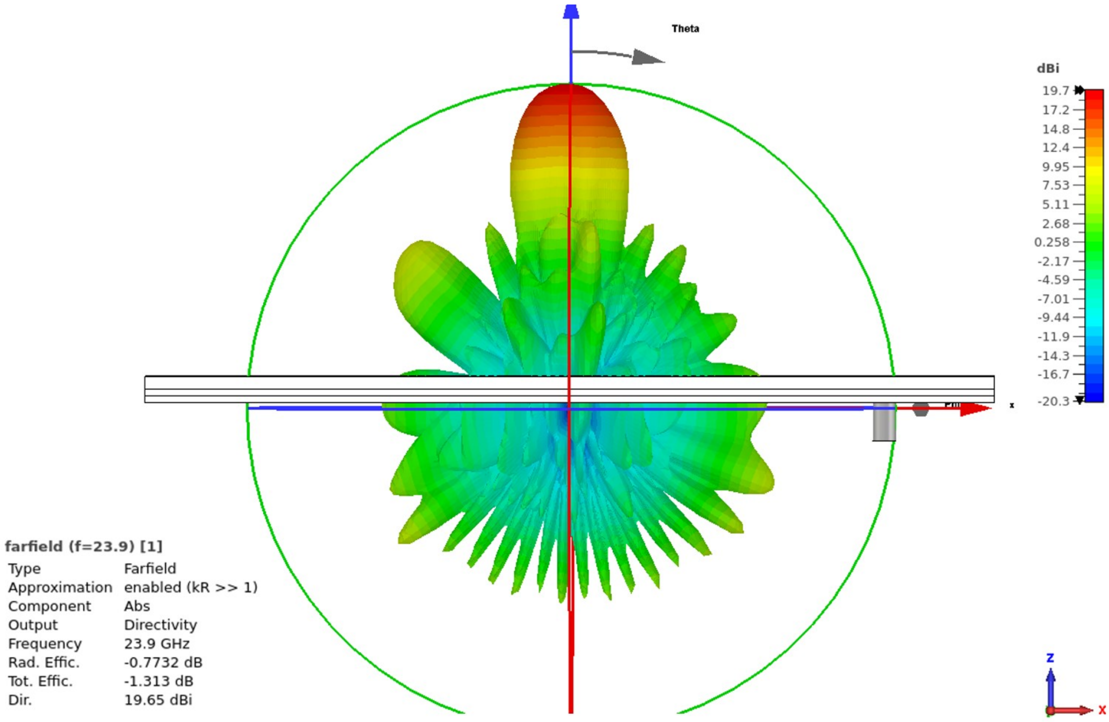

Figure 7: 3D representation of the radiation pattern obtained with the final model.

G.3 Propagating field at the frequency of $f = 23.9$ GHz

The spectral representation employed in Section 2.3 for the analysis of the propagating electric field can be utilised for a comparative evaluation of the results presented here. Furthermore, the x-component of the propagating field on the MTS substrate can be observed, which provides additional insight into the propagation of the planar surface wave (PW), as illustrated in Figure 8.

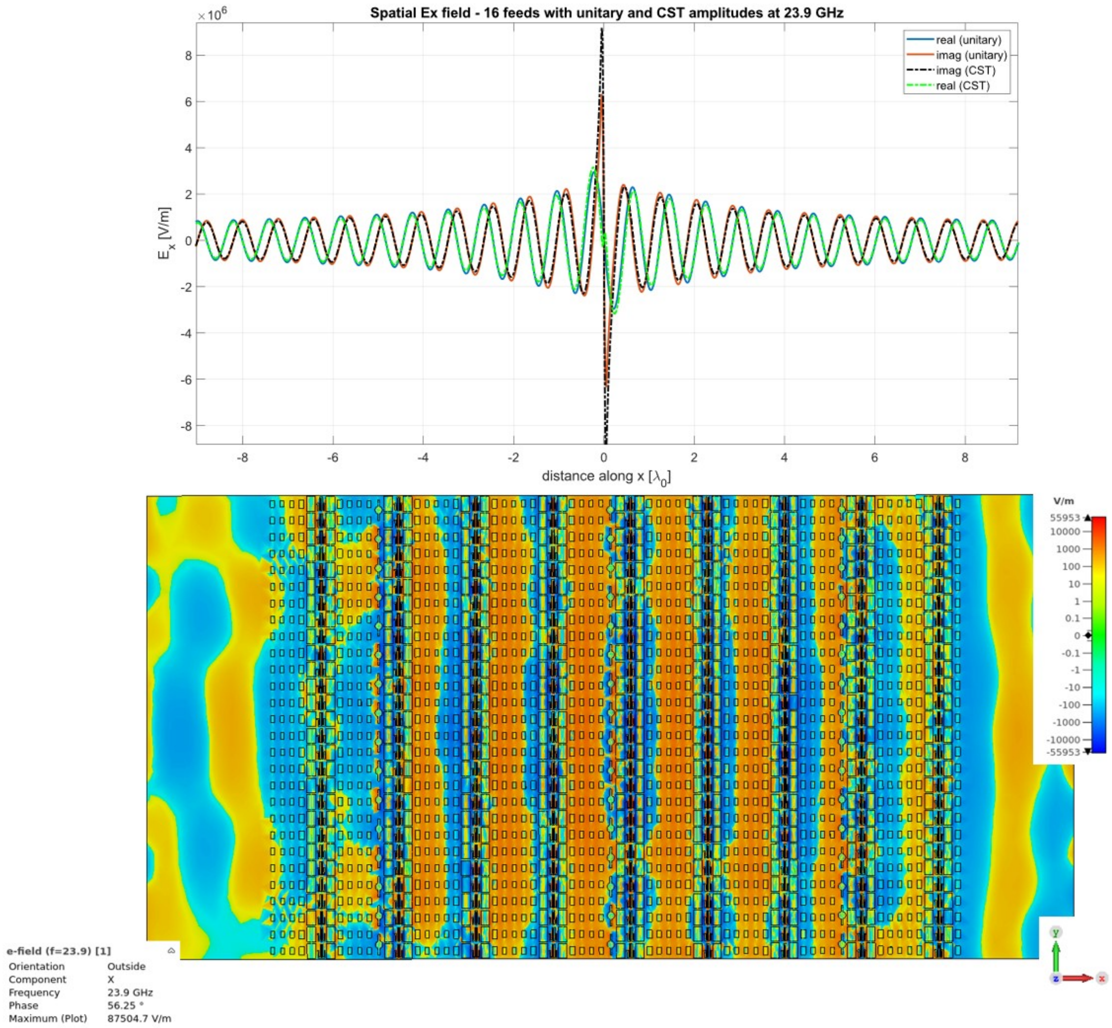

Figure 8: (a) Propagating x-component of the electric field compared with unitary weights, (b) graphical representation in CST showing the propagating field.

It can be observed that the x-component of the propagating field behaves in accordance with the expected behaviour, resulting in the generation of a planar surface wave.

UNIVERSITÉ CATHOLIQUE DE LOUVAIN
École polytechnique de Louvain
Rue Archimède, 1 bte L6.11.01, 1348 Louvain-la-Neuve, Belgique | **www.uclouvain.be/epl**